Université de Franche-Comté
École doctorale Carnot Pasteur

ELTE University of Budapest
Chemistry Doctoral School

Thèse de Doctorat

présentée par

Marias Darvas

pour obtenir le grade de
Docteur de l'Université de Franche-Comté en Physique
et celui de
Docteur de l'Université Eötvös Loránd de Budapest en Chimie

Modélisation d'interfaces par simulations numériques - des polymères en solutions à la troposphère -

Thèse en co-tutelle internationale dirigée par
Sylvain Picaud et Pál Jedlovszky

soutenue le 5 décembre 2012

Jury :

Président :	Ernő Keszei	Professeur - ELTE University of Budapest
Rapporteurs :	Marie-Pierre Gaigeot	Professeur - Université d'Evry
	László Turi	Professeur - ELTE University of Budapest
Examinateurs :	Pál Jedlovszky	Professeur - ELTE University of Budapest
	Claude Millot	Professeur, Université de Lorraine
	Sylvain Picaud	Directeur de Recherche CNRS, Besançon
	Imre Salma	Professeur - ELTE University of Budapest
	Céline Toubin	Maître de Conférences - Université de Lille 1

COMPUTER SIMULATIONS IN MODELING INTERFACIAL PHENOMENA
- FROM POLYMER SOLUTIONS TO THE TROPOSPHERE-

DOCTORAL (PhD) THESIS

DARVAS MÁRIA

Eötvös Loránd University of Science
Budapest

Chemistry Doctoral School
Head: Prof. György Inzelt

Theoretical , Physical and Structural Chemistry Program
Head: Prof. Péter Surján

Supervisor: Dr. Pál Jedlovszky, PhD, DSc

Université de Franche-Comté
Besançon

Carnot Pasteur Doctoral School
Head: Prof. H. Jauslin

Supervisor: Dr. Sylvain Picaud, PhD, HDR

Budapest, 2012

SZÁMÍTÓGÉPES SZIMULÁCIÓK A HATÁRFELÜLETEK MODELLEZÉSÉBEN
- POLIMER OLDATOKTÓL A TROPOSZFÉRÁIG-

DOKTORI (PhD) ÉRTEKEZÉS

DARVAS MÁRIA

Eötvös Loránd Tudomáynegyetem
Budapest

Kémia Doktori Iskola
Vezetője: Prof. Inzelt György

Elméleti és Fizikai Kémia, Anyagszerkezetkutatás Program
Vezetője: Prof. Surján Péter

Témavezető: Dr. Jedlovszky Pál, PhD, DSc

Université de Franche-Comté,
Besançon

Carnot Pasteur Doktori Iskola
Vezetője: Prof. H. Jauslin

Témavezető: Dr. Sylvain Picaud, PhD, HDR

Budapest, 2012

MODÉLISATION NUMERIQUE DES INTERFACES

- DES SOLUTIONS POLYMERIQUES Á LA TROPOSPHÉRE-

THÉSE DE DOCTORAT

DARVAS MÁRIA

Université Eötvös Loránd
Budapest

École Doctorale de Chimie
Directeur: Prof. György Inzelt

Programme Chimie Théorique, Chimie Physique et Chimie Structural
Directeur: Prof. Péter Surján

Directeur de thése: Dr. Pál Jedlovszky, PhD, DSc.

Université de Franche-Comté,
Besançon

École Doctorale Carnot Pasteur
Directeur: Prof H. Jauslin

Directeur de thése: Dr. Sylvain Picaud, PhD, HDR

Budapest, 2012

Acknowledgements

I am most grateful to my supervisors, Dr. Sylvain Picaud and Dr. Pál Jedlovszky for the productive moral and professional support and the lot of valuable advice with which they accompanied my PhD studies. I am especially thankful to them for giving me the possibility to create individual ideas, for trusting in them and for helping them develop into scientific work.

I would also like to express my gratefulness to Prof. Paul Hoang and Prof. Tibor Gilányi, whose ideas and support has always been a strong motivation during my work.

I am nonetheless grateful for the help and support of the other PhD students working formerly in our group, Hantal György, Lívia Bartók-Pártay and Katalin Pojják, whose technical support is deeply acknowledge.

At last but not at least I would like thank my parents for their never ceasing patience and for believing in my dreams.

CONTENTS

OUTLINE OF THE WORK

Interfacial science is a branch of physical chemistry which has attracted a never ceasing interest ever since its foundations have been established. In our days interfacial processes are intriguing for scientists working in a variety of fields of fundamental and applied physics and chemistry. The spectrum of these fields ranges from environmental research to nanoscience. One of the leading directions of interfacial science nowadays is the question of obtaining atomistic scale data directly about the interface. Computer simulations are known to be able to provide such data and thus they may complement highly developed surface sensitive experimental methods.

The present PhD thesis is aimed at demonstrating the ability of computer simulations, namely molecular dynamics and Monte Carlo techniques, to model interfacial phenomena. My work is comprised of two major subjects. One of them is the atomistic scale examination of solid interfaces relevant in atmospheric chemistry, whereas the other targets the investigation of liquid surfaces.

In my work concerning solid surfaces I have applied grand canonical Monte Carlo simulations to reconstruct the adsorption isotherm of acetaldehyde on ice at a temperature which is relevant for the upper troposphere. I have also investigated the adsorption of certain bifunctional volatile organic compounds, namely hydroxyacetone and oxalic acid on ice, by means of molecular dynamics simulation. Finally I have applied the MD method to study the phase behavior of aqueous organic aerosols in the tropospherically relevant (p,T) range. In all of these studies I have attempted to compare my results with relevant experimental data in order to justify the validity of the models and the applicability of the technique used.

My work concerning liquid interfaces includes first of all the examination of the competitive adsorption of polymers and surfactants on the free surface of water by means of molecular dynamics simulations. In this study, special attention has been paid to the correct intrinsic treatment of the interface in order to get an atomistic scale insight to the structure and dynamics of the mixed adsorption layer and subsequently to be able to describe the underlying thermodynamic features which invoke the observed competition. The other study concerning liquid interfaces targeted the characterization of the transfer of ions through liquid-liquid interfaces by using the potential of mean force method to calculate the free energy profile. The main direction of this work has been the development of a method to reconstruct the free energy profile of ions or small molecules with respect to the real dynamically changing intrinsic interface, in order to get a more detailed view on the process of ion transfer.

Chapter 1.

Introduction

In the everyday interpretation a macroscopic interface is a very simple two-dimensional object separating two immiscible or partially miscible phases, at least one of which is condensed. It is difficult to imagine that such a simple object as a two-dimensional plane may be intriguing enough to facilitate the birth and to support the flourishing of an entire discipline, interfacial science. The fact that the physical chemistry of colloids and interfaces has been, since the end of the 19th century subject to an ever increasing interest suggests that indeed its structure, and consequently the mechanism and thermodynamics of interfacial processes are more elaborate than what can be anticipated from the simplicity of the two-dimensional plane model, which to some might imply that the interface is merely a geometrical object.

The geometrical approach is invalid even from a macroscopic point of view, as evidently an interface of two phases of different chemical compositions can only be described in terms of the two phases it separates. The two-dimensional nature can be justified if we use a macroscopic approach, however if we increase the resolution through which the interface is examined to the atomistic scale, we will find that it is in fact a three-dimensional object. Namely, the interface can be defined as the three-dimensional region separating two phases, α and β, within which physico-chemical properties change from the bulk value characteristic of phase α to that of phase β. This definition implies that the interface is at least a monomolecular layer, but in certain systems it may spread from several molecular layers of phase α to several of phase β. The characteristics of this thin, most commonly monomolecular layer differ from those of the bulk phases. The reason for this difference can be explained if we examine the simplified model of the interface of a condensed phase is illustrated in Figure 1.1.

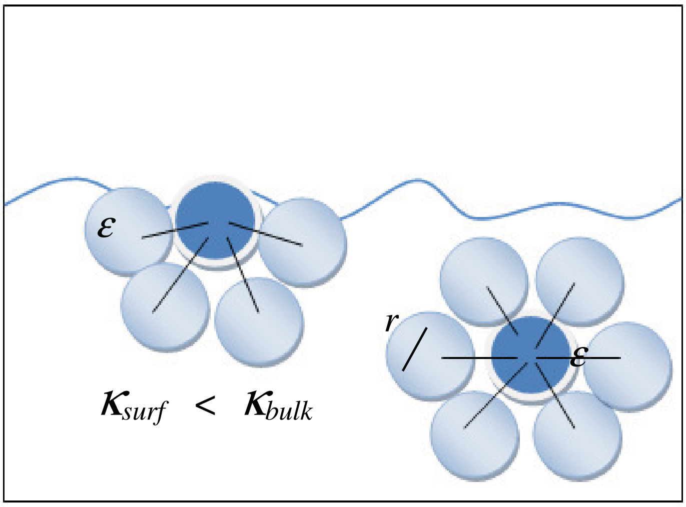

***Figure 1.1** Illustration of the origin of interfacial excess energy.*
Black lines connecting two molecules symbolize interaction between neighboring molecules

Looking at this figure, we may perform the following thought experiment. First of all, we pick a sphere randomly from the bulk phase and count its interacting neighbors. Supposing that the interaction energy between two neighboring spheres is ε, we can state that the average binding energy (E_{bind}^{bulk}) of molecule in the bulk phase is

$$E_{bind}^{bulk} = \kappa_{bulk}\,\varepsilon \quad , \tag{1.1}$$

where κ_{bulk} denotes the number of interacting neighbors in the bulk phase. Repeating our thought experiment with an interfacial molecule will result in obtaining a similar expression for the average binding energy of an interfacial molecule (E_{bind}^{surf}) with a number of interacting neighbors being $\kappa_{surf} < \kappa_{bulk}$. Consequently, the value of binding energy of an interfacial molecule will be:

$$E_{bind}^{surf} = \kappa_{surf}\,\varepsilon < E_{bind}^{bulk} \quad . \tag{1.2}$$

The difference between E_{bind}^{surf} and E_{bind}^{bulk} is usually defined as the interfacial excess energy. The existence of this excess energy which is responsible for several interface related phenomena, such as surface tension, the alteration of the pressure over curved surfaces, adsorption and surface activity, that is the enhancement of the concentration of a species in a mixture and the subsequent depletion of the others relative to their concentrations observed in the bulk phase.

Systematic investigation of interface-related problems dates back to as early as the 1870s. The birth of interfacial science can be attributed to the pioneering work of Gibbs[1] who, by developing a to our days valid thermodynamic background for several physico-chemical phenomena, including interfacial processes, put down the foundations of an entirely new discipline. During the last century, this new discipline, interfacial science, has grown out to be one of most important elements of understanding numerous different physico-chemical processes in the fields of atmospheric chemistry, colloid chemistry and nanoscience.

Experimental methods allowing the selective investigation of interfaces have gone through a rapid and dynamic development during the past decades. Nowadays several highly developed experimental techniques are at hand to examine the properties of surfaces. Images of the interface can be routinely taken by techniques such as transmission electron microscopy[2], scanning tunneling microscopy[3,4] or atomic force microscopy[5]. The chemical composition of interfacial layers may be measured by X-ray photoelectron spectroscopy (ESCA) [6], a multielement method which is able to provide lateral and depth concentration profiles of most of the common chemical elements composing our systems of interest. On the other hand, sum frequency generation (SFG) and second harmonic generation (SHG)[7] techniques are also useful tools to study solid or fluid interfaces. Besides instantaneous images and composition profiles, adsorption at interfaces is also of outstanding importance. Several experimental techniques, such as Fourier Transformation Infrared spectroscopy[8], allow us to reconstruct adsorption isotherms measured on solid surfaces. On the other hand, surface tension measurements performed for instance by methods like the Wilhelmy plate[9] or the hanging drop experiment[10], can be effectively applied to obtain surface excess concentrations of liquid mixtures. Measuring contact angles can also provide us with information about the geometrical and thermodynamic inhomogeneities of the surface in question [11].

With the development of the speed and efficacy of computers, simulations have emerged gradually to be one of the most important complementary techniques to experimental science as well as to purely theoretical methods. One of the biggest advantages of computer simulation techniques is that they enable us to see our systems of interest at an atomistic resolution. Besides this, they make it possible to model conditions that are experimentally difficult or even impossible to achieve. We may for example reach very low or very high temperature and pressure values without facing any difficulty creating and controlling the conditions, which can be useful when one wishes to model for instance physico-chemical processes of the upper layers of the atmosphere. On the other hand, information about extremely dilute solutions that are experimentally difficult to study are also readily available from simulations.

The above mentioned advantages enabled me to apply Monte Carlo and molecular dynamics simulations to model physico-chemical processes related to interfacial phenomena. My work is comprised of two main topics, namely the study of solid and liquid interfaces. The first one is the adsorption of small molecules on atmospherically relevant solid surfaces, such as the free surface of ice or of organic and binary water/organic aerosols. The second is the examination of fluid interfaces from various aspects. The latter includes the investigation of adsorption and competitive adsorption of polymers and surfactants on the free surface of water. Besides this, I have also applied molecular dynamics simulations to develop a new intrinsic approach to calculate the free energy profiles describing the thermodynamic background of transfer small molecules through fluid interfaces.

My thesis is organized as follows. In the next chapter, I collect and describe all the computational methods applied during my work, including the description of the newly developed protocol to calculate the intrinsic free energy profile of transfer of small molecules through various interfaces. In Chapter 3. I give an overview on solid interfaces, I introduce atmospherically relevant problems related to adsorption at solid surfaces. Then I summarize the major steps of the development in the field of computer simulations that allowed us to use them as tools to model solid surfaces of the atmosphere and finally I present the results of my studies concerning this subject. In Chapter 4, I address the question of fluid interfaces. First of all, I summarize the basic characteristics of fluid interfaces, and give examples of some intriguing interfacial phenomena, then I describe the advances of computational methods in the treatment of fluid interfaces and finally I introduce the results obtained during my work related to this subject. Finally, in Chapter 5, all my results are summarized and some perspectives are listed.

Chapter 2.

Computational methods

2.1. The place of computer simulations in scientific research

Scientific research historically relies mainly on experimental techniques. However, investigating physico-chemical processes in details may require the application of a theoretical approach as well. If we wish to use a purely theoretical method, we are obliged to apply simplifying conditions for the mathematical apparatus as well as for the model system. Simulations on the other hand may be performed on an appropriately chosen model system without any simplifying conditions which implies that they provide exact results valid for the model system. Thus simulation techniques can be considered as computer assisted experiments performed on the model system. The above three ways of approach in scientific research are, nevertheless, inseparable and incomplete without each other. Model systems are needed for both theoretical methods and simulations. The applicability and the validity of a model system may only be assessed by comparing theoretical and simulation results with the corresponding experimental values. Thus if we compare our simulation results with the relevant experimental data, we may check the validity of the model, whereas comparing the simulation and theoretical data obtained for the same model system can be regarded as the test of the theoretical approximation.

2.2 Comparison of the Monte Carlo and molecular dynamics methods

Any computer simulation technique relies on the basic idea of statistical physics that it is possible to calculate macroscopic properties of a system as an average over all the microstates belonging to the macroscopic state in question. It is obviously impossible to sample the entire phase space, that is to have a sample configuration of each of the microstates belonging to a macroscopic state, as it would require calculating and storing an enormous amount of data. However, computer simulations are handy tools to produce a statistically relevant sample ensemble, on which time or ensemble averaging can be performed, depending on the simulation method, to obtain macroscopic properties.

The ergodic hypothesis guarantees that, for a system in equilibrium, the above mentioned time and ensemble averages over a set of microstates are equivalent.

$$\langle M \rangle_t = \lim_{\tau \to \infty} \frac{1}{\tau} \int_0^\tau M(\bar{q}(t), \bar{p}(t)) dt = \int M(\bar{q}, \bar{p}) f(\bar{q}, \bar{p}) d\bar{q} d\bar{p} = \langle M \rangle_\Gamma \quad , \tag{2.1}$$

where $\bar{p}(t)$ and $\bar{q}(t)$ denote the momenta and the spatial coordinates of the particles constituting the system, $M(\bar{p}, \bar{q})$ is the value of the quantity in a given $\Gamma = \{\bar{p}(t), \bar{q}(t)\}$ microstate of the phase space, whereas $<M>_t$ and $<M>_\Gamma$ denotes the time and the ensemble average of quantity M over the set of microstates, respectively, finally, $f(\bar{p}, \bar{q})$ is the probability density function of the microstates, while t stands for the time and τ denotes the duration of observation. The equality of time and ensemble averages ensured by the validity of this hypothesis for systems in equilibrium guarantees the equivalence of Monte Carlo (MC) and molecular dynamics (MD) simulation for calculating equilibrium properties of our systems.[12]

These two methods differ in their way of generating a statistically relevant set of microstates. In molecular dynamics the microstates are created by solving the Newtonian equations of motion in each step of the simulation for each particle of the system. The new configurations are then obtained simply by moving the atoms according to the forces acting on them. MD is thus a deterministic method, which means that the initial state unambiguously determines the entire set of microstates which the system goes through. This in turn means that MD simulations may be used for calculating time dependent, dynamic properties as well as equilibrium thermodynamic quantities. In Monte Carlo simulations sample configurations are generated stochastically, and are accepted or rejected according to a conveniently chosen acceptance criterion. Thus in an MC simulation the initial configuration cannot determine *a priori* the entire set of microstates that will compose the sample. Consequently, it is impossible to calculate time dependent properties by MC simulations, however for quantities that depend only on the spatial coordinates the average value obtained from MC and MD simulations should be similar within statistical error. Both MD and MC methods have been used during my PhD studies, thus they are described in detail in section 2.5. and 2.6, after introducing the most important technical issues related to both of them.

2.3 The calculation of the energy in simulations

One of the most important question in performing simulations is how to obtain the energy of the microstates constituting our sample. As it has been seen in the previous section, in classical simulations a microscopic state is specified as the function of atomistic and molecular spatial coordinates and momenta of the particles building it up. The kinetic energy term of system consisting of *N* particles can be expressed simply in the following way, in cases where it is relevant:

$$K=\sum_{i=1}^{N}\sum_{\alpha}\frac{p_{i\alpha}^{2}}{2\mathrm{m}_i}\quad, \tag{2.2}$$

where m_i is the molecular mass of the i^{eth} molecule and α is the index which denotes the three Descartes coordinates of the molecular momentum *p* of molecule *i*. As is seen, the kinetic energy of the entire system can be given in an exact form as the sum of the molecular kinetic energy terms. However, the expression of the potential energy (*V*) is far from being as simple since the value of potential energy is determined mostly by the nature of intermolecular interactions. It follows from the previous statement, that in a system containing *N* particles the potential energy term of the Hamiltonian can be written as the sum of the single molecule terms, pair interaction energies, triplets, quadruplets, etc.[12]:

$$V=\sum_{i}v_1(q_i)+\sum_{i}\sum_{j>i}v_2(q_i,q_j)+\sum_{i}\sum_{j>i}\sum_{k>j>i}v_3(q_i,q_j,q_k)+\ldots\quad, \tag{2.3}$$

where q_i are the spatial coordinates of the atoms, and the *i*, *j* and *k* indexes run over the atoms of the system. The first term expresses the effect of an external field on the individual atoms, the second denotes pair interactions, whereas the following terms of the summation describe higher order intermolecular interactions. It has been proven that higher than third order terms give a very small, but not negligible part of the total potential energy, whereas third order terms are already significant in condensed phases. For instance it has been shown by Doran and Zucker that three-body interactions constitute as large as 10% of lattice energy in solid argon[13]. Despite the size of triplet interactions, potential energy terms are usually taken into account up to second order terms, whereas three-body (and higher order) interactions are partially accounted for by an effective pair potential. Within the framework of the above described approach we may express the potential energy as follows:

$$V \approx \sum_i v_1(r_i) + \sum_i \sum_{j>i} v_2^{eff}(r_{ij}) \quad , \tag{2.4}$$

where r_i are the spatial coodirnates and $r_{ij} = |r_i - r_j|$. Thus the potential is formally divided into two main contributions, the effect of an external field (v_1) and an effective pair potential ($v_2^{eff}(r_{ij})$).

Various different effective pair potential types have been developed in the literature.[12] The simplest one among them is the so called hard sphere potential, which creates no interaction beyond a certain cutoff distance and a constant infinite repulsion for atom-atom distances smaller than the above mentioned cutoff. Square-well or triangle well potentials are also used for describing pair interactions in a simple way. For distances larger than a cutoff distance they behave similarly to the hard sphere potential, however within the cutoff distance they describe the interaction as a simple mathematical function of the separation between the interacting atoms. The most widely used potential type in classical numerical simulations is the so called Lennard-Jones potential. The Lennard-Jones potential consists of a repulsive term decreasing as a function of the site-site distance r by $1/r^{12}$, and an attractive term decreasing as a function of $1/r^{6}$.:

$$V^{LJ}(r) = 4\epsilon\left[\left(\frac{\sigma}{r}\right)^{12} - \left(\frac{\sigma}{r}\right)^{6}\right] \quad . \tag{2.5}$$

As is seen from Equation 2.5, there are two adjustable parameters in a Lennard-Jones type potential. σ represents the „radius” of the particle, while ϵ describes the energy or strength of its interactions. Another widely used potential type is the so called Buckingham potential, in which the attractive term is described by an exponentially decaying function, while the repulsion is similar to what has been seen for the Lennard-Jones type of effective pair potential.

In simple systems the dispersion contribution to the interaction between two interacting particles A and B, can be described as the combination of the Lennard-Jones parameters of the particles in question either by the Lorentz-Berthelot rule[14] or by the rule of geometric means.[12] The above mentioned two combination rules are shown in Equation 2.6 a and b, respectively:

$$\epsilon_{AB} = \sqrt{\epsilon_A \epsilon_B} \qquad \sigma_{AB} = \frac{\sigma_A + \sigma_B}{2} \tag{2.6 a}$$

$$\epsilon_{AB} = \sqrt{\epsilon_A \epsilon_B} \qquad \sigma_{AB} = \sqrt{\sigma_A \sigma_B} \,. \tag{2.6 b}$$

Additionally, if the system consists of charged particles, electrostatic interactions have to be taken into account as well. These interactions most often are expressed by the Coulomb potentials, which can be written as follows:

$$V_C = \frac{1}{4\pi\varepsilon_0} \frac{q_A q_B}{r} \,, \tag{2.7}$$

where ε_0 is the permittivity of vacuum whereas q_A and q_B are the partial charges of atoms A and B.

2.4 Technical issues of performing simulations

Any computer simulation begins with preparing an initial configuration of the system of interest. An initial configuration can be obtained by placing the desired number of molecules somehow (for instance, randomly or in a crystal-like structure) into the simulation box. However, initial configurations obtained in one of the above-mentioned ways may correspond to energies too high for the simulation program to deal with or may slow down the equilibration process considerably and the probability of encountering such a problem is significantly higher for systems of higher complexity. This error may be avoided by starting from a pre-equilibrated configuration or by preparing the initial configuration in a way that it already resembles its anticipated equilibrium structure.

In the first phase of the simulation the energy of the system decreases monotonically and all other parameters describing the given statistical mechanical ensemble show a tendentious change. This phase of the simulation is called equilibration. After a certain number of steps the tendency disappears for even the slowest changing one among the monitored variables, and the values start to fluctuate around their average value. In this latter production stage configurations are saved for creating a statistically relevant model of the equilibrium statistical mechanical ensemble.

The capacity of today's computers allows us to simulate systems consisting of 10^4-10^5 molecules at a relatively low computational cost. However such a system is still many orders of magnitude smaller than what can be examined by regular experimental setups. Thus, as opposed to real systems, in a simulated model up to 15% of the molecules are found at the interface which may cause systematic errors due to the occurrence of the extraordinarily strong unphysical interfacial phenomena. The simplest way to overcome this problem is to surround the system with an infinite number of its own images translated along the box edges in all directions, that is to apply periodic boundary conditions.[12] It allows us to increase the system size practically to infinity without raising the computational cost noticeably. Such periodic boundary conditions can only be applied if the shape of the simulation box allows us to fill the space with its translated images without any gaps or overlaps, and their use results in the fact that if a particle leaves the basic simulation box in one direction in one step, its periodic image enters on the opposite side. Periodic boundary conditions are illustrated in Figure 2.1.

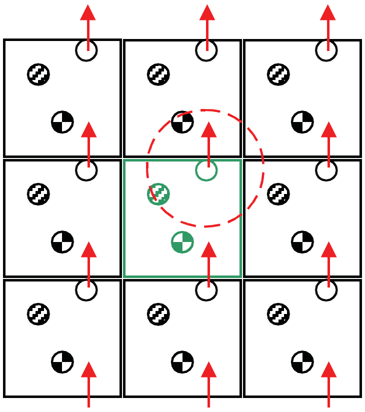

Figure 2.1 *Illustration of the periodic boundary conditions. The green square in the middle of the figure represents the basic box, the black copies are the periodic boundary images, whereas arrows show the movement of the periodic images of molecules traversing the box edge and the dashed circle symbolizes the maximum cutoff length (L/2) within which explicit treatment of intermolecular interactions is physically meaningful.*

It follows from the periodic boundary conditions that, in case of a cubic simulation box of length L it is only reasonable to calculate distance dependent properties of a given molecule within sphere of radius $L/2$, since at larger distances the molecules may be present together with one or more of its periodic images. (Figure 2.1.) This would give rise to artificial interactions and translational symmetry and, subsequently, to unphysical results. However, simply cutting the distance dependent properties is problematic when calculating pair interaction energies. Dispersion terms tend quickly to zero with the increasing distance, however, electrostatic interactions give a considerable contribution to the potential even at higher distances, thus it needs to be accounted for by long-range corrections, such as the Ewald summation [15], the Particle Mesh Ewald method (PME) [16] or the reaction field correction (RFC).[17]

2.5 Monte Carlo simulations

Any computational technique which applies stochastic sampling to obtain an approximate solution to mathematical problems belongs to the family of Monte Carlo methods. Its basic idea makes Monte Carlo methods highly suitable for solving multidimensional integrals, thus it is a technique widely used in physics for modeling statistical mechanical ensembles. In statistical mechanical simulations the phase space has to be sampled according to the probability density function $f(\bar{p},\bar{q})$ over the ν microstates, which can be written in the following form:

$$f(\bar{q},\bar{p})=\frac{\exp(-\beta F_{\nu}(\bar{q},\bar{p}))}{\sum_{\nu}\exp(-\beta F_{\nu}(\bar{q},\bar{p}))}, \tag{2.8}$$

where $F(\bar{p},\bar{q})$ is an energy-like potential function of the spatial coordinates and the generalized momenta whose actual form depends on the thermodynamic boundary conditions, or in other words the gender of the modeled ensemble, and $\beta=1/k_BT$, where T is the thermodynamic temperature and k_B is the Boltzmann constant). The denominator of the right side of the expression is the so called canonical partition function Q of the system:

$$Q=\sum_{\nu}\exp(-\beta F_{\nu}(\bar{q},\bar{p})). \tag{2.9}$$

According to equation 2.9 the partition function Q is given in an exact form as a sum over all the microstates. In the semiclassical approximation, which is usually used in classical simulations, Q is expressed in an integral form which has to be corrected for two basic defects of the approach. First of all, as the permutation of the particles does not increase the number of microstates we have to divide the partition function by $1/N!$ to account for the indistinguishable nature of particles. On the other hand quantum states are also indistinguishable in such a small unit volume of the phase space, thus one has to account for them too, which can be done by reducing the number of microstates by a factor of h^{3N}, where h is Planck's constant. After adjusting these corrections, Q will be approximated by the following expression:

$$Q=\frac{1}{N!h^{3N}}\int d\bar{q}\,d\bar{p}\exp(-\beta F_{\nu}(\bar{p},\bar{q})) \tag{2.10}$$

Thus performing the necessary algebraic operations the following expression will be yielded for the probability density function:

$$f(\bar{q},\bar{p})=\frac{1}{N!h_{3N}}\frac{\exp(-\beta F_{\nu}(\bar{q},\bar{p}))}{Q}. \tag{2.11}$$

2.5.1 Calculating macroscopic mean quantities from Monte Carlo simulations

The mean value of a general macroscopic quantity M can be calculated as the ensemble average of the values of M over the microstates:

$$\langle M\rangle=\frac{1}{N!}\int dq\,dp\,M(\bar{q},\bar{p})\,f(\bar{q},\bar{p}) \quad , \tag{2.12}$$

where $M(\bar{q},\bar{p})$ is the value of the M quantity in the microstate characterized by a given value of $\bar{p}$ and $\bar{q}$, and angle brackets denote ensemble averaging. Since solely the position-dependent part of the phase space can be sampled by regular Monte Carlo techniques, it is only possible to calculate macroscopic values of quantities which depend only on the spatial coordinates. The momentum dependent parts can, on the other hand be separated and integrated out from equation 2.12. Thus after substituting Eq. 2.11 into the expression and performing the possible simplifications, eventually we obtain the following formula for the mean value of M:

$$\langle M\rangle=\frac{\int dq\,M(\bar{q})\exp(-\beta F_{\nu}^{q}(\bar{q}))}{\int dq\exp(-\beta F_{\nu}^{q}(\bar{q}))} \quad , \tag{2.13}$$

where the q in superscript denotes the part of the energy like functional that depends solely on spatial coordinates. This equation is what makes it possible thus to approximate macroscopic values of position-dependent quantities based on a set of configurations collected during the course of Monte Carlo simulations of statistical mechanical ensembles.

2.5.2 The question of sampling

According to equation 2.13, the expectation value of M can be approximated if we know its microscopic value in a statistically relevant number of discrete points of the configuration space, supposing that the value of the potential-like quantity $F_{\nu}^{q}(\bar{q})$ is also known for these points. In this case the integral of equation 2.13 is transformed into a finite sum to yield the following expression for the mean value of M:

$$\langle M\rangle=\frac{\sum_{i\in S}M(q_i)\exp(-\beta F_{\nu}^{q}(q_i))}{\sum_{i\in S}\exp(-\beta F_{\nu}^{q}(q_i))} \quad , \tag{2.14}$$

where index i runs over the discrete set of points (atomic configurations or microstates) of the configuration space S constituting our sample. Even though calculating the value of M according to this approximation does not require the knowledge of the entire configuration space, the number of microstates in which $M(q_i)$ and $F_v^q(q_i)$ are needed to be known in order to give a good approximate to the real macroscopic value of M is still far too high to be obtained during a simulation of reasonable length. This problem can be simplified by considering the fact that probability of the realization of a microstate decreases exponentially with the value of $F_v^q(q_i)$, thus microstates corresponding to very high $F_v^q(q_i)$ values give a small contribution to the ensemble average whereas „low energy" configurations contribute to it significantly.[18] Thus if we introduce a weight factor w_i to achieve that microstates characterized by a relatively low value of $F_v^q(q_i)$ are chosen with a relatively larger frequency in our sample, we can decrease the time demand and the computational cost of our calculations significantly. On the other hand such a weighted method distorts the randomness of the sampling, which can be recovered by correcting the mean value of M in the following way:

$$\langle M\rangle=\frac{\sum_{i\in S} M(q_i)\frac{\exp(-\beta F_v^q(q_i))}{w_i}}{\sum_{i\in S}\frac{\exp(-\beta F_v^q(q_i))}{w_i}} . \tag{2.15}$$

If the simulation is performed on the canonical (N,V,T) ensemble, in which case the position-dependent part of the potential-like function is the potential energy $U(q_i)$ of the system, the weight factor is usually chosen to be the Boltzmann factor:

$$w_i(q_i)=\exp(-\beta U(q_i)) . \tag{2.16}$$

Substituting the Boltzmann factor to Equation 2.15. yields a simplified expression for the expectation value of M:

$$\langle M\rangle=\frac{\sum_{i=1}^{n} M_i(q_i)}{n} , \tag{2.17}$$

where n is the number of configurations (microstates) in the sample.

The above described Metropolis-sampling is carried out in the following way. Initially a random change is made in the starting configuration. Then the potential energy of the new configuration obtained as the result of the change is calculated. Steps leading to the decrease of the potential energy are always accepted. On the other hand, steps which increase the potential energy of the system are accepted with a probability of $\exp(-\beta\Delta U)$ and are rejected with a probability of $\exp(1-\beta\Delta U)$, where ΔU is the difference between the potential energy of the current and the previous configuration. In practice, the acceptance of a step is decided by comparing $\exp(-\beta\Delta U)$ to random number ξ whose value varies between 0 and 1. If the value of ξ is smaller than or equal to $\exp(-\beta\Delta U)$ then the step is accepted, otherwise the attempted step is rejected. Thus probability of acceptance (P_{acc}) can be given as :

$$P_{acc}=min(1,\exp(-\beta\Delta U)) \quad . \tag{2.18}$$

It has been demonstrated by Metropolis and coworkers that a simulation performed this way models the real probability density function properly. In the following sub section the application of the Metropolis sampling for performing Grand Canonical Monte Carlo simulations is described.

2.5.3 Grand canonical Monte Carlo simulations

In the grand canonical Monte Carlo method, which has been developed independently by Norman and Filinov[19] and Adams[20,21], the μ chemical potential, the volume and the temperature of the system are kept fixed, while the number of molecules may vary. On the grand canonical ensemble the condition of equilibrium is the minimum of the grand potential Ω

$$\Omega=A-N\mu=-pV \quad , \tag{2.19}$$

where A is the Helmholtz free energy of the system, N stands for the number of particles, μ is the chemical potential while p and V are the pressure and volume of the system respectively. The expectation value of an arbitrary macroscopic quantity can be written in the following form:

$$\langle M\rangle=\frac{\sum_{N=1}^{\infty}\frac{1}{N!h^{3N}}\int d\bar{q}\,d\bar{p}\,M(\bar{q},\bar{p})\exp(\beta(N\mu-E(\bar{q},\bar{p})))}{\Xi}\quad, \qquad (2.20)$$

where $E(\bar{q},\bar{p})$ is the energy of the system and the notation Ξ stands for the grand canonical partition function:

$$\Xi=\sum_{N=1}^{\infty}\frac{1}{N!h^{3N}}\int d\bar{q}\,d\bar{p}\exp(\beta(N\mu-E(\bar{q},\bar{p})))\quad. \qquad (2.21)$$

Differently from the regular canonical simulations, in the grand canonical Monte Carlo method configurations have to be saved from many phase spaces characterized by different number of particles. This means that coefficients depending on the number of particles do not cancel out after separating and integrating the momenta dependent part of the potential. Thus after introducing the concept of the thermal de Broglie wavelength:

$$\Lambda=\sqrt{\frac{h^2\beta}{2\pi m}} \qquad (2.22)$$

and changing to the conventionally used scaled coordinates *s*:

$$s=\bar{q}V^{1/3}\quad, \qquad (2.23)$$

the following expression for the expectation value of *M* will be obtained:

$$\langle M\rangle=\frac{\sum_{N=1}^{\infty}\int ds\,M(s)\frac{V^N}{N!\Lambda^{3N}}\exp(\beta(N\mu-U(s)))}{\sum_{N=1}^{\infty}\int ds\frac{V^N}{N!\Lambda^{3N}}\exp(\beta(N\mu-U(s)))}\quad. \qquad (2.24)$$

The weight factor used for Metropolis sampling on the grand canonical ensemble takes to following form:

$$w_i(s,N)=\exp[N\ln(\frac{V}{\Lambda^3})-\ln(N!)-\beta(U(s)-N\mu)]\quad. \qquad (2.25)$$

In GCMC simulations the acceptance ratio can thus be expressed as:

$$P_{acc}=min\{1,\exp[\Delta(N\ln(\frac{V}{\Lambda^3})-\ln(N!)-\beta(U(s)-N\mu))]\} \quad . \tag{2.26}$$

This expression is reduced to the canonical acceptance ratio for particle displacement steps. On the other hand, for insertion and deletion steps it takes the form of

$$P_{acc}=min\{1,\exp[\ln(\frac{V}{\Lambda^3})-\ln(N+1)-\beta(\Delta U(s)-\mu)]\} \tag{2.27 a}$$

and

$$P_{acc}=min\{1,\exp[-\ln(\frac{V}{\Lambda^3})-\ln(N)-\beta(\Delta U(s)+\mu)]\} \tag{2.27 b}$$

respectively, provided that deletion or insertion of only one molecule is attempted in every step. The basic algorithm may be accelerated by searching for cavities of a radius larger than a conveniently chosen cutoff value and attempting insertion first in that cavity[22,23].

For our adsorption studies we have used the reformulation of the basic GCMC method suggested by Adams.[12] According to this approach the chemical potential is given as the sum of an ideal gas and an excess contribution.

$$\mu=\mu^{id}+\mu^{ex}=\mu^{ex}+kT[\ln\langle N\rangle_{\mu,V,T}+\ln(\frac{\Lambda^3}{V})]=kTB+kTln(\frac{\Lambda^3}{V}) \quad , \tag{2.28}$$

where B is a simplified notation for the sum of the excess chemical potential and the average number of molecules, and it can be conveniently expressed from equation 2.28 as :

$$B=\frac{\mu}{kT}-\ln(\frac{\Lambda^3}{V}) \quad . \tag{2.29}$$

It should be noted that according to equation 2.29 performing GCMC simulations at constant B, V and T are equivalent to constant μ, V, T simulations at the corresponding value of μ.

2.6 Molecular dynamics simulation

In molecular dynamics sample configurations are created by solving the Newtonian equations of motion for each step of a simulation for a system consisting of *N* particles, whose interactions are given by a potential *V*. The equations of motion are usually expressed according to the Lagrangian formalism:

$$\frac{d}{dt}[(\partial L(\bar{q},\bar{p})/\partial \bar{p})-(\partial L(\bar{q},\bar{p})/\partial \bar{q})]=0 \quad , \qquad (2.30)$$

where $L(\bar{q},\bar{p})$ is the so called Lagrange function of the system, that depends on the generalized spatial coordinates $\bar{q}$ and the generalized momenta $\bar{p}$ of the particles constituting the system. In another formulation the Lagrange function can be written as the sum of the potential and kinetic energy terms.

$$L(\bar{q},\bar{p})=K-V \quad , \qquad (2.31)$$

where *K* is the kinetic energy of the system, expressed as it has been shown in equation 2.2 and *V* denotes the potential energy, which, as it has been already discussed in section 2.4., consists of the effect of an external field on the individual molecules, the pair interactions, three-body and higher order terms. It has also been stated in section 2.4. that this potential may be approximated as the sum of the one-particle term, an effective pair potential and a Coulomb term, which accounts for the electrostatic interactions.

Substituting the above-mentioned kinetic and potential energy expressions into equation 2.31 and performing the derivations allow us to obtain the following expression, well-known from classical mechanics, for the F_i forces acting on the individual particles:

$$F_i=m_i\ddot{r}_i \, , \qquad (2.32)$$

where r_i is the position vector of the i^{eth} particle expressed in the Cartesian frame of coordinates. During the course of a molecular dynamics simulation we may obtain the new coordinates by solving 3*N* of this second order differential equation in every time step. Alternatively 6*N* of the following joint differential equation, which can be derived from equation 2.32, may be solved:

$$\dot{r}_i = \frac{p_i}{m_i} \qquad\qquad \dot{p}_i = F_i \tag{2.33}$$

Several algorithms, based on both of the above described pathways have been developed for performing molecular dynamics simulations. One of the most well-known among them is probably the Verlet algorithm[24], which is based on equation 2.32. This algorithm is used also by the program package applied for our molecular dynamics simulations, thus this method will be described in details hereinafter. As the first step of the calculation, position vectors are written as their Taylor expansion according to time:

$$\begin{aligned} r_i(t+\Delta t) &= r_i(t) + \Delta t\, \dot{r}_i(t) + \frac{(\Delta t)^2}{2!}\ddot{r}_i(t) + \frac{(\Delta t)^3}{3!}\dddot{r}_i(t) + \dots \\ r_i(t-\Delta t) &= r_i(t) - \Delta t\, \dot{r}_i(t) + \frac{(\Delta t)^2}{2!}\ddot{r}_i(t) - \frac{(\Delta t)^3}{3!}\dddot{r}_i(t) + \dots \end{aligned} \tag{2.34}$$

By adding the above two equations we get:

$$r_i(t+\Delta t) + r_i(t-\Delta t) = 2\dot{r}_i(t) + \Delta t^2 \ddot{r}_i(t) + \dots \tag{2.35}$$

from where $r_i(t+\Delta t)$ may be expressed. After neglecting higher than second order terms and expressing the second order derivatives according to equation 2.34., we obtain the following expression for $r_i(t+\Delta t)$:

$$r_i(t+\Delta t) = -r_i(t-\Delta t) + 2r_i(t) + \frac{(\Delta t)^2}{m}\sum_{i\neq j} F_{ij}(t) \quad , \tag{2.36}$$

where F_{ij} is the force exerted on particle *i* by particle *j*. The v_i velocity of particle *i* can be calculated as the time derivative of its position vector, and thus it can be expressed in the form:

$$v_i = \dot{r}_i = \frac{1}{2\Delta t}[r_i(t+\Delta t) - r_i(t-\Delta t)] \quad . \tag{2.37}$$

All things considered, according to the Verlet algorithm the spatial coordinates of the individual particles in the following time step of the simulation, that is at the time (t+Δt), may be calculated from their current spatial coordinates, r_i and instantaneous value of their acceleration, expressed as

$$a_i(t)=\sum_{i\neq j}\frac{F_{ij}}{m_i} \quad . \tag{2.38}$$

Calculating other properties may however necessitate the knowledge of the v_i velocity vector of the particles constituting the system as well.

2.7. The importance of intrinsic surface analysis

An interface, especially if it separates two fluid phases from one another has a complex microscopic structure. In an atomistic resolution an interface is by no means planar and its composition and geometry vary in time. Thus if one wishes to investigate the interfaces of two fluid phases their study should always begin either by determining the covering surface by a conveniently chosen mathematical function or by finding the list of the molecules building it up for each sample configuration. (The origin of the complexity of fluid interfaces and methodological development in this field is discussed in Chapter 4.1.1 and 4.1.2. in details)

2.7.1 The ITIM method

The ITIM (Identification of the Truly Interfacial Molecules) method[25] has been proven to be one of the most suitable methods for routine analysis of the interface as it is a good compromise between computational cost and accuracy. This method has been developed previously in our group. Its concept is simple, the interface is mapped by dropping a probe sphere of radius R_p along a set of test lines parallel to the normal vector of the macroscopic plane of the interface. If a molecule is hit by the probe sphere, it is considered interfacial. It should be noted here that in this analysis the atoms building up our system of interest are represented as spheres whose radius is equal to the atomistic Lennard-Jones σ parameter. If this algorithm is performed along a set of testlines covering the entire surface of the basic simulation box, we get the full list of interfacial molecules. Moreover repeating the analysis n times on the system provides us with the list of molecules constituting the second, third, n^th molecular layer, which makes it possible to examine the depth profile of several properties of the interface, and it eventually enables us to draw consequences about the depth to which interfacial surplus properties can exert their effect.

Obviously the ITIM method (as any other methods aimed at determining the intrinsic surface) contains an inherent free parameter, which is the radius of the probe sphere R_p. The choice of R_p is crucial in detecting the real interface properly, as if it is chosen to be too big it will not be able to detect all the surface molecules as it will be excluded from well smaller than its size, on the other hand if it chosen to be too small. It has been shown that there exists an optimal R_p, for which the list of interfacial molecules will be determined with a highest possible accuracy, and this value, as it could be anticipated from the nature of the free parameter, is in the order of magnitude of the atomic radii of the molecules of our system of interest.

2.7.2 Properties of the intrinsic interface

Knowing the full list of interfacial molecules allows us to calculate several structural and dynamic properties of the intrinsic surface, such as the composition of the surface layer, the roughness of the surface or the dynamics of exchange between the interface and the bulk, and of interfacial molecules, such as their orientational preferences or the possibility of their lateral aggregation. Calculating the molecular composition of the surface layer knowing the full list of interfacial molecules to get information about the surface activity of our components is a trivial task, however acquiring any of the other above mentioned examples of interfacial properties necessitates performing non-trivial data processing and analyzes.

2.7.2.1 Collective properties of the surface

The roughness of an interface is directly related to its interfacial tension. Since the origin of the surface roughness is indeed a periodic perturbation of the original interface (see Chapter 4.1.1), it can be fully described by the joint analysis of an amplitude (a) and frequency-like parameter (ξ) on the analogy of waves. These parameters can be obtained by fitting the

$$\bar{d}=\frac{a\xi l}{a+\xi l} \tag{2.39}$$

function to a curve obtained as result of plotting the normal distance $\bar{d}$ between two points of the interface as a function of the distance between them in the plane of the interface (l).

Another interesting question in studying the entire interface is its dynamic behavior. If the sample configurations have been obtained from MD simulations, the dynamic changes of the interface may also be calculated from the results of the ITIM analysis. Interfacial dynamics are described by the $L(t)$ and $L^0(t)$ continuous and intermittent survival probabilities of the components of our system of interest. The $L(t)$ survival probability can be determined by calculating the probability that if a molecule is at the surface at a time t_0 it will be found at the surface also at the time (t_0+t). While the $L^0(t)$ function is obtained by a similar algorithm, with the exception, that in this case the molecule may leave the surface for a while, given that it returns within a number of configurations it will still be considered as interfacial. (Note that neither are the $L(t)$ curves fully continuous, their intermittence time is the time interval separating two configurations). Repeating the above described procedures for a set of t values covering the time span of the simulation and fitting exponentially decaying functions:

$$L(t)=\exp(-t/\tau) \qquad L^0(t)=\exp(-t/\tau^0) \tag{2.40}$$

to the $L(t)$ or the $L^0(t)$ curve will give the continuous and the intermittent survival probability or residence time (τ, τ^0) of the molecules at the surface.

2.7.2.2 Characterization of the interfacial molecules

The orientation of the molecules situated at the surface may also be calculated given the full list of interfacial molecules. Describing the orientational distribution in case of rigid molecules leads us to the problem of calculating a bivariate joint distribution function. The polar coordinates θ, ϕ of the normal vector X of the interface in a molecule fixed Cartesian frame have been proven to be good choice for determining the orientational distribution of the interfacial molecules. It should be noted that as θ is the angle of two spatial vectors whereas angle ϕ is enclosed by two vectors in the plane, the bivariate joint distribution of $\cos\theta$ and ϕ will be uniform only if the orientation of the molecules is independent from the direction of the surface normal vector.

On the other hand, the question of possible lateral aggregation can also be conveniently studied given that we have information about the coordinates of all the molecules constituting the interfacial layer. The most convenient method to detect the self-aggregation of molecules at the interfaces is based on the two dimensional Voronoi tessellation of the surface.[26] In a two-dimensional assembly of seeds the Voronoi polygon (VP) of a given seed is the locus of points which are closer to this seed than to any other one.[27] Therefore, the VPs of a (planar) system fill the plane without gaps and overlaps. If the seeds represent molecules at the surface, the VP of a given molecule can be assigned to the excluded surface area belonging to this molecule. Conversely, the reciprocal VP area measures the local surface density around this particle. If the molecules are uniformly distributed at the surface, the distribution of their VP area follows a Gaussian shape. However, if their distribution is such that the lateral density shows large fluctuations, the VP area distribution exhibits a long, exponentially decaying tail at large area values.[28] Considering these facts, the following strategy can be used to detect, for instance, self-aggregation of the adsorbed molecules at solid or fluid surfaces. We calculate the two dimensional VP area distribution by considering only one of the components of the system, disregarding the other. If this component is uniformly distributed, the resulting VP area distribution must be of Gaussian shape. However, if they form large self-aggregates, the removal of the molecules of the other component from the system will lead to the appearance of empty areas, and consequently the VP area distribution will show an exponentially decaying tail at larger areas. This effect is usually stronger if the major component of the system is disregarded, as in this case larger spaces are left unoccupied. The VP area distributions of these sets of points have been calculated by the algorithm of Ruocco, Sampoli and Vallauri.[29]

2.8 Calculation of the free energy and of free energy profiles from simulations

The characteristic function of the canonical ensemble is the Helmholtz free energy whose value dictates the direction of spontaneous processes and the stability of the individual states. The Helmholtz free energy A is the function of the canonical partition function Q:

$$A = -k_B T \ln Q \quad . \tag{2.41}$$

As a consequence of its definition, the Helmholtz free energy cannot be calculated directly from the simulations as a time or ensemble average since it would require the knowledge of the entire partition function Q which is computationally impossible to achieve.

Several methods have been described in the literature to overcome this problem, most of which use the trick of calculating the actual free energy difference between two well-defined points of the phase space, which only requires the sampling of the part of the phase space which differs significantly in case of the initial and the final states:

$$\Delta_a^b A \equiv A_b - A_a \quad , \tag{2.42}$$

where A_a is the free energy of state a whereas A_b is that of state b. The easiest way to obtain the free energy difference between two physically distinguishable states is to calculate the ratio of the number of configurations N_a and N_b in state a and that in state b. Knowing this ratio the free energy difference of the two states will be simply expressed as[30]:

$$\Delta_a^b A = -k_B T \ln\left(\frac{N_b}{N_a}\right) \quad . \tag{2.43}$$

This method yields a good approximate of the free energy difference only if both states appear in the sample a statistically relevant number of times. If it is not the case, we may use integration [31] or perturbation methods [32] to obtain the free energy difference in question. These techniques imply a coupling parameter in the Hamiltonian which connects the initial and the final states. Integration methods express the free energy difference as the integral of the work required to go from the initial to the final state with respect to the coupling parameter λ:

$$\Delta_{\lambda_a}^{\lambda_b} = \int_{\lambda_a}^{\lambda_b} \left\langle \frac{\partial U(\lambda)}{\partial \lambda} \right\rangle_{\lambda} d\lambda \quad , \tag{2.44}$$

where $U(\lambda)$ is the coupling parameter dependent energy of the system. Perturbation methods on the other hand express the path along the coupling parameter by small differential changes in its value.

The above described techniques are useful if we want to calculate a single free energy value, for example the free energy of solvation of a certain solute in a given solvent. In a number of cases, however, knowing the entire free energy profile along a reaction coordinate R describes a process more exactly than a single relative free energy value. The reaction coordinate R is often chosen as an N dimensional hypersurface which is a subspace of the total configuration space, in other words $R= R(r_1,r_2,\ldots,r_N)$, where r_i are the spatial coordinates of the particles in the system. The free energy as a function of the reaction coordinate R can be given by the following equation:

$$A(R) = -k_B T \ln P(R) + C \quad , \tag{2.45}$$

where C is an additive constant and $P(R)$ is the probability of finding our system at given point of the reaction coordinate. The task to be performed in order to obtain the free energy profile is to determine the value of $P(R)$. This can be done in theory by counting directly the number states along the reaction coordinate from an unbiased simulation, however in this method only relatively low-energy configurations can be properly sampled, whereas high-energy ones will be represented poorly in the trajectory. Thus direct counting will not be suitable for instance for calculating the free energy profile of a particle along a path which goes from a phase in which it is soluble to an opposite phase in which it is not. A widely used solution to overcome the problem of poor sampling is to do biased simulations to increase the number of configurations which lie on the reaction coordinate. In umbrella sampling[33], for example, an additive bias potential is introduced to the Hamiltonian. It is also possible to obtain the free energy profile by doing a set of simulations in which the system is forced to stay on the hyperspace described by R.[34] A variety of this latter method, which I have used during my work, is called the potential of mean force (PMF) and is described in details in the following section.

Before going into the details of the PMF method it should be noted that in the recent years several non-equilibrium methods, such as steered molecular dynamics[35] or metadynamics[36], together with equilibrium methods which use accelerated sampling techniques like parallel tempering[37] have been developed to facilitate fast and effective free energy calculations.

2.8.1 The potential of mean force (PMF) method

The original concept of the potential of mean force has been established by Kirkwood in as early as 1935.[38] According to his definition, in a system consisting of N particles the PMF can be defined strictly as the potential that gives the average force over all the possible configurations of particles (n+1), (n+2),...,N acting on a particle i, with the constraint that particles 1,2,...,n are kept fixed

$$-\Delta_j \omega^{(n)} = \frac{\int dq_{n+1} \ldots d\, q_N \exp[-\beta U(\bar{q})][-\nabla U(\bar{q})]}{\int dq_{n+1} \ldots d\, q_N \exp[-\beta U(\bar{q})]} \equiv \langle F_C \rangle \qquad j=1,2,\ldots.,n \quad , \tag{2.46}$$

where $-\nabla_j \omega^{(n)}$ is the ensemble average of the force (F_C) exerted on the jth particle by all N-n non-fixed particles, and therefore $\omega^{(n)}$ is the Potential of Mean Force (PMF). In most of its applied varieties n =2 that is the distance of two particles are kept fixed.

This concept allows us to estimate free energy profiles from a (constraining) force depending on a reaction coordinate, exerted on the system to force it to stay on the subspace determined by R. In the framework of our simulations, the derivative of the free energy (A) is calculated as the average of the constraining force:

$$\frac{d\, A(R)}{dR} = -\langle F_C(R) \rangle \quad , \tag{2.47}$$

where brackets denote ensemble averaging over each constrained simulation. Integrating Equation

2.47 along the reaction coordinate *R* yields the following expression for the free energy difference of state *a* and *b*, both of them lying on the reaction coordinate:

$$\Delta_{R_a}^{R^b} A = -\int_{R_a}^{R_b} dR \langle F_C(R) \rangle \quad . \tag{2.48}$$

It can be easily demonstrated that calculating the free energy along a set of different values of the R_C reaction coordinate chosen to model a physically meaningful pathway enables us to obtain the free energy profile of the process described by this particular set of *R*. In practice, the *R* reaction coordinate is usually chosen as a fixed distance between two points of the system.

This method is traditionally applied to reconstruct the free energy profile of the transfer of a single penetrant across a liquid/liquid interface along a one dimensional path parallel to the interface normal axis in the following way. A number of simulations with the penetrant located at different positions along the interface normal axis is performed on the canonical (*N*,*V*,*T*) ensemble, with a constraining force (F_C) fixing its distance from the center of mass of the system. The magnitude of the projection of the force to the reaction coordinate is recorded in every time step of each of these simulations, yielding a set of $F_C(t)$ values for every value of the *R* reaction coordinate. This way, for each position of the ion along *R* the time average of the force, $<F_C(R)>_t$, can be obtained by simply averaging the force over all the steps. Finally, the free energy profile is calculated by integrating the time average of the forces according to equation 2.48, and is conventionally interpreted with respect to the macroscopic plane of the interface, namely by anchoring the origin of the obtained free energy profile (i.e.: the point where the value of the reaction coordinate is equal to zero) to the position of the Gibbs dividing surface.

2.8.2 The intrinsic potential of mean force method

2.8.2.1 The importance of the intrinsic treatment of the interface in free energy calculations

Knowing that an interface of two fluid phases is neither flat nor invariant in time, it can be assumed that the classical way to reconstruct the free energy profile characterizing the transfer of a particle from one phase to another is burdened with systematic error of unknown magnitude originating from identifying the interface with its macroscopic plane. Having the intrinsic surface itself determined, the profile of any physical quantity can, in principle, be calculated relative to this surface. In theory it is also possible to reconstruct the free energy profile relative to the intrinsic interface, however, to the best of our knowledge, such intrinsic analysis has never been published. A part of my PhD studies has been dedicated thus to developing such a method.

The basic difficulty of the question lies in the fact that the calculation of the free energy profile is by itself a computationally demanding task. In reconstructing the intrinsic free energy profile, however, this already considerable computational cost is further increased by the requirement of determining the intrinsic surface for – in principle – every sampled configuration. Our method is based on the idea that such calculations do not require the determination of the *entire* intrinsic surface, just a small portion of this surface that lies right behind the penetrant. When using the ITIM method it means that instead of checking the full set of test lines in the entire basic box only a few of them, located at the close vicinity of the penetrant has to be investigated.

2.8.2.2 A protocol to calculate the intrinsic free energy profile

Our method is built up of four main consecutive steps. First of all, the set of constrained simulation is carried out such that the reaction coordinate R is chosen to transfer the penetrant along a one dimensional path parallel to the interface normal axis from phase A to phase B, and the constraining force is collected. Then the ITIM analysis is carried for each saved configuration of every simulation. The ITIM analysis and subsequent determination of the intrinsic instantaneous distance between the ion and the interface provides us with an intrinsic ion-interface distance as a function of time ($x_i(t)$) for a given configuration for which the corresponding constraining force $F_C(t)$ has been recorded at for every sampled configuration. From these data one can readily obtain the constraining force as a function of the intrinsic distance ($F_C(x_i)$) simply by merging the intrinsic $x_i(t)$ function obtained during the course of the ITIM analysis with the $F_C(t)$ function. For the sake of a mathematically correct treatment, the original simulation box is then divided into slabs parallel with the macroscopic plane of the interface, whose width is equal to the displacement effectuated between two consecutive constrained force runs. Each $\{F_C(x_i),x_i\}$ pair is then assigned to the corresponding the slab according to the value of x_i and the forces belonging to one slab are averaged within each separate slab to obtain $<F_C(x_i)>_{slab}$. The cumulative integral of the slab averages of the intrinsic forces $<F_C(x_i)>_{slab}$ as a function of the average slab position, i.e.: the x coordinate of the midpoint of the slab, is then calculated to give the intrinsic free energy profile of transfer.

2.8.2.3 Technical questions of the intrinsic PMF method

2.8.2.3.1 The speed of the ITIM algorithm

The ITIM analysis, even though one of the fastest among the similar methods, has turned out to be computationally too costly to analyze a greater number of trajectories simultaneously on a reasonable time scale. Thus, prior to applying it for free energy profile calculations the algorithm had to be simplified to reduce the computational cost. The basic idea that enabled us to reduce the above mentioned cost of the original ITIM algorithm substantially when calculating the intrinsic profile of one single penetrant is the following. Since it is only the exact distance of the penetrant from the intrinsic surface that has to be determined, it is sufficient to know the position of this surface at one particular point of the *YZ* plane (i.e.: the macroscopic plane of the interface), namely where the penetrant is also located. Therefore, here we modified the original ITIM algorithm as follows. Differently from the original idea of using a uniformly distributed fine grid of test lines across the entire *YZ* plane, for the purpose of reconstructing the intrinsic PMF we use only a few crucial test lines, located in the vicinity of the penetrant, to map solely the relevant section of the intrinsic surface. The position of these crucial testlines is determined on the fly, during the ITIM analysis based on their lateral distance (i.e. the distance in the *YZ* plane of the simulation box) from the position of the ion, and it is refreshed for every analyzed frame. Those test lines whose lateral distance from the center of mass of the penetrant is smaller than or equal to $N \times d_{\text{grid}}$ are considered as crucial testlines, whereas all the other test lines are disregarded from the analysis. Here N is a conveniently chosen small integer, leading to the use of N^2 crucial testlines around the ion, and d_{grid} is the spacing of the grid lines, the optimal spacing of which is discussed in detail by Jorge et.al. [39] Performing the ITIM analysis along only the set of crucial testlines results in the list of the few (practically 5-10) truly interfacial molecules whose distance in the *YZ* plane is the shortest from the *YZ* position of the ion

2.8.2.3.2 Methods to determine the distance of a point from the intrinsic surface

Knowing the position of the penetrant and the molecules of the instantaneous intrinsic interface which lie laterally in the vicinity of the penetrant allows us to reconstruct the intrinsic free energy profile, as several mathematically well-established methods are at hand to calculate the real intrinsic distance between the penetrant and the interface along the surface normal axis. The two most accurate of these methods, namely Voronoi method and triangular interpolation, have been tested. In the Voronoi method, the intrinsic distance in the normal direction is defined as the normal distance of the center of mass of the penetrant and the molecule whose lateral distance is the smallest from the ion, that is the molecule whose two dimensional Voronoi cell contains the projection of the penetrant in the XY plane.[40] Triangular interpolation, on the other hand takes into account the three closest interfacial molecules, which are situated in a way that the *YZ* projection of the penetrant falls into the area of the triangle. The intrinsic distance along the interface normal in this case is calculated as the distance of the center of mass of the penetrant from the plane determined by this triangle. All things considered, while in the Voronoi method the corrugated surface is approximated by the Voronoi cell of the interfacial molecules, the triangular interpolation uses small triangles to create a mathematically manageable covering surface. A comparison of the two methods is shown in Fig. 2.1.

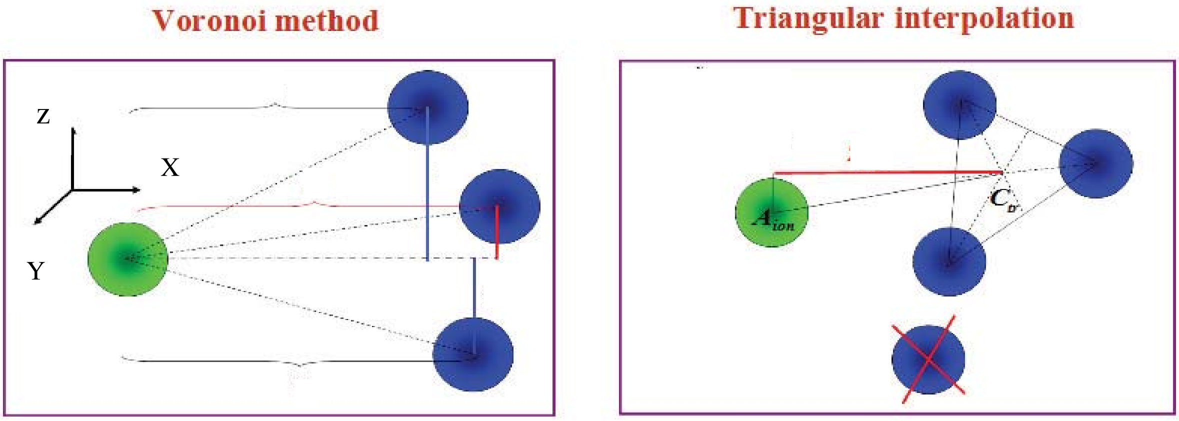
Voronoi method

Triangular interpolation

If for $\forall j \in 0, nwat_{surf}$

$\sqrt{Y_j^2 + Z_j^2}$ **is minimal then** $X_{\text{int}} = X_{\text{j}}$

$$X_{\text{int}} = A_{\text{ion}}(X) - C_{\text{rt}}(X)$$

Figure 2.1. *Comparison of the concept of the Voronoi method (left panel) and the triangular interpolation (right panel), green spheres represent the penetrant while blue spheres are the interfacial molecules, the intrinsic distance is indicated in red and the interface normal vector points in this case, differently in the X direction.*

2.8.2.3.3 The problem of the hydration shell

When calculating the intrinsic free energy profile of transfer by the above described procedure one has to be aware of the experimentally proven fact that the first hydration shell is usually co-extracted with the penetrant as it moves towards the organic phase. It has to be taken into account that the water molecules constituting the hydration shell can be considered as part of the intrinsic interface only if the shell is still attached by hydrogen bonds to the bulk aqueous phase. In cases when the hydration shell of the penetrant is already detached from the interface, that is when the penetrant has already penetrated deep enough into the bulk organic phase, the consideration of these molecules among the interfacial ones leads to a severe theoretical error in the calculation. Practically, the ITIM method is certain to find these molecules to be the closest interfacial ones, thus the penetrant will seemingly never leave the interfacial region. This, in other words, means that the ion's behavior in the bulk organic phase will never be correctly sampled. To avoid this kind of theoretical error, we have to disregard molecules of the hydration shell from the analysis in cases when they form separate body which is not connected to the hydrogen bonded network of the aqueous phase. However, one has to consider how to differentiate between the above mentioned two cases. A trivial approach to this question might be to introduce a cutoff position along the X axis, beyond which we disregard the water molecules from the analysis. This cutoff distance can be conveniently chosen by simply looking at the total mass density profiles of the bulk aqueous and the bulk organic phase and taking the position of the Gibbs dividing surface with an additional safety zone width. However, if the penetrant is situated very close to the interface, the attachment – detachment process might be reversible. More precisely, in some configurations the penetrant might be surrounded by a separate hydration shell on the organic side of the interface, and, due to the fluctuations of the surface, this shell maybe reattached to the aqueous phase to form a water finger, which means that the penetrant can re-enter the aqueous phase and the hydration shell will again contribute to the interface. An example of the above phenomena observed during our studies is shown in figure 2.2.

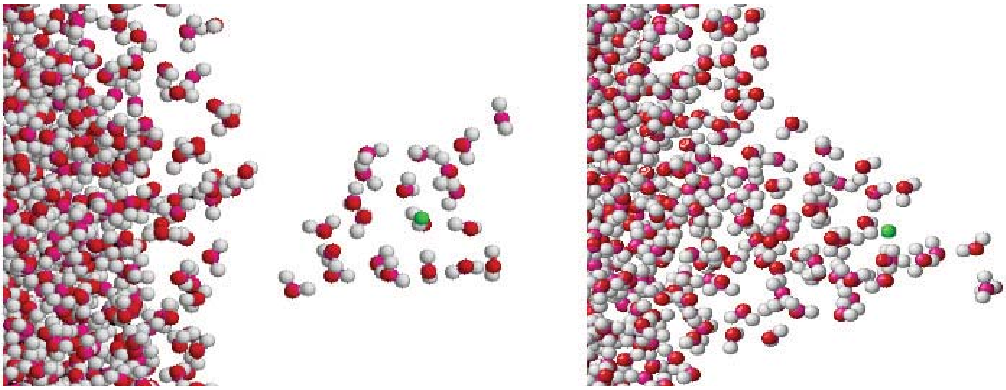

***Figure 2.2**. Instantaneous snapshots of two consecutive sample configurations taken from one of our simulations. The snapshot on the right (taken in the earlier step) shows a separate hydration shell, which however in the next sampled configuration (right panel) is reattached to the interface.*

Obviously, by using a uniform cutoff beyond which we disregard the hydration shell molecules from our analysis, we neglect these situations. However our approach will be more accurate if we take the above described process into account.

The solution to circumvent the systematic error caused by neglecting the occurrence of the above mentioned phenomena is to perform a cluster size analysis on each of the configurations. This method which has been already described in [41] proved to be a feasible way of deciding if the hydration shell is separated from the aqueous phase or forms a part of it. The cluster analysis is carried out as follows. First, the molecules constituting the hydration shell have to be identified by a neighbor searching algorithm which selects the water neighbors of the penetrant by comparing their c.o.m. – c.o.m. distance to the abscissa value of the first minimum observed in the corresponding radial distribution function. Those water molecules whose distance from the penetrant is shorter than the above mentioned value are selected as members of the hydration shell and are further analyzed to find the largest water cluster to which they belong. If any of the molecules constituting the hydration shell belongs to a water cluster which consists of a larger number of molecules then three times the ion's average hydration number in the bulk aqueous phase, then the hydration shell is considered as part of the interface. Otherwise it is treated as a separate droplet, and is thus disregarded from further analysis. We should also note here that, for the sake of reducing the computational cost of the otherwise quite costly neighbor-searching method, finding the first water molecule belonging to both the hydration shell and the bulk aqueous phase stops algorithm.

Chapter 3

Solid interfaces

3.1 Properties of solid surfaces, adsorption

An ideal solid surface is considered to be an atomistically flat monolayer of a constant surface area consisting of particles whose orientation is fixed, having only vibrational degrees of freedom, and whose exchange with molecules of the bulk phase is hindered. Nevertheless, solid surfaces are usually far from being ideal, even crystal surfaces can be „contaminated" by several inhomogeneities, both geometrical and energetic. These inhomogeneities together with the generally valid fact that a solid surface cannot minimize its surface excess energy by contracting itself to a minimal area explain that most solid surfaces are relatively good adsorbents, since the only way to minimize the excess energy of a solid surface is to trap molecules (adsorbates) from the opposite phase. It has been proven experimentally that under certain conditions adsorption of such inert compounds as N_2 or noble gases occurs on surfaces to minimize their surface excess Gibbs free energy.[42,43]

Adsorption occurs if the change in the Gibbs free energy accompanying the process is negative:

$$\Delta_{free}^{ads} G = \Delta_{free}^{ads} H - T\,\Delta_{free}^{ads} S < 0 \quad , \tag{3.1}$$

where *G* is the Gibbs free energy of the adsorbed (*ads*) and the non-adsorbed (*free*) system, *H* is the enthalpy, S is the entropy and T is the thermodynamic temperature. Adsorption at solid surfaces is, by nature, accompanied by the decrease in entropy because adsorbed molecules have fewer degrees of freedom than molecules in the gas phase, thus ΔS will always be negative which means that the decrease in the enthalpy should overcompensate this effect in order for adsorption to happen. Consequently, all factors which minimize the effect of the decrease in the entropic contribution, such as low temperature for instance, or those which maximize the effect of the enthalpic term, for example the increased reactivity of the free solid surface, facilitate adsorption processes.

On a general scheme adsorption at a solid surface can be described as the sequence of a number of steps. The first one among them is the transport of the adsorbate to the surface, which can happen by diffusion in the simplest case in the lack of convective transport. Then the adsorbed molecule gets into contact with the solid surface, after which possible structural and chemical rearrangements of both the adsorbent and the adsorbate may take place. These rearrangements can be followed by desorption in case of *physisorption* (a reversible process which does not involve the breakage of a chemical bond neither in the adsorbent nor in the adsorbate). In case of *chemisorption* the breakage of chemical bonds and formation of new ones as a result of the contact with the adsorbent happens and the adsorption process is considered irreversible. Under certain conditions surface induced conformational changes of the adsorbed molecules may also be observed. It should be noted that the possible porosity of the adsorbent further elaborates the general adsorption scheme, as in such cases adsorbates have to penetrate into the pores by diffusion. It happens for instance if the adsorbate is zeolite a material widely used in a separation science and catalysis. [44] Figure 3.1 shows the general schemes of adsorption from a fluid phase at a non-porous solid surface.

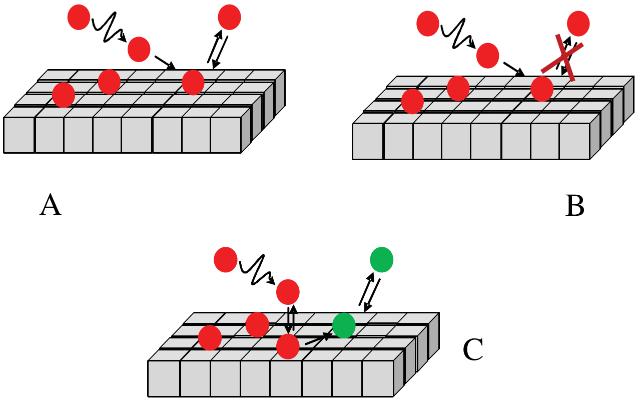

Figure 3.1. *General adsorption schemes at solid surfaces. a) shows the case of simple reversible physisorption, b) shows the case of chemisorption, whereas c) illustrates the case when conformational changes are induced in the adsorbate as result of the interaction with the surface.*

Measuring or calculating isotherms is the most straightforward way of the quantitative investigation of adsorption processes. Adsorption isotherms can be constructed by recording the amount of adsorbate per unit area of the adsorbent expressed as a function of its amount in the fluid phase in contact with the solid surface. It is a commonly used technique to construct adsorption isotherms by simply measuring the amount of the adsorbate in the fluid phase before and after bringing it to contact with the adsorbent surface. The adsorbed amount is then obtained as the difference between the above-mentioned two quantities and plotted against the original amount of adsorbate in the gas phase. The shape of the isotherms is determined largely by mechanism of adsorption and can thus yield valuable information about the details of the process. Several theoretical models exist for the mathematical description of adsorption isotherms. The most common among them is the so called Langmuir model.[45] The Langmuir model is valid for physisorption at atomistically flat surfaces whose interaction sites are equivalent, with the condition that no lateral interactions are formed between the molecules in the adsorption layer, which is strictly monomolecular. In such cases the adsorbed amount, can be expressed as:

$$\Theta=\Gamma/\Gamma_m=\frac{bp}{1+bp}\ , \tag{3.2}$$

where Θ is the surface coverage, that is the ratio of the actual adsorbed amount (Γ) and the amount needed for a complete monolayer coverage (Γ_m), p is the concentration in the fluid phase (expressed as partial pressure if the adsorbate is in the gas phase) and b is the so called sorption constant which is proportional to the ratio of the rates constant of adsorption (k_a) and that of desorption (k_d):

$$b=\frac{k_a}{k_d\exp(-E_a/RT)}\ , \tag{3.3}$$

E_a and R being the activation energy and the universal gas constant, respectively. Other adsorption models describe more complicated schemes, for example the B.E.T (Brunauer – Emmett – Teller) isotherm[46] accounts for the formation of more than one adsorbed layers whereas the Freundlich[47] and the Temkin[48] isotherms describe surface inhomogeneities and adsorbate-adsorbate interactions, respectively.

We have already mentioned that during the course of adsorption conformational changes are often induced in the adsorbate, especially if organic molecules are concerned. Their adsorbed geometry is usually markedly different from the gas phase equilibrium structure, due to the presence of interactions with the adsorbent surface, as well as to the lateral interactions between the adsorbed molecules in case of a non-Langmuir-like behavior. Surface sensitive measurements, such as FTIR are capable of determining these conformational changes as well as the orientational preferences of the adsorbed layers by comparing the spectra of molecules bonded to the surfaces with that of the free molecules. However, such measurements are always burdened with noise, and their accuracy is limited by the precision and the resolution of the instrument. Computer simulations on the other hand can provide us directly with atomistic-scale information about the structure of the adsorbed layer as well as the conformational changes occurring due to vicinity of the surface and the neighboring adsorbates for the model system. Moreover, GCMC simulations are suitable for calculating entire isotherms.

3.2 The importance of ice surfaces in environmental chemistry

Solid interfaces are known to participate in several processes in environmental chemistry. Ice surfaces, in particular, play an outstandingly significant role in promoting chemical reactions in the atmosphere. Their importance has been discovered together with the discovery of the Antarctic ozone hole, and since then interactions of trace gases with ice surfaces in the Earth's atmosphere have been attracting an ever growing interest. If we look at the different layers of the atmosphere, we will find that ice surfaces are abundant at every altitude. The structure of the atmosphere is illustrated in Figure 3.2.

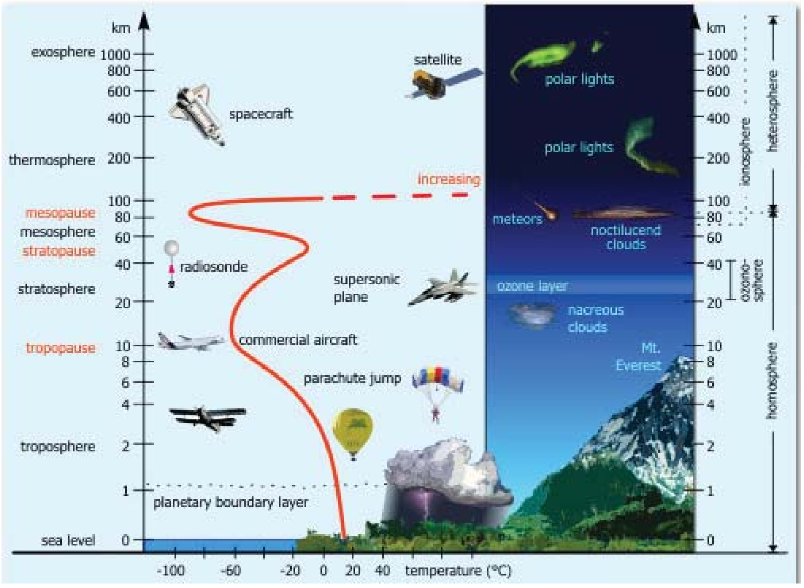

Figure 3.2 *Illustration of the layers of the atmosphere together with their characteristic amplitude a temperature values.*[211]

Stratospheric ice particles are mostly parts of PSCs (polar stratospheric clouds) and they are known to catalyze the transformation of non-reactive reservoir species of chlorine, e.g.: CFCs which have a mean-lifetime long enough to cross the boundary between the troposphere and the stratosphere, to their active form responsible for the formation of the ozone hole above the polar areas. Ice surfaces present in the icy clouds of the upper troposphere (UT) are also of great importance since they can scavenge volatile organic compounds (VOCs), nitrous oxides (NO_x) or CO. In their bound form, VOCs can be readily oxidized to yield HO_x radicals, while the latter two types of species undergo photochemical oxidation by the sunlight. These radicals are important sinks of ozone in the troposphere. It should also be noted that ice as a main component of the snowpack at the ground level has a similar effect on the VOCs and NO_x species emitted from anthropogenic or natural sources. However the photochemical reaction of these compounds, eventually leading to ozone formation at the boundary layer, that is the layer of the atmosphere which is closest to the Earth's crust, is a harmful process, since ozone at this lowest part of the troposphere is known to act as GHG and has also severe health hazards.

The first step of the photochemical reactions leading to the formation of ozone is necessarily the adsorption of the precursors on ice invoking such changes in the structure of the molecules that increase their reactivity. Thus the investigation of adsorption phenomena at ice surfaces under atmospheric conditions at an atomistic resolution may deepen our knowledge about crucial questions of atmospheric chemistry. A large number of studies have been devoted to investigating the adsorption of nitrated and halogenated species on ice. Much less attention has been paid however to small molecular VOCs which, as it has been seen previously, are yet important factors in the chemistry of the atmosphere.

3.3 The role of clouds in atmospheric chemistry

As it has been seen, ice surfaces affect the chemistry of the atmosphere as catalysts speeding up reactions which in the gas phase would be too slow to proceed at a perceivable rate. A considerable fraction of the total surface of atmospheric ice is present in clouds of the stratosphere and the troposphere. It is a well-known fact that the so called Polar Stratospheric Clouds (PSCs) are formed under very dry conditions during polar winters solely above the arctic regions. They have two basic types, type I PSCs contain water and nitric acid hydrates, or alternatively they can be ternary mixtures of water, nitric acid and sulfuric acid, type II PSCs on the other hand consist of pure water ice. Type II PSCs are iridescent and responsible for the nacreous colors of the polar light. Tropospheric clouds on the other hand may have various forms and may consist either of small water droplets or of ice grains. They are usually categorized by their shape. Layered clouds are called stratos, bulky thick water clouds belong to the cumulus group, whereas cirrus clouds look like greyish-white translucent threads crossing the sky. Cirrus clouds in the UT are usually icy clouds which cover on average 25% of the surface of the Earth. Their importance lies in their net heating effect which is due to the fact that these thin and translucent networks of ice nuclei absorb a considerable percentage of the outgoing infrared radiations of the Earth while they reflect only a negligible fraction of the incoming IR rays of the sun. A cirrus cloud with an average thickness of 100 m absorbs on average 50% of the outgoing IR radiation, while it reflects only 9% of the incoming rays, and thus heats up the surface it cover by as much as 10 °C[49] which suggests that these kind of clouds can probably be considered as significant contributors to global warming.

3.3.1 Aerosol particles as cloud condensation nuclei

Aerosol particle are small aggregates of molecules suspended in the atmosphere whose size ranges between a few nanometers and 100 µm. They can be composed of organic or inorganic compounds, however their composition depends on the way of production. In general, the predominant chemical components of air particulate matter are sulfates, nitrates and ammonium salts, sea salt, mineral dust, black carbon and organic compounds, whose relative abundance depends on, e.g., location, time, and meteorological conditions. [50] Due to their colloidal size they alter the light scattering properties of the atmosphere which results in an overall cooling effect. On the other hand, organic aerosols in particular have a tendency to trap water molecules by the reactive groups of their surface, promoting the formation of binary aerosol particles, which are, in turn known as ice (IN) or cloud condensation nuclei (CCN). This latter statement implies that binary aerosols have an indirect heating effect on the atmosphere, due to the fact that cirrus clouds are formed usually by heterogeneous nucleation of such particles and, as it has been described in the previous section, they are known to increase the IR absorbance of the tropospheric region significantly.

Investigating the interactions of water molecules with organic aerosols is thus another field of major interest in atmospheric chemistry. [51] Organic aerosols are most commonly formed by the aggregation of VOCs, which are emitted into the atmosphere on a daily basis in vast amounts from both natural sources and anthropogenic activities. [52] In the previous paragraph we have seen that these aerosols play a central role not only in air pollution but also in climate evolution, due to their impact on light scattering and their potential to act as cloud condensation (CCN) or ice nuclei (IN). Moreover they affect the number, the concentration, and the size of cloud droplets and induce changes their lifetimes, and in their precipitation rates. Due to their potential impact on Earth's atmosphere, a thorough understanding of the structure and the phase transitions of neat and binary aqueous aerosols under atmospheric conditions is strongly needed, especially when they are in contact with water molecules**.**

3.4 The development of computer simulations as tools to model solid/fluid interface

Modeling any of the above mentioned phenomena related to solid/fluid interfaces requires the accurate treatment of the interactions between the solid and the fluid phase. The history of computer simulations of solid/fluid interfaces originates in the very early years of appearance of computer simulations in physical sciences, and the development in this field has been going on ever since. In this early age of simulations, due to the limited computational and storage capacity, the atomistic treatment both of the phases in MD or MC simulations would have been extremely demanding. Thus, development in this field followed two main directions: *i*, the use of enhanced potential models to describe the solid and/or the fluid phase; and *ii,* proposing alternative methods capable of modeling interface related phenomena besides Monte Carlo and molecular dynamics.

In the first studies the solid interface was represented by a rigid non-interacting wall. Henderson and van Swol[53], for instance performed a series of simulations in which the fluid phase was described by either hard sphere or square-well potentials whereas the wall was treated as a rigid body. Although considered as pioneering work at that time, their studies were not able to describe such interfacial phenomena as wetting or adsorption. The simplest setup capable of describing such processes uses square-well or hard-sphere potentials for both the wall and the fluid phase. Another work of Henderson and van Swol showed that these potentials performed sufficiently well in simulating wetting transitions.[54] The same question was successfully addressed by Sikkenk et. al. who studied the interaction of a Lennard-Jones fluid against a Lennard-Jones type of wall by molecular dynamics simulations.[55] The surface tension and contact angle results obtained for this model system were already surprisingly accurate for the time, however the increasing need to study more realistic systems encouraged the spread of atomistic models. Lennard-Jones type of fluids were soon replaced by molecular fluids, for instance explicit models of water. Heinzinger and Spohr, for example, reported a study about the interaction of an aqueous Li^+ solution, aimed at describing its interactions with a Lennard-Jones type of wall, where the water molecules were modeled by the ST2 water potential.[56] Metal walls were also investigated extensively already in the 1980s, which obviously required the atomistic treatment of the solid phase.[57]

Concerning the second, methodological direction of development in this field, it has to be emphasized that historically integral equation methods represented the state of the art technique to simulate interactions between fluids and hard walls by using the Ornstein-Zernike equations.[58] However well they worked for describing gas/solid interactions in general, they failed to reproduce the wetting of the solid surface by a liquid properly.[59] The second technique to mention is density functional theory, which has been successfully applied to reconstruct crystal/fluid interactions and the subsequent melting of the crystalline surface. [60]

Despite of the variety of techniques and models in early simulations, atomistic-scale Monte Carlo and molecular dynamics simulations have become doubtlessly the most popular among methods to simulate solid/fluid interactions, due to the wide range of their applicability for various problems, their accuracy and their relatively simple theoretical background. Indeed, the increased computational capacity of today's computers allows us to use highly developed equilibrium or even non-equilibrium simulations to model interfacial phenomena on the atomistic scale. Equilibrium molecular dynamics simulations are usually applied to investigate the dynamics of adsorption and desorption processes on various types of solid surfaces, for instance graphite, metals or silica surfaces[61,62,63,64,65], on porous materials such as zeolites[66,67] frameworks (MOFs) which are promising new type of molecular sieves.[68,69] Grand canonical Monte Carlo methods, on the other hand, have replaced 2D simulation techniques in the beginning of the 1990s in modelling adsorption and have become one of the most widely used techniques to calculate adsorption isotherms on various atomistic solid surfaces. Recently attempts have been made to adapt the GCMC method for modeling competitive adsorption which is of equally great interest from both industrial and environmental point of view.

3.5 The interaction of volatile organic hydrocarbons and water under tropospheric conditions – an overview on the literature

We have already seen that VOCs are indeed among the key factors in heterogeneous reactions occurring in the atmosphere, and as such the detailed description of their interaction with ice is of exceptional importance, however, until the end of the 20th century the molecular level description of the corresponding mechanisms represented a largely unexplored field. During the last decade, a number of experimental[70,71,72,73,74,75,76,77,78,79] and theoretical[80,81,82,83,84,85,86,87,88,89,90,91,92,93] studies have been devoted to the characterization of the interactions between small organic molecules and ice. More specifically, coated-wall flow tube and Knudsen cell experiments have been performed to characterize the uptake of different volatile organic compounds (VOCs), including aldehydes and alcohols, carboxylic acids and ketones by ice. These studies have shown that VOCs are reversibly adsorbed on ice, having adsorption enthalpies ranging between -70 kJ/mol and –50 kJ/mol, with the exception of formaldehyde for which it was not possible to accurately determine the adsorption enthalpy which is thus supposed to be quite small.

Experiments have been complemented by theoretical calculations performed at a molecular level to deal with such fundamental questions as the energetics of the interaction between VOCs and ice, their preferred location and orientation at the surface, and, the possibility of the emergence of competition between hydrogen-bonds with ice and lateral ones formed between adsorbed species. *Ab initio* calculations have been devoted to the characterization of the adsorption properties of, among others, acetone and formic acid on ice.[81,84] However, these quantum studies focused on the determination of adsorption geometries and energies at 0 K and, as a consequence, the transferability of the corresponding results to tropospheric temperatures has remained questionable. Classical MD and GCMC methods, on the other hand, may allow a more realistic modelling of the VOC-ice interactions provided that the classical potential model on which they are based is sufficiently accurate. MD simulations have thus been used to characterize the adsorption and in certain cases diffusion behavior of acetic acid[83], acetone[89,91], formaldehyde[80,85], methanol, and ethanol on ice, the adsorption of phenanthrene on snow[94], the diffusion of formaldehyde in bulk ice[85]. On the other hand, a series of GCMC studies have been performed to simulate the adsorption isotherms of methanol, formaldehyde, formic acid[86], acetone[92], and benzaldehyde[93] molecules on ice at tropospheric conditions. The simulated isotherms showed a remarkable agreement with available experimental measurements demonstrating that classical simulations are accurate and useful tools for studying interactions between VOCs and ice at tropospheric temperatures. Moreover, these simulations evidenced the influence of hydrogen bond formation on the resulting adsorption characteristics and emphasized the strong dependence of the adsorption properties on the functional chemical group of the VOC considered.

Little attention has been paid from the theoretical point of view on the other hand to the investigation of the behavior of organic molecules having more than one functional groups in connection with ice surfaces under tropospheric conditions. Even if such species are significant representatives of volatile organic compounds, being present in the atmosphere in considerable amounts, as far as we know, there is still a lack of works dealing with them.[95,96] However the molecules containing more than one organic functionality, such as oxalic acid, hydroxyacetone, glyoxal or glycolaldehyde, certainly interact with ice surfaces in a different way than simple organic species do. Dicarboxylic acids are probably the most prominent group of complex small molecules in the atmosphere. Indeed, they represent about ~30-50 % of its total organic particulate matter, and oxalic acid ($C_2H_2O_4$) comprises 37-69 % of the total amount of dicarboxylic acids. [97,98] This acid is, in particular, involved in the photochemical production of hydrogen peroxide which is responsible for the oxidation of many tropospheric species.[99] Concerning its interactions with ice, experimental studies of the adsorption and the thermally induced desorption of the mixed adsorption layer of this molecule and water by means of Fourier transformation IR spectrometry has shown that upon heating the system at any possible initial arrangement (i.e.: if oxalic acid is the lower phase, or if a homogeneously mixed adsorption layer is used, moreover also if the oxalic acid is the top layer covering initially the surface of ice) the departure towards the vapor phase of water molecules takes place prior to to that of oxalic acids.[100] This interesting experimental finding, among others, indicates the importance of an atomistic-scale characterization of the heterogeneous chemistry of this molecule at the surface of ice, which question is still not completely understood. Hydroxyacetone containing a carbonyl and a hydroxil functional group, on the other hand, can be considered as another important and relatively abundant model compound in studying the adsorption of small molecules on ice. The major source of hydroxyacetone in the atmosphere is the oxidation of methacrolein which yields 42 % of its total amount.[101,102] Once produced, this hydroxyl carbonyl compound has a potentially large atmospheric impact since it initiates the formation of HO_x radicals in the UT which, as we have seen, are known to increase the oxidizing capacity of the atmosphere and therefore to influence the ozone budget. [103]

Another significant feature of bifunctional organic species, especially dicarboxylic acids is their ability – due to their free hydroxyl and carboxylic groups – to aggregate, giving rise to the formation of organic aerosol, which may, as it has been already seen, act as cloud condensation nuclei. Thus, besides the in depth investigation of the adsorption of small molecules on ice under tropospheric conditions, another prominent question is the modeling of the condensation of these clouds, whose characteristics vary greatly with the altitude at which they are formed and situated. However, while the potential of organic aerosols to act as CCN for water clouds is well-established, little is known about their influence on icy clouds in the upper troposphere. Due to their potential impact on Earth's atmosphere, a thorough understanding of the phase transitions of aerosols under atmospheric conditions is strongly needed, especially when they are in contact with water molecules. Experimental studies focusing on the phase transition of such aerosols and their binary mixtures with water have been carried out by Braban et al.[124] Their investigations addressed two main phase transitions, namely deliquescence, which is the uptake of water by the dry aerosol particle, and efflorescence, the opposite process, i.e., the loss of water from mixtures to form a solid phase. According to their measurement, oxalic acid aerosols proved to be particularly difficult to be examined by experimental techniques. Another, very recent measurement performed by Schill and Tolbert[120] aimed at characterizing the relation between the hydrophylicity of the organic compound, described as the O:C ratio and the cloud condensation potency of its aerosol phase has, on the other hand, shed light on the fact that cloud condensation potency increases as a linear function of the O:C ratio. (The above mentioned two experiments are discussed in more and cited in Chapter 3.6.3 in comparison with the results of our simulations)

3.6 Results of modelling solid surfaces

3.6.1 GCMC simulation of the adsorption of acetaldehyde on ice [1]

3.6.1.1 Introduction

This work comprises of grand canonical Monte Carlo simulations of the adsorption acetaldehyde on ice particles under conditions which are characteristic of the troposphere.

A growing number of experimental and theoretical studies have been recently devoted to the characterization of the interactions between aldehydes of different carbon chain length and ice. Acetaldehyde is a relatively abundant representative of this group of molecules in the UT (between 30 and 100 pptv) and its atmospheric fate is of great interest, thus its uptake on ice has been recently re-investigated at tropospheric temperatures, using coated wall flow tube experiments between 203 and 253 K.[104] These studies revealed that the adsorption of acetaldehyde on ice is totally reversible, with measured values of the adsorption enthalpy falling between 41.6 ± 2.3 kJ/mol (at 223 K) and -36.4 ± 2.0 kJ/mol (at 203 K).

Our GCMC simulations are aimed at investigating the applicability of the Langmuir model for the adsorption of this molecule on ice under tropospheric conditions. The question of the structure of the adsorbed layer together with the orientation of the individual acetaldehyde molecules within the layer are also addressed**.**

3.6.1.2 Computational details

Adsorption of acetaldehyde on I_h ice has been modeled by grand canonical Monte Carlo simulations at 200 K. The X, Y and Z edges of the rectangular basic simulation box have been set to 100.0 Å, 35.926 Å, and 38.891 Å, respectively, axis X being perpendicular to the ice surface. Standard periodic boundary conditions have been applied. 2880 water molecules, arranged in 18 molecular layers of proton-disordered I_h ice have been placed in the middle of the simulation box along the X axis. The number of the acetaldehyde molecules has been left to fluctuate by fixing their chemical potential. To determine the full adsorption isotherm a set of 20 simulations has been performed, in which the chemical potential of acetaldehyde, μ, has been increased gradually from -47.1 to -30.2 kJ/mol.

Water molecules have been described by the rigid, five-site TIP5P model.[105] Acetaldehyde parameters have been taken from the Transferable Potential for Phase Equilibria (TraPPE) force field. [106] According to this force field, the CH_3 and CH groups have been treated as united atoms. The interaction parameters of the potential models used in this study are summarized in Appendix A Table 1. All interactions have been truncated to zero beyond the molecule-based cut-off distance of 12.5 Å, and no long-range correction has been applied for the electrostatic interactions.

The simulations have been performed using the MMC open source Monte Carlo code.[107] Particle displacement and particle insertion/deletion steps followed each other in an alternating order. In a particle displacement attempt a randomly chosen molecule has been translated randomly by no more than 0.25 Å and rotated randomly around a randomly chosen space-fixed axis by no more than 15°. Water and acetaldehyde molecules have been chosen for particle displacement steps with 50%-50% probabilities. In a particle insertion/deletion step either a randomly chosen acetaldehyde molecule has been attempted to be removed from the system, or a new acetaldehyde molecule has been attempted to be added to the it. Particle insertion and deletion attempts have been made with equal probabilities, using the cavity biased scheme of Mezei, i.e., particles have only been attempted to be inserted into empty cavities of the radius of at least 2.5 Å. Suitable cavities have been searched for along a $100 \times 100 \times 100$ grid. Equilibration lasted for 10^8 Monte Carlo steps, after which, in the production stage, the number of acetaldehyde molecules has been recorded and averaged over 2×10^8 sample configurations. Finally, at selected chemical potential values (corresponding to significantly different surface coverages) 2500 sample configurations separated by 2×10^5 Monte Carlo steps have been saved for structural and energetic analysis.

3.6.1.3 Results

3.6.1.3.1 Adsorption isotherms

The adsorption isotherm obtained from our GCMC simulations is shown in Figure 3.3., from which it is clearly visible that the number of adsorbed molecules increases with the increasing chemical potential up to the point of condensation. The large slope of the increase observed at low μ values gradually decreases at higher chemical potentials and no plateau of the isotherm is observed before the point of condensation. The sudden jump in the isotherm at $\mu = -34.2$ kJ/mol corresponds to the point of condensation, where the vapor and liquid phases of acetaldehyde have the same chemical potential. Above this value the simulation box contains liquid acetaldehyde.

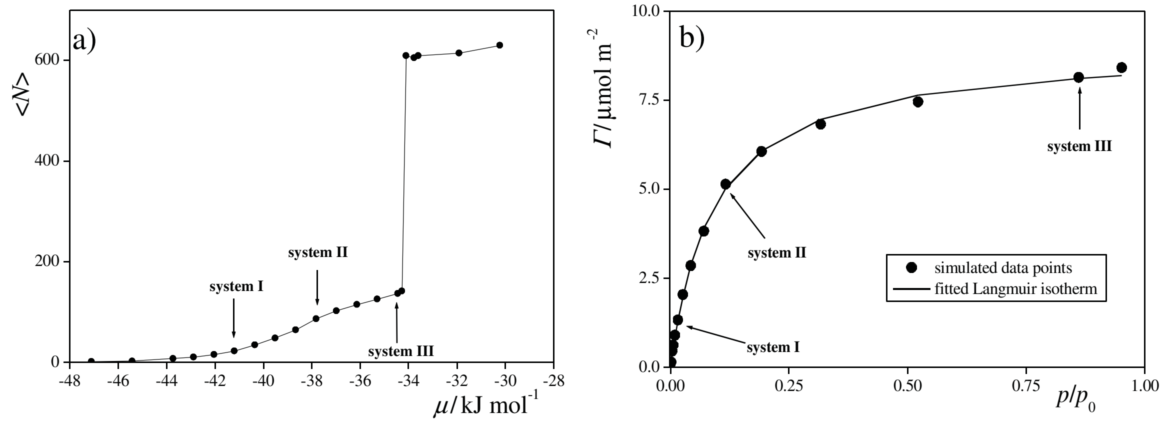

Figure 3.3 *a) Average number of acetaldehyde molecules in the basic simulation box as a function of their chemical potential. b) Adsorption isotherm of acetaldehyde on ice, obtained from our simulation (circles), together with the Langmuir fit to these data (solid line). The arrows indicate the systems used in the detailed analyzes.*

It is more convenient to look at the isotherm expressed in terms of the surface coverage as a function of relative pressure $\Gamma(p_{\mathrm{rel}})$, where $p_{\mathrm{rel}} = p/p_0$ relative pressure is calculated as the ratio of the actual pressure of the system and that of the saturated vapor (Figure 3.3.b). The values of Γ and p_{rel} can simply be obtained as

$$\Gamma = \frac{\langle N \rangle}{2YZ}, \tag{3.3}$$

and [108]

$$p_{rel} = \frac{p}{p_0} = \frac{\exp \mu}{\exp \mu_0}. \tag{3.4}$$

The factor of 2 in the denominator of Eq. 3.3 reflects the fact that, due to the periodic boundary conditions, the basic simulation box contains two ice surfaces, whereas μ_0 in Eq. 3.4 is the chemical potential value corresponding to the point of condensation. Obviously, the conversion of the $\langle N \rangle(\mu)$ isotherm to the $\Gamma(p_{\mathrm{rel}})$ form can only be done up to the point of condensation. The shape of the isotherm obtained as a result of the conversion is well described by the Langmuir formalism. The Langmuir character of the isotherm suggests that the saturated adsorption layer is monomolecular, and that lateral interactions between the adsorbed acetaldehyde molecules are do not affect the mechanism of adsorption.

3.6.1.3.2 Characterization of the Adsorption Layer

The molecular level details of the structure of the adsorption layer have been analyzed based on 2500 sampled configurations collected in systems characterized by three different chemical potential values, namely, -41.2, -37.8, and -34.4 kJ/mol, which, from now on, are referred to as systems I, II and III, respectively.

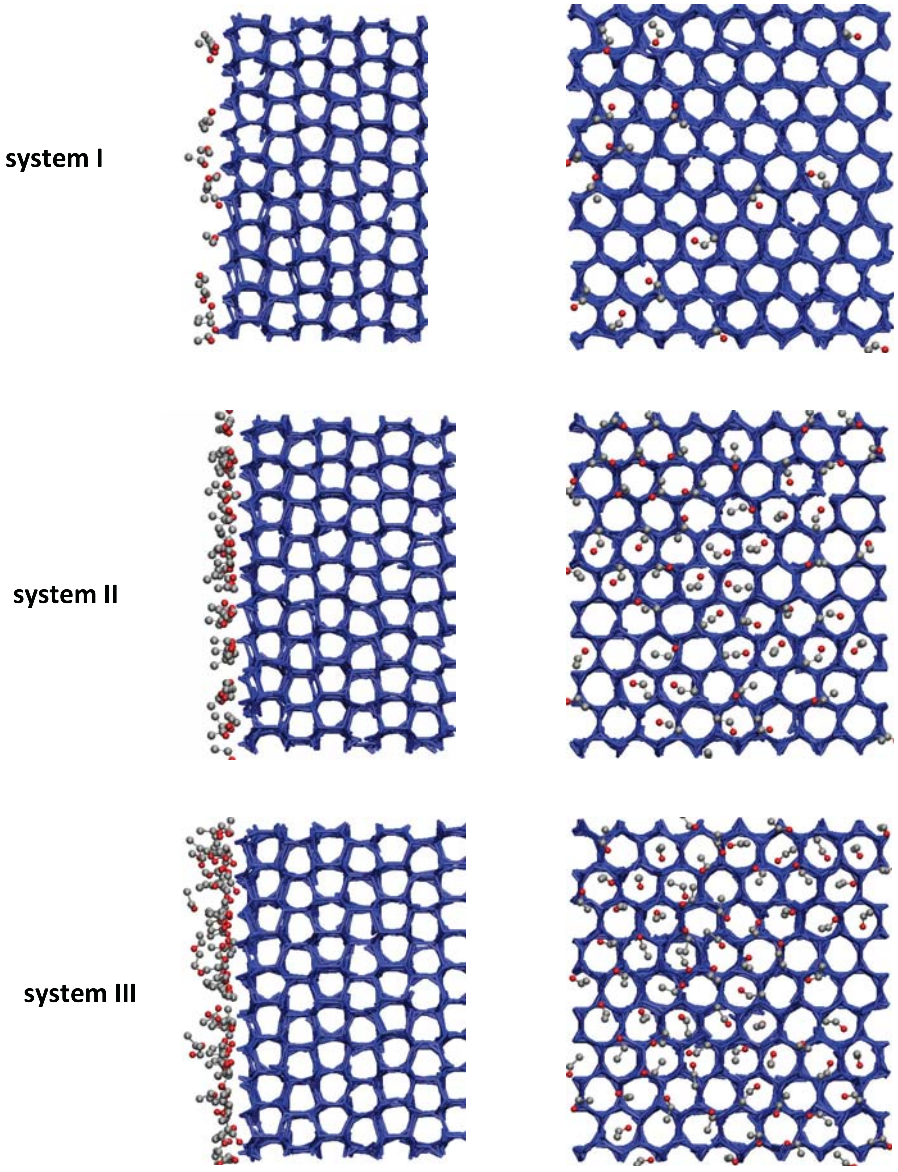

Figure 3.4 *Instantaneous equilibrium snapshot of systems I (top), II (middle) and III (bottom), as taken out from the simulations, shown both in side (left) and top views (right). Water molecules are shown by blue sticks, acetaldehyde molecules are shown by balls and sticks. The O and C atoms of the acetaldehyde molecules are shown by gray and red colors, respectively, H atoms are omitted from the figure for clarity.*

System I corresponds to the linearly rising part of the Langmuir-like isotherm, where due to low surface coverage adsorbed molecules are isolated from each other. System II represents to the part of the isotherm where it turns from a linear rise to a nearly constant section. At this μ value the adsorption layer is not yet saturated, however, most adsorption sites are already occupied, thus the adsorption of the acetaldehyde molecules is no longer independent from each other. Finally, system III is located at the nearly constant part of the $\Gamma(p_{\mathrm{rel}})$ isotherm corresponding to the saturated monolayer. Equilibrium snapshots of systems I-III are shown in Figure 3.4 both from top and side views.

Density Profiles. The density profiles of the acetaldehyde O atoms and CH_3 groups along the interface normal axis X are presented in Figure 3.5 for each of the analyzed systems. All the profiles shown are symmetrized over the two interfaces present in the basic box. All profiles have turned out to be unimodal and, apparently, the increasing coverage of acetaldehyde on the ice surface only leads to the increase of the heights of the peaks leaving their position along the interface normal axis completely unaffected. The observed unimodal character of the peaks even at the highest chemical potential values indicates, in accordance with the Langmuir-like behavior of the isotherm, that the saturated adsorption layer is still monomolecular.

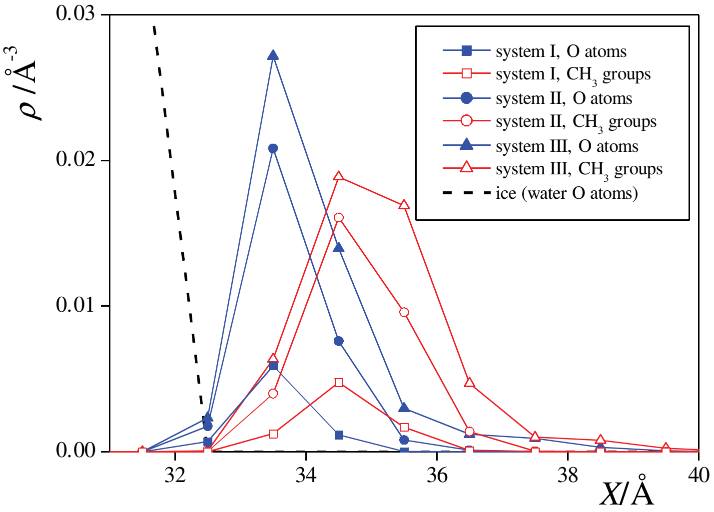

Figure 3.5 *Number density profile of the O atom (filled symbols, blue) and CH_3 group (open symbols, red) of the acetaldehyde molecules in systems I (squares), II (circles) and III (triangles), as obtained from the simulations. For reference, the outer tail of the number density profile of the water O atoms in system I is also shown (dashed line). All profiles shown are symmetrized over the two surfaces present in the basic simulation box*

The lack of the peak position shift, on the other hand, suggests that no substantial change in the orientation of the adsorbed molecules occurs upon saturation. It is also seen that the density peak of the O atoms is located about 1 Å closer to the ice surface in every case than that of the CH_3 groups, which means that the adsorbed acetaldehyde molecules prefer, on average, to point towards the ice surface by the O atom, and away from it by the CH_3 group. However, the relatively small peak-to-peak distance of the O and CH_3 density profiles being considerably smaller than the intramolecular distance of the O atom and the CH_3 group of 2.4 Å in the gas phase equilibrium geometry suggests that the majority of the adsorbed molecules are probably tilted from the surface normal axis rather than pointing straight towards the ice phase by the O atom.

Energetic Background of the Adsorption. In order to get an insight into the energetic background of the adsorption, we have calculated the distribution of the binding energy U_b of the adsorbed acetaldehyde molecules (that is the energy of their interaction with the rest of the system) in systems I-III. In addition, the U_b^w and the U_b^{lat} contributions to the total binding energy, coming from the interaction with the water molecules of the ice phase and from the lateral interaction with the other acetaldehyde molecules, respectively, have also been extracted. The $P(U_b^w)$ and $P(U_b^{lat})$ distributions obtained in systems I-III are shown in Figure 3.6.

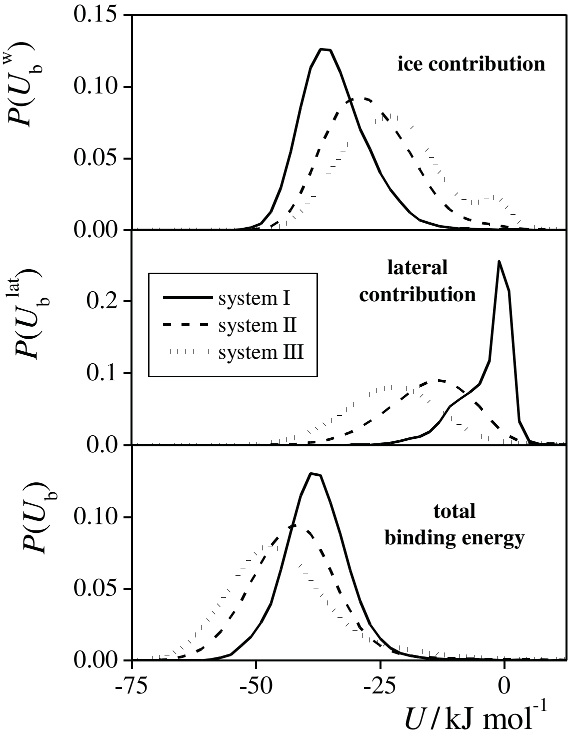

Figure 3.6 *Distribution of the binding energy of an adsorbed acetaldehyde molecule (i.e., the energy of interaction between the adsorbed molecule and the rest of the system, bottom panel), and that of its contributions coming from the interaction with the other adsorbed molecules (middle panel) and with the ice phase (top panel). Solid lines: system I, dashed lines: system II, dotted lines: system III.*

At low surface coverage the $P(U_\mathrm{b}^\mathrm{w})$ distribution has a single peak around -35 kJ/mol. Considering the fact that the energy of a hydrogen bond is roughly -20 – -25 kJ/mol, respectively, which indicates that the adsorbed acetaldehyde molecules form one hydrogen bond with the water molecules of the ice surface. The mean value of the distribution is -34.1 kJ/mol, which can serve as an estimate for the heat of adsorption at infinitely low coverage. Upon saturation, the peak of the $P(U_\mathrm{b}^\mathrm{w})$ distribution gradually shifts to higher energies, being positioned at about -29 and -23 kJ/mol in systems II and III, respectively; which indicates the gradual increase of competition between the adsorbed molecules. Despite of the presence of competitive interactions, apart from a small fraction of the adsorbed molecules contributing to the small peak of $P(U_\mathrm{b}^\mathrm{w})$ near zero in system III, the adsorbed acetaldehyde molecules form one hydrogen bond with surface waters even at high coverages.

The $P(U_\mathrm{b}^\mathrm{lat})$ distribution exhibits a large peak at zero in system I, reflecting the fact that at this low coverage the adsorbed molecules are typically well separated from each other. However, this distribution shows two clear shoulders at the negative energy side of the main peak, one at around -10 kJ/mol, and another around -20 kJ/mol. These peaks correspond to acetaldehyde molecules having one and two near neighbors, whose relative orientation has to be such that it is favored by dipolar forces (e.g., head-to-tail or antiparallel dipole-dipole alignments). In systems II and III the $P(U_\mathrm{b}^\mathrm{lat})$ the peak appears around -14 kJ/mol and -22 kJ/mol, respectively, indicating that upon saturation an increasing fraction of the adsorbed molecules has two such neighbors, and in the saturated adsorption layer this becomes the most common arrangement.

The distribution of the total binding energy, $P(U_\mathrm{b})$, is unimodal in every case, the peak position being shifted to lower energies upon saturation from about -38 kJ/mol in system I to -42 kJ/mol (system II) and -48 kJ/mol (system III). This result confirms that the increasing lateral interaction overcompensates the slight weakening of the acetaldehyde – ice interaction, occurring due to the increasing competition of the molecules upon saturation.

Orientation of the Adsorbed Molecules. The analysis of the density profiles and binding energy distributions has already led to several conclusions about the orientation of the acetaldehyde molecules in the adsorbed layer. However to investigate the orientational preferences of the acetaldehyde molecules in the adsorbed layer, their orientational map have been calculated according to the protocol described in Chapter 2.7.2.2.

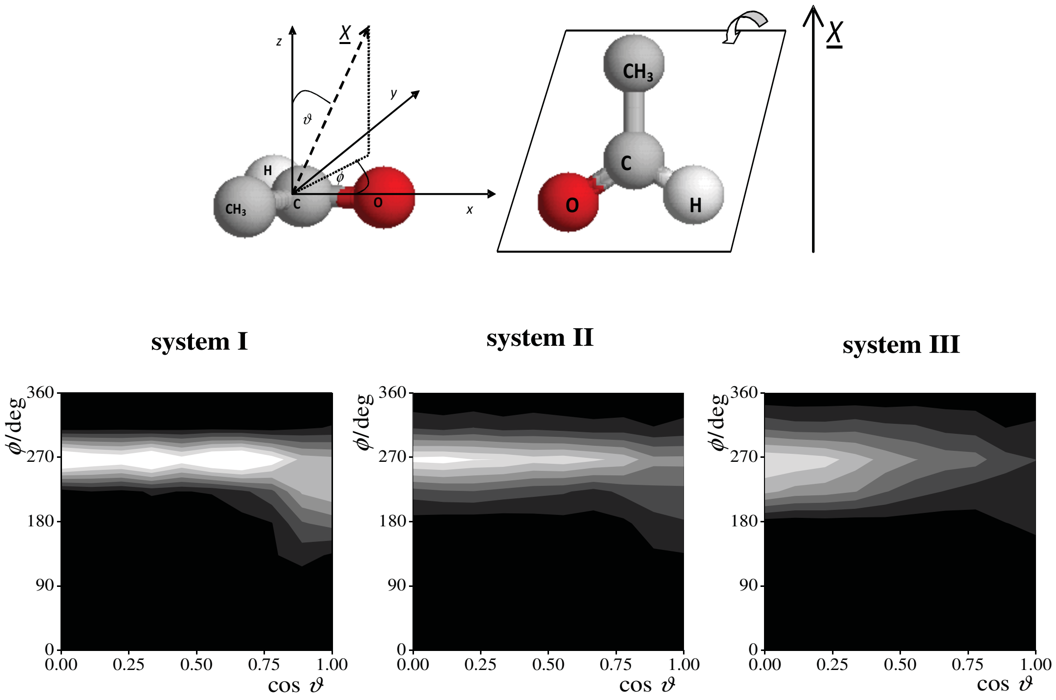

Figure 3.7 *Definition of the local Cartesian frame fixed to an acetaldehyde molecule in order to describe their surface orientation. X is the surface normal vector pointing away from the ice phase, ϑ and ϕ are its polar coordinates in this molecule-fixed local frame. (top left) Illustration of the acetaldehyde orientations corresponding to the peak region of the maps. The plane of the molecule gets increasingly tilted upon moving along the peak region from lower to higher cosϑ values. (top right) Orientational map of the adsorbed acetaldehyde molecules in systems I (left) II (middle) and III (right). Lighter colors indicate higher probabilities (bottom panels).*

In this specific case the local Cartesian frame used for orientational analysis has been defined in the following way. The origin coincides with the C atom of the aldehyde group, axis x points along the C=O double bond from the C to the O atom, axis z is perpendicular to the plane formed by the CH_3 group and C=O bond of the molecule, and axis y, being perpendicular to the above two axes, is oriented in such a way that the y coordinate of the CH_3 group is negative. The definition of this local frame along with that of the polar angles ϑ and ϕ is illustrated in Figure 3.7 together with $P(\cos\vartheta,\phi)$ orientational maps of the adsorbed acetaldehyde molecules obtained for systems I-III.

The preferred orientations of the acetaldehyde molecules seem to depend only slightly on the surface coverage. The distribution obtained for system I exhibits a rather elongated peak around the ϕ value of 250°, extending from $\cos\vartheta = 0$ to about $\cos\vartheta = 0.6$, corresponding to the ϑ range of about $50^o \leq \vartheta \leq 90^o$. According to this definition of the local Cartesian frame, ϑ is simply the angle formed by the plane of the adsorbed molecule with the plane of the ice surface, thus this finding suggests that acetaldehyde molecules adopt orientations ranging from tilted by about 50^o to perpendicular relative to the surface plane. The observed preferences of the acetaldehyde molecule is also illustrated in Fig. 3.7. Contrary to ϑ, angle ϕ is very strongly restrained to a narrow interval around 250° for acetaldehyde molecules in the adsorption layer. This finding indicates that the CH_3 group is located as far from the ice surface as possible within the constraint of the tilt angle of the molecular plane, ϑ. In the particular case of $\vartheta = 90^{\circ}$ (at $\cos\vartheta = 0$) this means that the C-CH_3 bond points straight away from the ice surface. It is also seen that upon saturation of the adsorption layer the peak of the $P(\cos\vartheta,\phi)$ orientational map becomes less elongated along the $\cos\vartheta$ axis, extending to $\cos\vartheta$ values of about 0.4 and 0.2 in systems II and III, respectively. The shrinkage of the $\cos\vartheta$ range suggests that as the adsorption layer gets increasingly crowded the adsorbed molecules adopt, on average, less tilted orientations, and in the saturated monolayer the perpendicular orientation becomes clearly the preferred one. This is in accordance with the fact that, due to their increasing competition, the adsorbed molecules should occupy, on average, smaller surface area upon saturation.

To understand the physical background of the observed orientational preferences it should be noted that surface water molecules of I_h ice have four preferred orientations. In one of these orientations an O-H bond stays perpendicular to the surface pointing by its H atom to the vapor phase, whilst in other preferred orientations at least one of the O-H bonds points flatly to the vapor phase, declining from the surface plane by about 20°. As is illustrated in Figure 3.8, the adsorbed

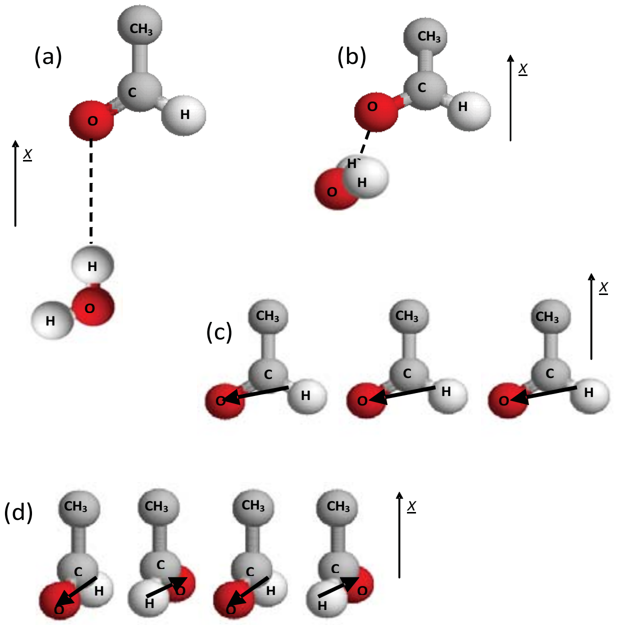

Figure 3.8 *Possible hydrogen bonds between a water molecule located at the ice surface and an adsorbed acetaldehyde molecule aligned in one of its preferred orientations: a) acetaldehyde molecule aligned perpendicular to the ice surface, b) acetaldehyde tilted relative to the ice surface. Possible alignments of the neighboring acetaldehyde molecules are also illustrated: c) acetaldehyde molecules in head-to-tail type dipole arrangement, d) acetaldehyde molecules in antiparallel-like dipole arrangement.* $\underline{X}$ *is the surface normal vector pointing away from the ice phase.*

acetaldehyde molecules that align perpendicular to the surface can accept a hydrogen bond from the former, while those being tilted by 50° relative to the ice surface can accept one from the latter type of water molecule. Finally, considering the observed orientational preferences, the favored dipole-dipole arrangement of two neighboring acetaldehyde molecules, seen from the lateral binding energy distributions, can be realized either by the two molecules being located behind each other, pointing by their C=O bond to the same direction (head-to-tail-like arrangement), or by them being located next to each other, pointing by their C=O bonds to the opposite directions (antiparallel-like arrangement). Both of these possible near neighbor arrangements of the adsorbed acetaldehyde molecules are also illustrated in Figure 3.8.

3.6.1.4 Comparison of the simulation results with experimental studies

FTIR spectra of ice exposed to increasing amount of acetaldehyde together with to the spectrum of solid acetaldehyde has been analyzed in comparison with our results concerning the energetics of adsorption and orientation of acetaldehyde molecules at the surface of ice. The shift of stretching mode of dangling OH groups of water is a clear indication of the formation of one hydrogen bond between the dangling hydrogen of water and acetaldehyde, which finding is in accordance with our results concerning energy distributions. The analysis of the spectrum of acetaldehyde on the other hand has led to the conclusion (by examining the νC=O band) that acetaldehyde is attached to the surface by its carbonyl group, which again is in agreement the results of simulations. Further analysis of the acetaldehyde spectrum on the other hand has evidenced the formation of a solid layer of acetaldehyde molecules similar to the separate solid phase. However, whereas in the separatele solid individual molecules are found to connected by C-H – O hydrogen bonds, the red shift of the corresponding peak of the ice-acetaldehyde spectrum suggests that at ice surface lateral interactions are restricted to dipole-dipole and dispersion forces, being in accordance with the fact that our adsorption isotherm can be well fitted by a Langmuir-isotherm. The adsorption enthalpy (ΔH_{ads}) estimated from the IR spectrum has also been found to agree with our estimation based on the energy distributions of system I.[212]

It can be concluded that simulation of the acetaldehyde/ice system yielded results concerning both the mechanism and the energetics of adsorption, and the orientation of the molecules in the adsorbed layer which are in excellent agreement with the corresponding FTIR measurements, which are accurate and widespread methods to study adsorption on solid surfaces.

3.6.2 MD simulations of the adsorption of oxalic acid and hydroxyacetone on ice [2,3]

3.6.2.1 Introduction

This study is aimed at describing the structural and dynamic behavior of the adsorbed layer of more complex organic compounds, such as oxalic acid and hydroxyacetone at the surface of ice under conditions that mimic the upper troposphere, by simulations. Due to the fact that this field is, to best of our knowledge, relatively unexplored, besides analyzing simulation results special attention has been paid to exploring the range of validity and limitations of the potential models by comparing our findings with experimental results.

We have performed molecular dynamics simulations to get insight into the atomistic scale structural and dynamic properties of the adsorption of oxalic acid on ice at different temperatures and for different amount of adsorbed molecules. In particular, we have characterized the energy distribution and surface orientation of the adsorbed oxalic acid molecules. We have also focused on the possible conformational changes of the oxalic acid molecules upon adsorption, and we examined the possibility of lateral aggregation. These analyses have been aimed primarily at proving the applicability of computer simulations to study the interactions of bifunctional organic molecules with ice under tropospheric conditions, by attempting to use our results to explain the experimental finding about the anomaly of thermal desoprtion of water molecules from under the oxalic acid adsorption layer. Upon finding that MD simulations are able to explain such elaborate interactions, we have performed simulations of the adsorption of hydroxyacetone on ice.

3.6.2.2 Computational details

Molecular dynamics simulations of oxalic acid and hydroxyacetone molecules deposited on ice at infinitely low and at finite coverages have been performed using the GROMACS 3.3.2. program package. [109] Calculations have been carried out on the canonical (*N,V,T*) ensemble at three different temperature values, namely at 200 K, 220 K and 240 K. These values are proven to correspond to conditions at different heights of the troposphere. The temperature of the systems has been controlled by means of the weak coupling algorithm of Berendsen *et. al.* [110]

Water molecules constituting the ice slab have been fully rigid while in case of oxalic acid and hydroxyacetone bond angle and torsional flexibility has been allowed. The geometry of water molecules has been kept unchanged using the SETTLE [111] algorithm, whereas chemical bonds of oxalic acid and hydroxyacetone have been maintained at constant value by means of the LINCS[112] algorithm. The potential energy of the systems investigated have been calculated as the sum of atom-atom pairwise interaction energies between the interacting species consisting of dispersion and Coulombic contributions. The Lennard – Jones σ, and ε parameters of the corresponding atom pairs have been obtained from the σ and ε values of the individual molecules according to the Lorentz – Berthelot rule.[14] The Lennard-Jones interactions have been neglected for atom pairs positioned at distances greater than an interaction site-based cutoff of R_c=9 Å, while the long-range part of electrostatic interactions has been accounted for by the Particle Mesh Ewald (PME) method.[16]

In the case of the oxalic acid/ice systems two interaction potential models were used for water molecules, namely the TIP5P[105] and the TIP4P/2005 [113], for comparison. The I_h ice slab used in the simulations had the same dimensions as the one used for modeling the adsorption of acetaldehyde (chapter 3.6.1), that is it consisted of 18 layers built up of 2880 water molecules, with interfacial plane being the basal surface. Based on the preliminary results obtained for oxalic acid-water interaction and knowing that TIP5P reproduces the melting point of hexagonal ice sufficiently well, hydroxyacetone/ice systems have only been simulated using a TIP5P ice slab. Partial charges and the initial geometry of the oxalic acid molecules have been taken from *ab initio* calculations [114] while the Lennard-Jones σ and ε parameters were obtained form the OPLS [115] force field. On the other hand, hydroxyacetone molecules have been modeled simply by the OPLS potential[115], in the lack of an existing well-established model to describe these molecules.

The choice of the initial geometries is crucial in the case of these molecules which are both characterized by an internal torsional degree of freedom around their C-C single bond. In case of oxalic acid choosing the initial geometry has been a straight forward task. *Ab initio* calculations [116,117,118] have shown that in vacuum an individual oxalic acid molecule can have six different conformers stabilized by intramolecular H-bonds whose relative stability ranges between a few to tens of kJ/mol. The most stable among these corresponds to the formation of two five-membered rings involving the C=O groups and their vicinal OH groups (see Fig. 3.9). At tropospheric temperature, the energy of thermal motion (k_BT) is considerably lower than the potential energy barrier corresponding to transforming this conformer into any of the others. This allowed us to use uniquely the most stable conformer to describe the geometry of this molecule in the initial configurations of our simulations. The case of hydroxyacetone has turned out to be more complicated than what has been seen for oxalic acid. To the best of our knowledge no outstandingly stable conformation hydroxyacetone has been reported in the literature, moreover *ab initio* studies [119] have shown that about sixteen rotamers of this molecule characterised by roughly the same stability exist. In the lack of stable geometry we have decided to choose an *all trans* conformer as an initial geometry. The (initial) molecular geometries of the oxalic acid molecule are given in Fig. 3.9, whereas potential parameters of water, oxalic acid and hydroxyacetone are listed in Table 1 of Appendix A.

Figure 3.9 *Initial geometry of the oxalic acid (a) as modeled in the present MD simulations. Example of the other stable geometry of oxalic acid (b) as taken from ab initio calculations of Mohajeri and Shakerin [!118]*

All simulations have been performed as follows. The systems were created by placing a number of oxalic acid or hydroxyacetone molecules near each of the two pre-equilibrated ice surfaces in the simulation box. At infinite coverage this number has been one, while at finite coverage 52, corresponding roughly to a monolayer, has been placed near the surface. These systems have been equilibrated for 5 ns with a timestep of 1 fs, on the canonical ensemble which has been followed by a production run of 5 ns under the same conditions during which 5000 configurations separated by a 10 ps long trajectory have been saved for analysis.

3.6.2.3 Results concerning oxalic acid

3.6.2.3.1 Adsorbed geometries

Intramolecular H-bonds The most stable gas phase conformations of oxalic acid are stabilized by either five- or four-member ring structures (see Fig. 3.9), created by intramolecular hydrogen bonding of the hydroxil H (H_{OH}) atom to one of the carbonyl O atoms (O_{CO}). Thus forming these bonds requires a relatively short O_{CO}-H_{OH} distance. According to *ab initio* calculations of Mohajeri et. al.[118] the equilibrium value of this distance for vicinal O_{CO}-H_{OH} pairs in the five-member rings ($dO...H = 2.1$ Å) is found to be slightly shorter than for geminal pairs in the corresponding four-member ring structure ($dO...H = 2.3$ Å), as shown in Fig. 3.9 a and b. The distribution of these distances have been calculated for the simulated trajectories to find that they increase by on average 1.3 Å when an oxalic acid molecule is adsorbed at the surface of ice, independently from the choice of water model and of temperature. The average distances have been approximated by the peak position of the Gaussians fitted to the corresponding distribution functions. From this increase, it may be anticipated that in the vicinity of other H-bonding partners (such as a water molecule of the ice surface or another carboxylic acid) the geometry of the oxalic acid molecules undergo conformational changes (e.g., rotation of the OH groups) which increase the possibility of forming intermolecular hydrogen bonds even at the expense of loosing the aforementioned prominently stable ring structures and changing the O=C-C=O dihedral angle.

The distribution of the C-C torsional angle To further investigate the geometry of the adsorbed oxalic acid molecules we have calculated the distribution of the O=C-C=O dihedral angle at the ice surface. The obtained distributions are shown in Figure 3.10 together with examples of the

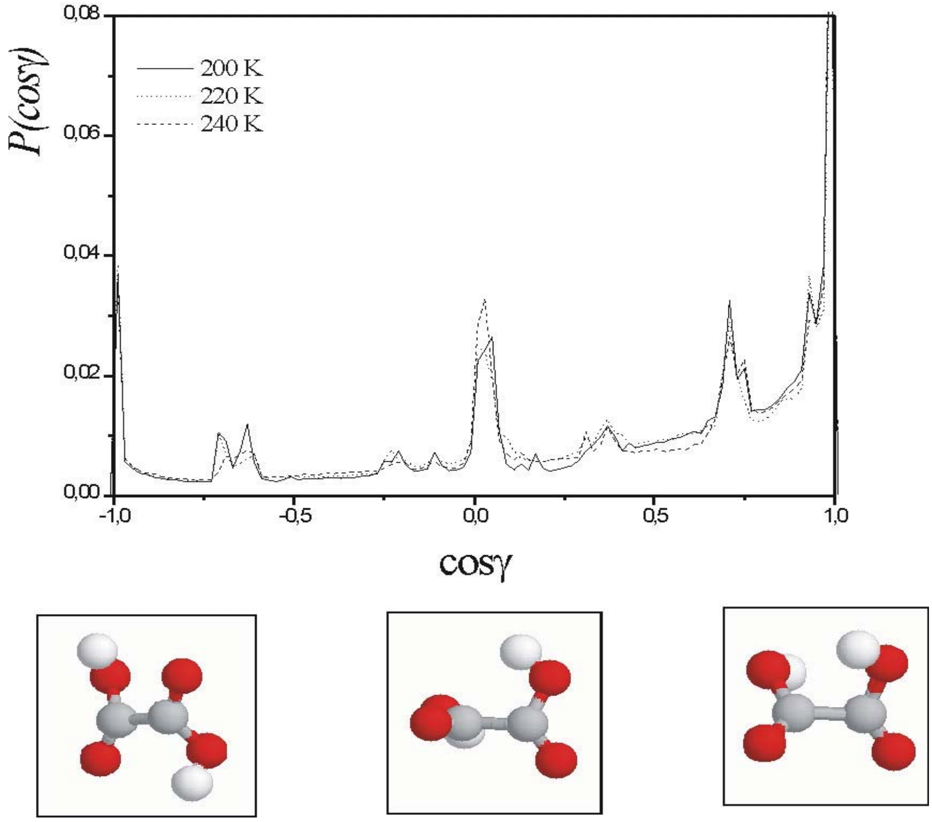

Figure 3.10 *Dihedral angle distribution around the C-C- bond for the oxalic acid molecules adsorbed at the surface of hexagonal ice at three different temperatures and finite coverage. We also illustrate some oxalic acid geometries found in snapshots of the simulations, below the corresponding torsional angle values.*

three preferred torsional states found in the adsorption layer. It is clearly visible that irrespective of the simulation temperature, the cosine distribution of the O=C-C=O dihedral angle shows three major peaks. The first one at $\cos\gamma \sim 1$ corresponds to the "*cis*" conformation, in which the torsion angle is close to 0°, the second one at $\cos\gamma \sim 0$ describes a conformation in which the O=C-C=O dihedral angle is roughly 90°, i.e., when, the two carboxyl groups are perpendicular to each other, while the third one at $\cos\gamma \sim -1$ corresponds to the "*trans*" conformation of the two C=O bonds. The presence of these peaks in the dihedral angle distribution indicates that different geometries (mainly "*cis*" and "*trans*" structures) appear in the presence of lateral interactions either with neighboring oxalic acid or with water molecules. It should be noted here that the dihedral angle distributions given in Fig. 3.10 do not contain information on the orientation of the hydroxyl group with respect to the C—C bond of the oxalic acid molecule. However, looking at the equilibrium snapshots at various temperatures reveals that OH groups can point either inwards or out of the plane of the corresponding COO- group, as illustrated by the examples in Fig. 3.10. These rotations of the OH groups facilitate the formation of hydrogen bonds with neighboring water and oxalic acid molecules. Indeed, by considering that the stable ring structures are stabilized by a maximum of two H-bonds for a single molecule in the gas phase, the driving force of such conformational changes in the adsorbed phase might be, in the vicinity of other H-bonding partners, the opportunity of further decreasing the energy of the entire system by forming more than two intermolecular H-bonds, even at the expense of the increase of the conformational energy of the individual molecule. However, it should be mentioned that the flexibility of the C-OH bonds involved in these OH group rotations is certainly very sensitive to the internal potential used in the simulations. Nevertheless, changes in the internal conformation of oxalic acid molecules upon adsorption on ice at finite coverages are clearly evidenced.

Energy distributions In order to get a deeper insight into the energetic changes that occur during and as a result of the adsorption process, as well as to shed light on the background of the observed conformational changes, we have calculated the distribution of the binding energy of an oxalic acid molecule with the other oxalic acids (U_b^l) in the finite concentration range as well as that with ice phase (U_b^w) both at finite and at infinitely low coverage for all of simulated temperatures. Figure 3.11 a shows the oxalic acid-water (U_b^w) binding energy distribution for infinitely low surface coverage, while figure 3.11 b shows the oxalic acid-water (U_b^w) and oxalic acid-oxalic acid (U_b^l) binding energy distributions obtained for systems characterized by finite surface coverage.

Looking at the U_b^w curve we can conclude that the binding energy distribution of oxalic acid and water molecules in the infinitely low coverage case has a peak between -160 and -150 kJ mol^{-1}. Only a very slight shift towards more negative energies can be observed in the position of the peak for the higher temperatures. Assuming that the average energy of a single hydrogen bond is roughly -25 kJ mol^{-1}, the position of these peaks indicate that in the limiting case of infinitely low surface coverage the adsorbed oxalic acid molecule can form as much as six hydrogen bonds with the surrounding water molecules. At finite surface coverage the system shows a much more complex behavior and a stronger temperature dependence. As is seen from figure 3.11.b, at lower temperatures the P(U_b^w) curve exhibits a peak around -50 kJ mol^{-1}, which corresponds to the formation of two H-bonds with water molecules. However, when increasing the temperature this peak is shifted to about -25 kJ mol^{-1}, suggesting that at higher temperatures the oxalic acid molecules tend, on average, to form only one hydrogen bond with the ice surface.

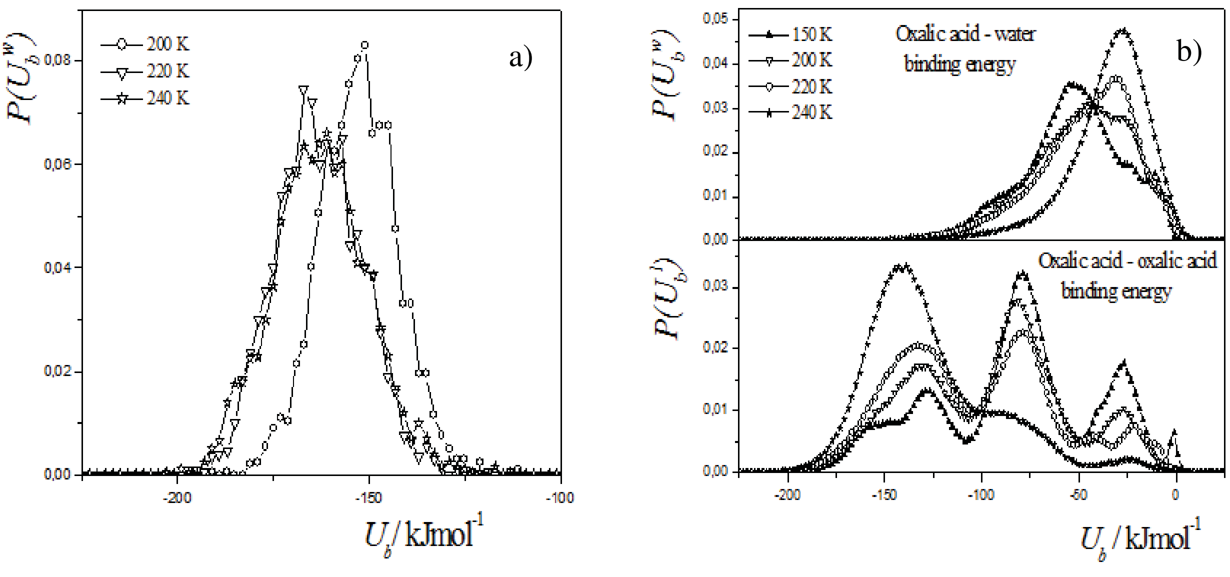

Figure 3.11 *Energy distributions of oxalic acid molecules adsorbed at the ice surface for different temperatures (a) at infinitely low surface coverage and (b) finite surface coverage.*

Looking at the temperature dependence of the *P*(U_b^l) distributions additional information can be obtained about the intermolecular interactions in the adsorption layer. At the lowest temperature three well distinguished peaks are visible at -25 kJmol^{-1}, -75 kJ mol^{-1}, -125 kJ mol^{-1}, corresponding to the formation of one, three and five hydrogen bonds with oxalic acid molecules, respectively. (Note that this latter peak also exhibits a shoulder extending down to -150 kJ mol^{-1}, indicating that some oxalic acid molecules are even tied to their neighbours by six H-bonds). At the lowest temperature the intensity of the first and the second peak (i.e., at -25 kJ mol^{-1} and -75 kJ mol^{-1}) is considerably higher than that of the third. With the increasing temperature, however, the intensity of these peaks decreases while that of the third one (at -125 kJ mol^{-1}) increases significantly. This latter peak also broadens and shifts to lower energy values, indicating a strengthening of the lateral interactions between oxalic acid molecules as the temperature is increased.

These findings suggest that upon increasing the temperature the oxalic acid–oxalic acid interactions become more favorable. In other words, at higher temperatures the oxalic acid molecules tend to be connected to like partners rather than to water molecules. This effect might be similar to the phenomenon of temperature induced demixing, which is observable in mixtures of hydrogen bonding liquids whose phase diagrams exhibit a closed-loop behavior, and which can be related to the effect of orientational entropy changes of the system. From a more practical point of view, this change in the interaction profiles may be due to the clustering of the adsorbed oxalic acid molecules at the ice surface.

3.6.2.3.2 Surface aggregation and thermal desorption

Surface aggregation The problem whether at finite surface coverages the adsorbed molecules are distributed more or less uniformly, forming a stable monolayer at the surface of ice or tend to aggregate and leave other parts of the surface unoccupied is of fundamental interest in the molecular level understanding of experimental results claiming the temperature induced departure of water molecules through the oxalic acid adsorption layer.[100] In spite of the interest in the self-association behavior of adsorbates at the ice surface, due to the lack of sensitive experimental techniques little is known about the degree of self-association of these molecules. In this study we used the technique described in chapter 2.7, aimed at detecting surface aggregation by means of 2D Voronoi analysis. The obtained VP area distributions of oxalic acid molecules, disregarding waters are shown in Figure 3.12. Oxalic acids were represented in this analysis by the midpoint of their C–C bond. Due to the fact that oxalic acid molecules are the major component of the system, the VP area distributions are close to the Gaussian shape, having only a slight exponentially decaying tail, which, becomes more pronounced with increasing temperature. The exponential decay of these tails, which is visible as a linearly decaying part if the $P(A)$ distribution is represented on a logarithmic scale (inset of Fig 3.12), is a clear proof of temperature-induced self-aggregation.

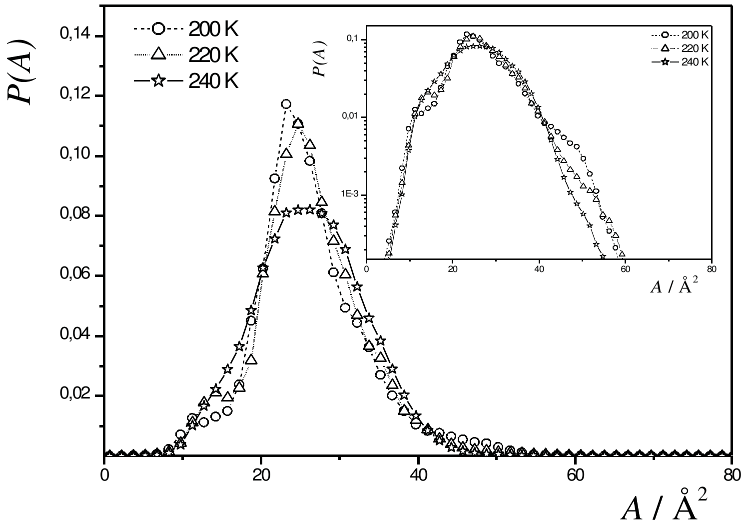

Figure 3.12 *Voronoi Polygon area distribution P(A) issued from the Voronoi analysis of the oxalic acid layer adsorbed on ice at finite surface coverage. The inset shows the same curve on a logarithm scale.*

The position of the peak in the *P*(*A*) distribution shows the typical VP area of a molecule in a lateral self-aggregate. In our systems this value has turned out to be about 22 Å^2 at 200 K, and has been found to increase with the increasing temperature up to 27 Å^2 at 240 K. On the other hand, the VP area distribution extends to about 55-60 Å^2 at every simulation temperature. These results evidence temperature induced aggregation and the consequent increase of uncovered areas between the aggregates at higher temperatures compared to what has been observed at low temperatures. Experimental evidence implies that it is water that starts leaving the surface when the temperature is increased. The fact that oxalic acid molecules tend to form aggregates on the ice surface, thus leaving small ducts for waters through which they may leave the surface without breaking the stable structure of the adsorption layer might be closely related to the aforementioned experimental fact.

Thermal desorption The easiest and perhaps the most plausible way to examine the thermally induced changes of the adsorption layer, such as desorption of water or mixing of the two phases is to analyze the distribution of the different molecules along the interface normal axis *X*. In order to address this question, we have calculated the number density profiles of the water and oxalic acid molecules along the interface normal axis *X*. Figure 3.13 shows the obtained density profiles of the simulated systems at different temperatures.

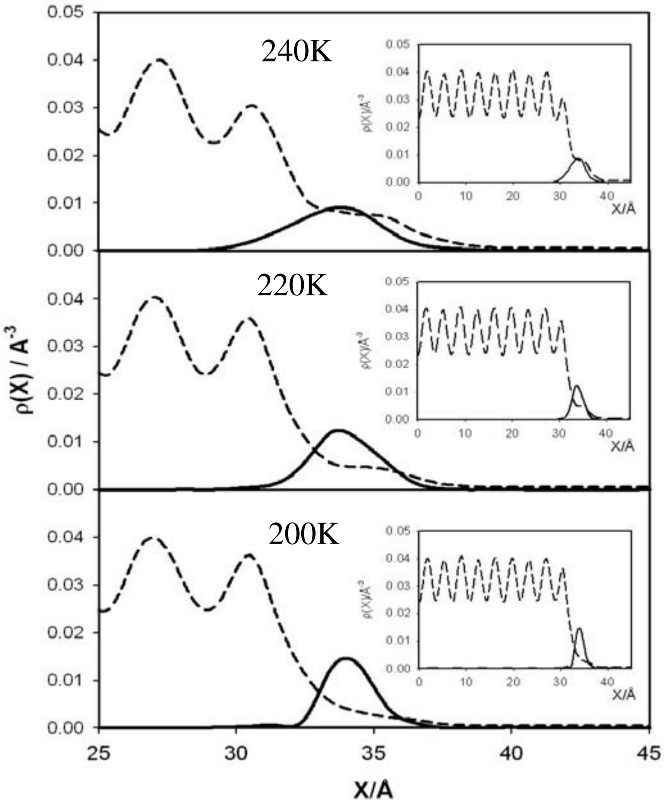

Figure 3.13 *Number density profile (solid line) of the adsorbed oxalic acid molecules at different temperatures and finite coverage corresponding to roughly one oxalic acid monolayer at the surface of ice. The number density profile of the surface water molecules is also indicated (dash-dotted line). The insets show the number density profiles for the whole system taking into account that all the profiles shown are averaged over the two surfaces that are present in the basic simulation box.*

The position of the water molecules (dashed lines) are represented by their O atoms, while oxalic acid molecules (solid lines) by one of their C atoms. The main panels of Figure 3.13 show the density distributions at the three simulated temperatures, enlarged in such a way that the adsorption layer is well observable, while on the insets the density profile of the entire system along the interface normal axis *X* can be seen. The insets show that structure of the bulk ice is well preserved during the simulations at each temperature, thus, excluding melting of the ice phase even at the highest temperature. Density profiles of oxalic acid molecules show that the adsorption layer is characterized by a single peak close to the ice surface (at about 33-34 Å), at every simulated temperature. This suggests that within the simulated temperature range significant desorption of the oxalic acid molecules does not take place. Nevertheless, a slight but pronounced broadening of the adsorption layer can be observed at higher temperatures. At 200 K (bottom panel) the width of the density peak is about 2 Å, at 220 K (middle panel) it is roughly 3 Å, while at 240 K (top panel) it is already 4.5 Å wide. This increasing broadening cannot be fully attributed to the increasing thermal motion at higher temperatures and, since these aggregates are certainly thicker than a monomolecular layer, it implies the idea of the formation of oxalic acid aggregates already invoked on the basis of the Voronoi analysis and on the interpretation of the energy distribution functions (Figs. 3.11 and 3.12). Moreover, the increasing extent of this peak down to lower X values indicates a partial solvation of the oxalic acid molecules when the temperature is increased in the simulations. A much more significant change can be observed on the water density profiles. Thus, at 200 K the water density decreases smoothly within the region of the adsorption layer, while at 220 K a conspicuous shoulder appears at that region. This may correspond to the fact that at this temperature some water molecules penetrate already into the ducts between the oxalic acid aggregates. This feature becomes even more pronounced when the temperature is further increased, and a long tail of the water density profile, corresponding to water molecules leaving the ice surface is seen at large X values. To characterize this desorption-like process in a more quantitative way we have also calculated the average percentage of water molecules located at positions corresponding to those of the oxalic acid molecules in the adsorption layer for the three different temperatures considered. The width of the adsorption layer has been estimated by the width of the density profile of the oxalic acid molecules at each temperature. At $T = 200$ and 220 K a negligibly small number of water molecules (0.7 and 0.8 %, respectively) is found to be in the X range corresponding to the location of the oxalic acid molecules, indicating that the two phases are indeed well separated at these low temperatures. This number, however, significantly increases at $T = 240$ K (being 2.2 %, corresponding to about 30 water molecules at each surface of the ice slab), indicating that the desorption process is already started at this temperature.

3.6.2.3.3 Comparison of the simulations with experiments

We are aware of the fact that the results of the present MD simulations cannot be quantitatively compared with those obtained in experiments performed on ice systems deposited on a polycrystalline Cu surface and in a ultrahigh vacuum chamber, due to the remarkably different conditions used in the experiments.[100] However, the analyses performed here may explain what has been observed in these experiments, namely that the behavior of the oxalic acid/ice system is governed by the oxalic acid–oxalic acid interactions rather than by the interactions of the oxalic acid molecules with the ice surface. On the other hand, our results can, at least for the model system in use, explain the results of the above mentioned experiment, namely that water molecules can depart from under the adsorption layer of oxalic acid, by pointing out that the temperature-induced aggregation of the organic particles is accompanied by the formation of empty patches on the surface, through which water molecules can leave without breaking stable structure of the layer. Further in a more general way, the details of the investigations performed by using molecular dynamics simulations show that the adsorption of large organic molecules on ice is a complex phenomenon, characterized by a strong competition not only between H-bonding with ice and with neighboring partners, but also between internal and external hydrogen bond formation, leading to possible deformation of the adsorbed molecules. Finally, it should be mentioned that additional simulations performed at 200, 220 and 240 K with a different potential model (the TIP4P/2005 model of ice) lead to very similar results, giving us confidence in the present conclusions.

3.6.2.4. Results concerning hydroxyacetone

3.6.2.4.1 Properties of the adsorption layer

Energy distributions Similarly to the case of oxalic acid, the distribution of the binding energy of a hydroxyacetone molecule with all the other hydroxyacetones at finite concentration as well as the interaction energy with the water molecules constituting the ice phase both at finite and infinitely low coverages have been calculated.

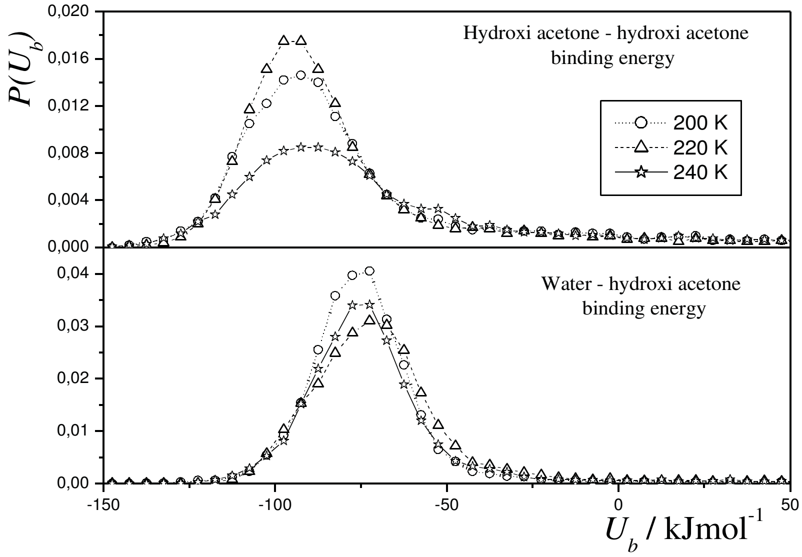

Figure 3.14 *Binding energy distributions of hydroxyacetone molecules adsorbed at the ice surface for different temperatures and at finite surface coverage.*

Irrespective of the simulation temperature, the U_b^w distributions in the infinitely low coverage case exhibit a single broad peak around -80 kJ mol^{-1}. Assuming that the average energy of a single hydrogen bond is roughly -25 kJ mol^{-1}, the position of this peak indicates that at infinitely low surface coverage the adsorbed hydroxyacetone molecule can form, on average, three H-bonds with the surrounding water molecules. At finite coverage, the hydroxyacetone-water binding energy is also characterized by a single broad peak (Figure 3.14) whose peak is however shifted to the higher values, being thus centered around –70 kJ mol^{-1}, still corresponding to the formation of approximately three H-bonds with water molecules. No significant shift of this peak has been observed upon increasing the temperature.

Hydroxyacetone-hydroxyacetone energy distributions are also characterized by a single broad peak positioned around -90 kJ mol^{-1}, at each simulated temperature. This means that one hydroxyacetone molecule forms, on average, between three and four H-bonds with other hydroxyacetone molecules. It should be noted, however, that this single broad peak also exhibits a shoulder extending up to -50 kJ mol^{-1}, indicating that some hydroxyacetone molecules are rather tied to their neighbors by only two H-bonds. The number of these weakly tied molecules seems to increase with the temperature, a feature which might be due to a larger disorder in the adsorbed layer when the temperature is higher.

3.6.2.4.2 Evaluation of the potential model

Naturally the results of these MD simulations are strongly dependent on the model chosen to calculate the hydroxyacetone/water interactions. The comparison with the experimental values of the adsorption enthalpy shows that the potential model used here (which is, to the best of our knowledge, the only one available in the literature) certainly overestimates the hydroxyacetone/ice interaction by about 20 %, which is admittedly a poor agreement. In addition, the experimental values were obtained on the basis of the Langmuir analysis which disregards lateral interactions within the adsorbed layer. This assumption is certainly not fully valid here because the hydroxyacetone layer is characterized by large lateral interactions between neighboring molecules (Fig. 3.13), and this should be also taken into account when comparing the calculated and measured values. Nevertheless, the results of this MD study can by no means be considered as sufficiently accurate and should be regarded as a maximum semi-quantitative description of the adsorption behavior. Due to weakness of the model used for these simulations, it would have been meaningless to perform such detailed analysis of the structural and orientational characteristics of the molecules in the adsorbed layer as in case of the oxalic acid/ice system. It should be noted that such a detailed study must have been preceded by extensive work on the development of a valid model for hydroxyacetone which would go definitely beyond the scope of my PhD thesis.

3.6.3 Molecular dynamics modeling of aerosols and their phase behavior [4,5]

3.6.3.1 Introduction

One of the main goals of this work is to investigate the size distribution and the structure of aerosol particles formed by dicarboxylic acids of different carbon chain length, namely oxalic and malonic acid. The other main interest of this study is to shed light on the complexity of the phase behavior of binary aqueous aerosols of these compounds, with special interest in the tropospherically relevant part of the phase diagram. The applicability of atomistic simulations in studying aerosols is also demonstrated by this study.

Hydrogen bonding binary mixtures in general are known to exhibit closed-loop phase diagram in the liquid phase. In an initially mixed, barostated system, upon the increase of temperature demixing will occur at the lower critical temperature of mixing. This phenomenon is due to the increase in the orientational entropy connected to the breakage of hydrogen bonds between different kinds of molecules and formation of bonds between like molecules. Naturally, above the upper critical temperature, due to the increasing energy of thermal motion, the molecules will have enough energy to overcome the free energy barrier of mixing. Little is known, however, about the existence of such behaviour among binary mixtures in the aerosol phase. There have been a number studies addressing the question of the phase behavior and the existence of special phases in aerosol systems yet we are unaware of a systematic investigation of the atmospherically relevant part of the (p,T) phase diagram of binary mixtures of water and aerosol forming dicarboxylic acids, which might be due to the fact that it is inconvenient or experimentally impossible to record a phase diagram of such mixtures.

We have performed molecular dynamics simulations to model the structure of oxalic acid aggregates and to analyze the phase behavior of the binary oxalic acid/water aerosols under atmospherically relevant conditions. To complete this study, we have repeated simulations with the larger malonic acid molecule aimed at characterizin the effect of one additional CH_2 group on water adsorption. This approach can be related to the recent experimental work of Schill and Tolbert [120] who tried to provide simple parametrizations of organic ice nucleation efficacy by using the O:C ratio as a proxy for characterizing the organic aerosol hydrophilicity. We have also investigated the thermodynamic background of the phase behavior. The results concerning the phase behavior together with the structural and energetic characteristics are interpreted in comparison between the two types of acids/water binary aerosols to get a deeper insight into the possible relation between the carbon atom number (or the O:C) ratio and the aerosol's ability to act as a cloud condensation nucleus.

3.6.3.2 Computational details

Molecular dynamics simulations of the formation and stability of oxalic and malonic acid aerosols together with the adsorption of water on the aerosol particles at three different compositions, corresponding to 0, 55% (65% for oxalic acid), and 85 mole % water concentration have been performed using the GROMACS simulation program package.[109] Simulations of the neat oxalic and malonic acid aerosols have been carried out on the canonical (*N*,*V*,*T*) ensemble at 200 K. The adsorption of water on the aerosol particles has been modelled at the isothermal-isobaric ensemble at six different, atmospherically relevant pressure values ranging between 0.01 and 1 bar, and temperatures between 100 and 250 K. The temperature and pressure of the systems were controlled by means of the weak coupling algorithm of Berendsen et al. [110] In the case of malonic acid, for three randomly chosen temperature-pressure pairs calculations have been repeated using Nosé-Hoover thermostat [121,122] and the Parrinello-Rahman barostat[123] to examine the possible effect of the choice of temperature and pressure coupling algorithms on the results. The results obtained with the different coupling methods have turned out to be in good agreement with each other. All simulations were performed using a time step of 1 fs.

Water molecules have been described by the TIP5P[105] model. Malonic acid molecules were modelled by the OPLS potential[115], whereas oxalic acid molecules were described by exactly the same geometry and potential parameters as the ones used for simulating its adsorption on ice. Water molecules were fully rigid, while bond angle and torsional flexibilities were allowed for the oxalic and malonic acid molecules. The geometry of water, and bond lengths in the case of oxalic and malonic acid molecules were kept fixed by means of the SETTLE[111]and LINCS[112] algorithms, respectively. The potential energy of the systems has been calculated exactly in the same manner as for the adsorption of oxalic acid and hydroxyacetone on ice, with the exact same cutoff scheme applied to account for the long range electrostatic interactions by the PME method.[16] For the sake of a more clear analysis we have repeated some of the simulations of the malonic acid/water binary aerosols without periodic boundary conditions, to ensure that the obtained results are meaningful and do not originate from any possible artefact resulting from translational periodicity, more precisely from an unphysical confinement of water molecules between periodic images of the aerosol particles.

To create the oxalic and the malonic acid aerosol we have placed a nucleus consisting of five molecules in the middle of a cubic simulation box having an edge length of 54.5 Å, to serve as a nucleation core, around which 120 more acid molecules were placed randomly. These initial systems have been equilibrated by a 1 ns long simulation on the (*N*,*V*,*T*) ensemble at 200 K. Once a stable aerosols have been formed, equilibration runs of 5 ns, performed under the same conditions have been launched. Simulations have been repeated with a system of double density for both acids, consisting of 240 randomly placed oxalic molecules around the nucleation grains to check the dependence of the formed aerosols on the initial density of the system. The largest stable aggregates found for each type of acid (consisting of 58 molecules in case of oxalic acid and of 212 in the case of malonic acid) have been taken as a model of an aerosol particle for our further studies devoted to the investigation of adsorption of water on oxalic and malonic acid nuclei. From the stable dicarboxylic acid aerosols the binary systems have been prepared as follows. The stabilized oxalic and malonic acid aggregates have been placed in the middle of an empty cubic simulation box having the edge length of 70 Å. For modelling the different water concentrations, in the case of oxalic acid 100 and 300, whereas for malonic acid 300 and 1500 water molecules have been placed randomly in two-two identical copies of the basic box. Each system has been equilibrated primarily on the canonical (N,V,T) ensemble for 4 ns at a temperature as low as 100 K. The pre-equilibrated systems have then been further equilibrated for 1 ns on the isothermal-isobaric (N,p,T) ensemble at 6-6 different, atmospherically relevant temperature and pressure values, namely 100, 150, 175, 200 , 225 and 250 K, and 0.01, 0.05, 0.1, 0.25, 0.5 and 1 bar, respectively. Each of these simulations has been followed by a 1 ns long production run performed under the same conditions during which 1000 equilibrium configurations, separated by 1 ps long trajectories each have been saved for the analyses. A total number of 36 simulations has thus been performed to reconstruct the phase behavior of the binary oxalic acid/water system and the same number of simulations has been carried out to provide us with detailed information about the malonic acid/water binary aerosols.

Common points in the analysis In such binary mixtures, the structural characteristics are well visible by looking at equilibrium snapshots, or as a more quantitative approach they might be investigated by means of detailed cluster analysis. Binding energy distributions on the other hand, are useful tools to provide us with information about the hydrogen bonded network of the aerosol. We have thus calculated the $P(n)$ distribution of the size of acid clusters disregarding water molecules, that of the water clusters without the acid molecules, and also the cluster size distributions taking both components into account for all the possible pressure and temperature pairs at both compositions. During the course of this analysis two malonic or oxalic acid molecules were considered to be hydrogen bonded if the distance from any of their hydrogens to any of the hydroxylic or carboxylic oxygen atoms of the other malonic or oxalic acid molecule was smaller than a cut-off distance of 2.45 Å or 3.5 Å respectively. The distance between the carboxylic and hydroxyl oxygen atoms had to be smaller than a cut-off value of 4.6 Å and the hydroxyl O - hydroxyl O distance had to be smaller than a cut-off of 3.5 Å. A water and a malonic or oxalic acid molecule have been considered to be connected by hydrogen bonds if the H(acid) – O(water) and the hydroxyl O(acid) – O(water) cut-off distances turned out to be smaller than the cut-off of 2.65. In the same way, two water molecules were considered to be hydrogen-bonded neighbors if the distance between their oxygen atoms did not exceed the value of 3.3 Å, while the smallest of the possible oxygen-hydrogen distances were also smaller than 2.45 Å. The cut-off values listed above were obtained as the abscissa value of the first minima of the corresponding pair correlation functions. Moreover, to get a deeper insight in the energetic changes that occur during and as a result of the phase transitions, and furthermore, to shed light on the energetic reasons underlying the changes in the characteristics of the different parts of the phase diagram, we have calculated the distributions of the binding energy between a water molecule and all the other waters ($P\left(U_w^b\right)$) and between a malonic or oxalic acid molecule and all the water molecules ($P\left(U_{ac}^b\right)$).

3.6.3.3 Results concerning oxalic acid

3.6.3.3.1 Characterization of the pure aerosol

The simulated pure aerosol phase of oxalic acid molecules has been proven to be polydisperse, with a size distribution of stable particles ranging from trimers and tetramers to particles consisting of 50-60 molecules. This size distribution is apparently independent of the original density of the system, as roughly the same distribution of particles have been obtained after doubling the initial density of molecules around the nucleation grain. It has, on the other hand, been found to depend largely on the temperature. At temperatures higher than 225 K only formation of small oligomers, consisting of 3 -10 molecules occurs, probably due to the increasing thermal motion, which acts against the formation of bigger clusters. As already mentioned above, a big aggregate (stable at 200 K) of 58 oxalic acid molecules has been chosen as a model of an aerosol particle for our further studies devoted to the investigation of water adsorption on oxalic acid nuclei.

3.6.3.3.2 Phase diagrams of the the oxalic acid/water binary system

The phase diagrams have been calculated at two water concentrations which have shown markedly different behaviour according to the measurements of Braban et al., [124] which have proven to be relevant for atmospheric studies. At 65 mole %, the concentration of water has not yet been high enough to fully hydrate the molecules of the oxalic acid aggregate. For this composition, the formation of oxalic acid dihydrates as well as efflorescence have a low probability. On the other hand, at a relative composition of 85 mole % both efflorescence and dihydrate formation could occur with a higher probability. Figure 3.15 a shows the phase diagrams obtained from our simulations, at the two different compositions.

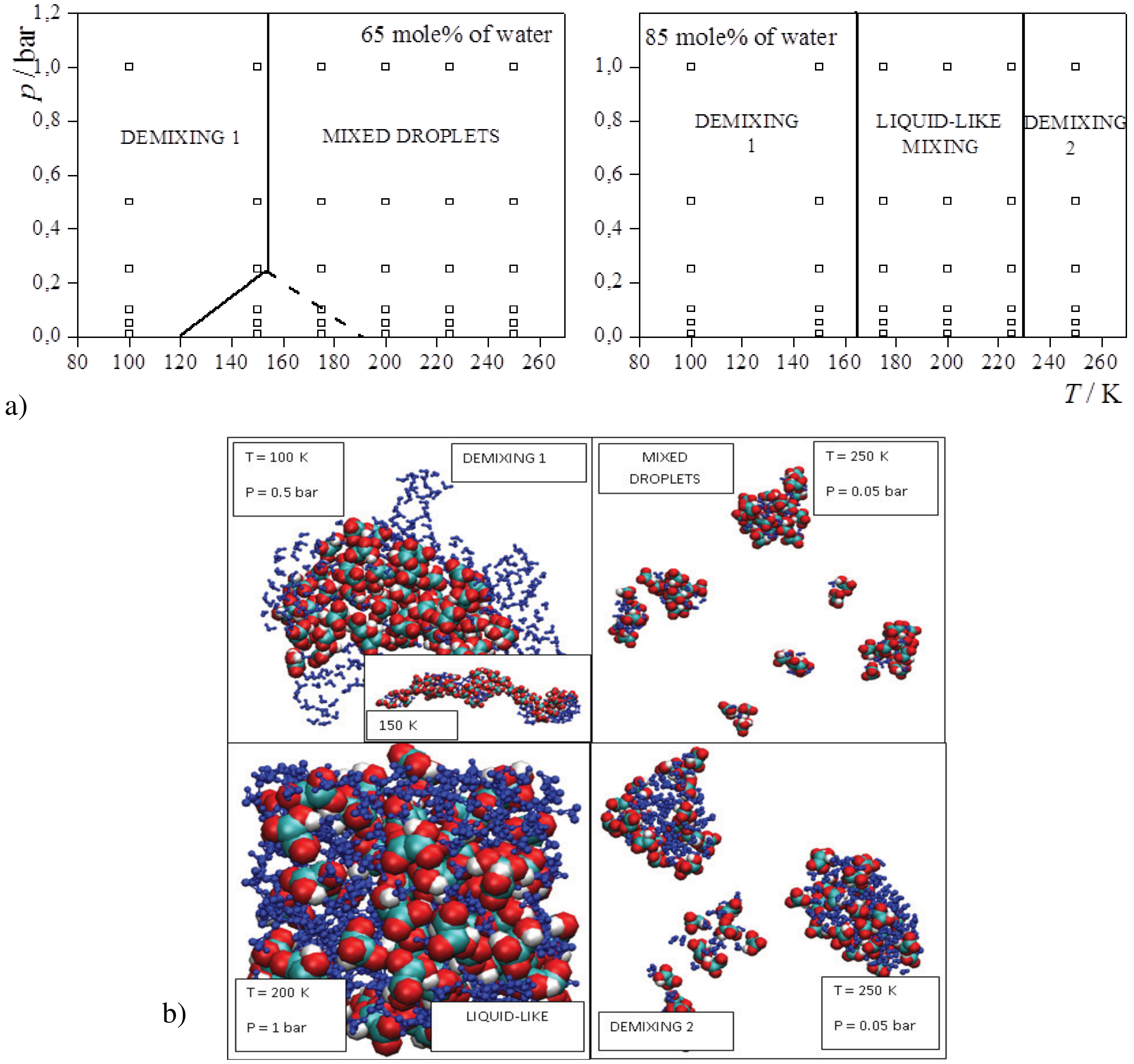

***Figure 3.15** a) (p,T) phase diagram of the water/oxalic acid binary aerosol at 65 mole% of water content (left panel) and at 85mole% of water content (right panel).b)Equilibrium snapshots of the four different phases observed in our simulations.*

System of 65 mole % water content At this composition, the phase diagram exhibits three distinguished phase transitions. The first type of phase, observed below 175 K for pressures higher than 0.2 bar and below 150 K for very low pressures, comprises of one big oxalic acid grain with water molecules adsorbed on its the surface as seen in the top left panel of Fig. 3.15. b. The presence of this single aggregate is also evidenced by the single peak of the total cluster size distributions calculated by taking both waters and oxalic acids into account, whose position corresponds to the total number of particles in the system. Total cluster size distributions together with those calculated disregarding water and oxalic acid molecules, respectively are shown in Figure 3.16. a and b for the two examined water concentrations. Cluster size distributions of oxalic acids (Fig. 3.16. a middle panel) analyzed together with the equilibrium snapshots confirm that in this temperature and pressure range the system consists of one oxalic acid particle, whose average size is independent from the exact value of the temperature and the pressure and is equal to the total number of oxalic acid molecules in the system. On the other hand, size distribution of the water clusters (Fig. 3.16. a top panel) shows that the vast majority of the adsorbed water molecules are not present as monomers; instead, they tend to form small clusters whose size ranges between 5 and 20 molecules.

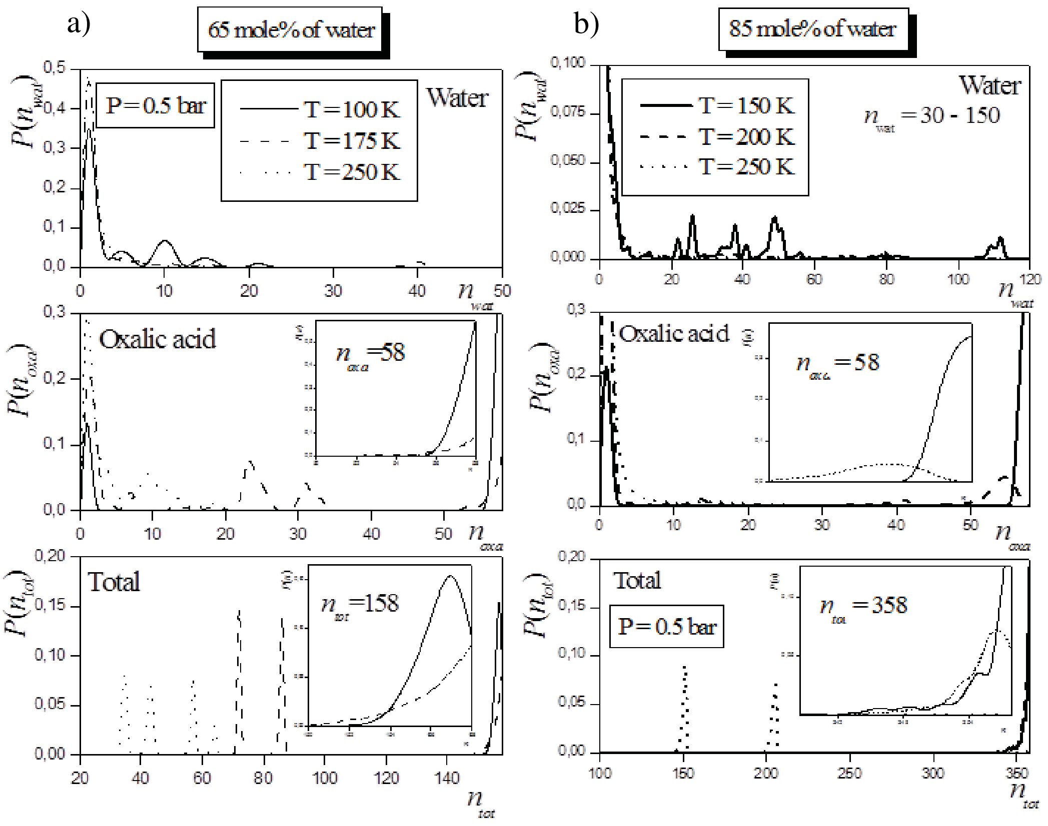

Figure 3.16. *Cluster size distribution as observed at a) 65 and b) at 85 mole% of water content. Top panels show the cluster size distribution of water molecules disregarding oxalic acids, middle panels show that of oxalic acid clusters without taking waters into consideration, whereas the distribution of the total cluster size (including both species) is presented in the bottom panels.*

This finding evidences that water molecules form small three-dimensional clusters attached to the oxalic acid aggregate rather than a monolayer at the surface of the oxalic acid grain. Moreover, taking a closer look at the equilibrium snapshots, we may conclude that the shape of the aerosol is distorted by the increasing temperature quite significantly. Namely, at very low temperatures the aerosol is nearly spherical, whereas at 150 K it already becomes rather elongated, having a rod-like structure. Regardless of the shape of the oxalic acid aggregate, water adsorption occurs preferably on the convex parts of the surface of the particle (as seen from the snapshots). This latter effect might originate from the fact that at the convex parts of the surface the possible electron donating functionalities, i.e., the hydroxylic and the carboxylic oxygen atoms lie further away from the electron acceptor H atoms of the hydroxyl groups of other molecules, and hence oxalic acid - oxalic acid hydrogen bonding has steric hindrance. This effect is further enhanced by the fact that small water oligomers are simply excluded from the concave curvatures because of their size. These conclusions are supported by the analysis of the energy distributions, shown in Fig. 3.17.a

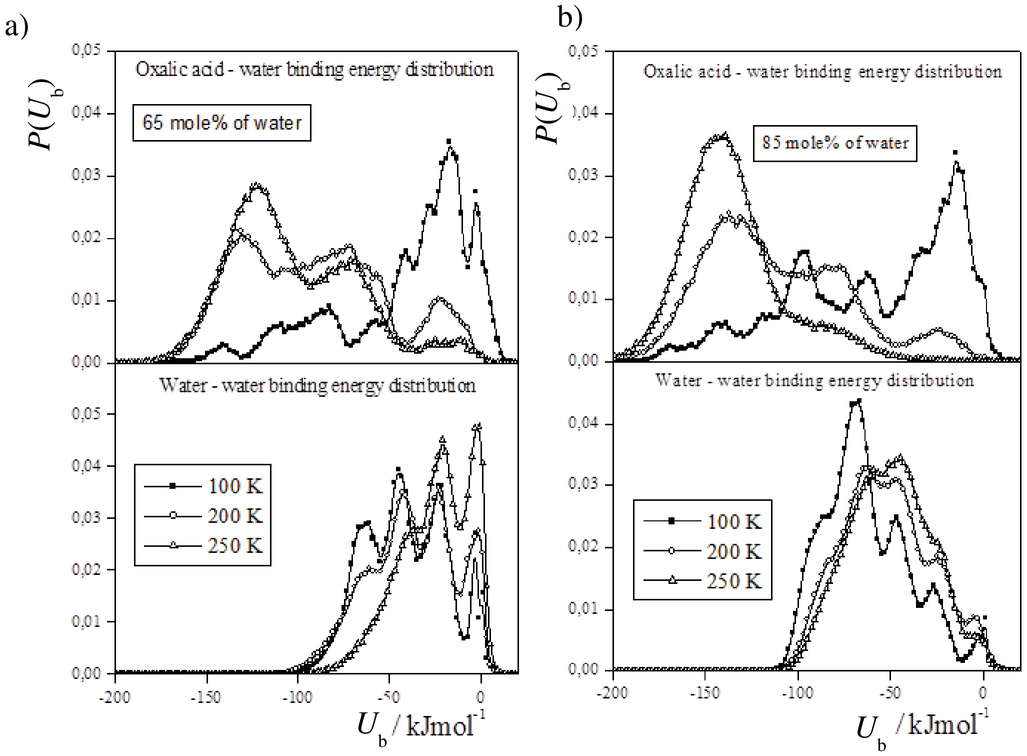

__Figure 3.17__ Binding energy distribution of oxalic acid molecules to waters (top panels) and water molecules to other waters bottom panels, at a) 65 and b) 85 mole% water concentrations.

Indeed, at low temperatures, the distribution of the oxalic acid - water binding energy $P\left(U^{b}_{oxa-wat}\right)$ exhibits a large peak in the range between -40 and -10 kJ/mol, and two much smaller peaks between -120 and -80, and between -150 and -130 kJ/mol, respectively. The first one may be related to the vast majority of oxalic acid molecules which are not directly tied to water molecules, whereas, the two peaks at lower energies correspond to oxalic acid molecules that form more than three hydrogen bonds with adsorbed water clusters, assuming, as usual, that the average energy of a single hydrogen bond is roughly between -25 and -20 kJ/mol. In the same way, $P(U_w^b)$ exhibits three peaks around -25, -50, and -75 kJ/mol, corresponding to the formation of one, two, and three hydrogen bonds between neighboring water molecules, respectively, thus supporting our previous conclusions on the formation of three dimensional water clusters.

Upon increasing the temperature the system undergoes a phase transition (Fig. 3.15 a) to form rather small mixed droplets of oxalic acid and water (see the snapshot given in Fig. 3.15 b). However, this kind of phase transition, i.e., the disintegration of the aerosol particle with the water molecules adsorbed on its surface into smaller binary water/oxalic acid droplets has only been observed at pressures higher than 0.25 bar. Indeed, in the low pressure region, ranging from 0.01 to 0.25 bar we have found a transition zone, in which small aerosol particles are visible but mixing does not occur yet, instead, water clusters are adsorbed at the surface of the smaller oxalic acid aggregates. This region has been found at temperature values ranging between 150 and 200 K. Due to the limited size of the simulated system, we cannot undoubtedly assign this behaviour to the formation of a new phase. Thus, this transition is marked by a dashed line in Figure 3.15 a. Above 200 K, regardless of the value of pressure, the formation of smaller mixed droplets was observed. The cluster size distributions of the total systems exhibit not only peaks at smaller values of n (Fig. 3.16.a, bottom), but also a larger number of peaks than that observed for the low temperature case. This visible increase in the polydispersity of the system, together with the subsequent decrease in the average cluster size serves as a clear indication for the disintegration of the aerosol into smaller droplets. However, the exact structural properties of these droplets, i.e., whether they are mixed or they form smaller biphasic aerosol particles remain still questionable. By examining the cluster size distributions calculated with the exclusion of waters (Fig. 3.16.a, middle) and of oxalic acids (Fig. 3.16.a, top), we can conclude that the size distribution of the oxalic acid clusters follows the same pattern as that of the total cluster size, i.e., the number of peaks increases and the size of the clusters decreases with increasing temperature, whereas at high temperatures water molecules exist almost exclusively in the monomer form. This is confirmed by the progressive disappearance of the high energy peak in $P(U_{ac}^b)$ (Fig. 3.17.a, top) which indicates that the number of oxalic acid molecules not being in direct contact with water molecules is considerably smaller than in the demixed phase, due to the smaller size of the oxalic acid aggregates in the high temperature phase. Similarly, in the distributions of the water-water binding energy $P(U_w^b)$, the low energy peak around -75 kJ/mol progressively disappears when the temperature increases (Fig. 3.17.a, bottom), while a growing peak is observed around zero, corresponding to the increasing number of water monomers in the system.

System of 85 mole % water content At this considerably higher value of relative water content, a markedly different phase behavior has been observed (Fig. 3.15 a, right panel). This is already evident from simple visual analysis of the equilibrium snapshots taken from the simulations. The first significant difference found is that, in this case, pressure has none the slightest effect on the phase transition zones. Increasing the temperature has, on the other hand, led to the appearance of three different phases in the phase diagram between 100 and 250 K. In the low temperature range, a phase very similar to what has been seen in the case of 65 mole % system has been found (called previously as "demixing phase"). Even the temperature-induced change in the shape of the oxalic acid aggregate has been found to be similar to that observed for the low water content case. However, it has to be noted that for this system the disintegration of the stable aggregate of oxalic acid with water clusters adsorbed on its surface has occurred at a higher temperature. The cluster size distribution in this demixing phase has shown almost the same characteristics as seen at 65 mole % water content. The only rather obvious difference between to two concentrations is that in the case of higher water content the water clusters are also larger (see the top of Fig. 3.16.b). In the high concentration case, adsorbed water clusters may consist of up to 110 water molecules.

As it has been already mentioned, mixing of the oxalic acid molecules and the waters takes place above 175 K, resulting in the formation of a liquid-like mixed phase, consisting of one big cluster, resembling a simple binary liquid mixture of these two compounds (see the snapshot in Fig. 3.15 b). This transition is evidenced by the distribution of the cluster size in this region. Indeed, the distribution of the total cluster size in this case exhibits one single peak (Fig. 3.16.b, bottom), corresponding to the formation of a single big aggregate containing all the oxalic acid and water molecules. On the other hand, the size distribution of the oxalic acid clusters exhibits a broad peak at around $n = 55$ besides the rather intense peak of the monomers. Similarly, the size distribution of the water clusters has a peak at $n = 1$, followed by several, rather broad peaks around the cluster sizes of about 30, 80 and 140. The average number of hydrogen bonded water neighbors of a water molecule turned out to be two, based on energetic analysis. This finding suggests that, as a result of mixing, the initially densely packed oxalic acid aerosol has a less dense structure thus water molecules can penetrate into the voids of the oxalic acid network. Further, besides the oxalic acid clusters water aggregates surrounding oxalic acid monomers also occur in the system. This structure resembles the structure of liquid mixture of two compounds of self-associating ability, such as the aqueous solution of oxalic acid at low temperatures. The phenomenon of liquid-like mixing is also indicated by the considerable shrinkage of the box edges, and hence the volume of the system, giving rise to the formation of a liquid phase consisting of a mixture of water and oxalic acid molecules. It should be emphasized that this behavior is only seen here in the case of the system of higher (i.e., 85 mole %) water content, whereas in the system of lower water content the box edge length turned out to be insensitive to the thermodynamic conditions.

Another peculiarity of this system is that above the temperature value of 225 K one more phase transition takes place, manifesting in the formation of small, demixed aerosol particles, whose structure differs significantly from the demixing phase observed at low temperatures. First of all, according to the total cluster size distributions, the particles have a considerably smaller average size here than in the demixed phase at lower temperatures. Namely, in contrast to the single peak at the n value corresponding to the total system size at 150 K, here the total cluster size distribution exhibits two peaks, one at around $n = 150$ and another one around $n = 200$ (Fig. 3.15.b, bottom). More importantly, the structure of the aerosol particle also shows considerable differences from that at low temperature, as in this high temperature demixed phase the individual oxalic acids molecules are seen to be adsorbed on the surface of water clusters (see the corresponding snapshot in Fig. 3.15). Clearly, careful examination of the snapshots rules out the possibility of the formation of big liquid-like oxalic acid clusters. This finding is supported by the cluster size distribution of the water and oxalic acid molecules, which indicate the presence of small, liquid-like water droplets in the simulation box, and that in this high temperature demixed phase oxalic acid molecules exist solely in monomer form. This conclusion is confirmed by the distribution of the oxalic acid - water binding energy $P(U_{ac}^{b})$, the broad peak of which at around -150 kJ/mol evidences strong interactions between oxalic acid and water molecules (Fig. 3.17.b, top).

3.6.3.4 Results concerning malonic acid

3.6.3.4.1 Characterization of the pure aerosol

Simulation of the pure aerosol phase of malonic acid molecules resulted in the formation of one big spherical particle whose size depended on the initial density and a few monomers in equilibrium with the big cluster. This result differs greatly from what had been observed previously for oxalic acid. In the case of the neat malonic acid aerosol the equilibrium cluster size depends on the initial concentration whereas for oxalic acid the size distribution in the observed atmospherically relevant density range has been found to be concentration independent. More importantly, a much bigger average aerosol size has been observed in the case of malonic acid molecules. For the smaller average initial density, equilibrium cluster size has turned out to be about 100 molecules whereas for the larger initial concentration the aerosol in equilibrium with the remaining monomers and dimers consisted of, on average, 210 malonic acid molecules. The characteristic size of the aerosol particles and subsequently the number of nuclei formed at the same initial density may be an important factor in the efficacy of the aerosols as cloud condensation nuclei. We speculate that the formation of a number of smaller clusters is more advantageous from the point of view of cloud condensation than that of a bigger aggregate whose overall surface area is smaller. This suggestion is in agreement with the finding of Schiller and Tolbert stating that the higher the O:C ratio the more effective the aerosol as a cloud condensation nucleus. However, this question may be further elaborated by a comparative investigation of the atomistic structure and the energetic characteristics of oxalic acid-water and malonic acid/water binary aerosols.

3.6.3.4.2 Phase diagram of the malonic acid/water binary mixture

The phase diagram of malonic acid water mixtures has turned out to be much simpler than what had been observed previously for the oxalic acid/water mixtures. First of all, unlike for the oxalic acid- water systems, we have observed no dependence of the (p,T) phase diagram on the water concentration, at least in the range covered by our simulations. The (p,T) phase diagram of malonic acid/water mixtures consists of two phases and pressure, just like in case of oxalic acid, has turned out to be an largely irrelevant variable concerning its effect over phase transitions. The phase

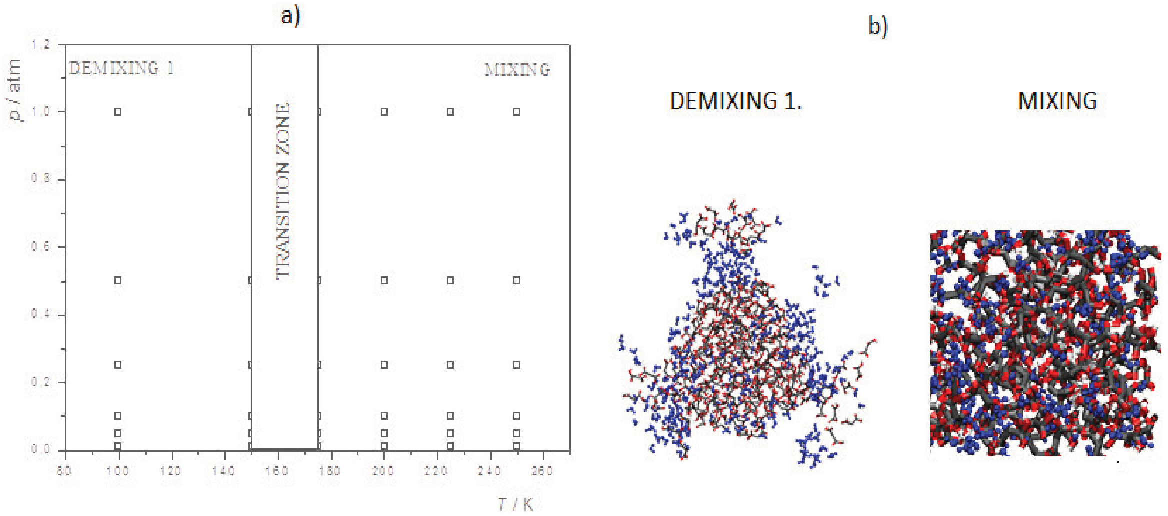

Figure 3.18. *The phase diagram of the malonic acid/water aerosol as obtained for the system containing 300 water molecules (a), equilibrium snapshots illustrating the characteristic features of the two*

phases (b).

diagram of the malonic acid/water system as obtained for the lower water concentration together with the equilibrium snapshots of the different phases are shown in Figure 3.18.

At low temperatures malonic acid forms one single big aggregate on which water molecules are adsorbed in the form of small clusters, while for temperature values above 150 K we see a mixing of the two phases in a manner which does not involve the breakage of the original big aggregate. Comparing the equilibrium snapshots of oxalic acid aggregates ((Fig 3.15 b) and that of malonic acid (Figure 3.18. b), it is clear that we may identify the demixing phase of the malonic acid/water systems with the low temperature demixed phase observed for oxalic acid/water systems, whereas the mixed phase is apparently similar to liquid-like mixing observed at high water concentration at intermediate temperatures. Cluster size distributions calculated at four temperatures values for both of the malonic acid/water systems are shown in Figure 3.19. Total cluster sizes are seen in the top panel, whereas the middle and the bottom panels contain size distributions of malonic acid molecules disregarding waters, and that of water molecules disregarding malonic acids, respectively. It is evident from the total cluster size distributions, i.e.: the distribution calculated involving both water and malonic acid molecules, that regardless of the temperature no dissociation of the binary aggregate happens. It can be observed in the top panels Fig. 3.19 for both concentrations that the average size of the binary aggregate varies only slightly with temperature and the peak is definitely broader for higher temperature values but apart from this change, which may be attributed to thermal motion, no significant difference and even more importantly no appearance of any peak in the region of small aggregation numbers is visible. Taking a closer look at the malonic acid cluster size distributions calculated disregarding water molecules we can draw the conclusion that the initial size of the malonic acid aggregate remains also practically intact when temperature is increased. Here the decrease of the mean value of cluster size is observable at higher temperatures and subsequently the appearance of some monomers and dimers is visible in the snapshots, however the number of these is statistically irrelevant as they do not appear in the cluster size distribution as peaks at small values of n_{mal}. It can thus be concluded that the qualitative picture suggested by the equilibrium snapshots, stating that in case of malonic acid/water mixtures the initial aggregate does not dissociate at higher temperatures, is supported by the total cluster size distribution as well as the size distribution of malonic acids.

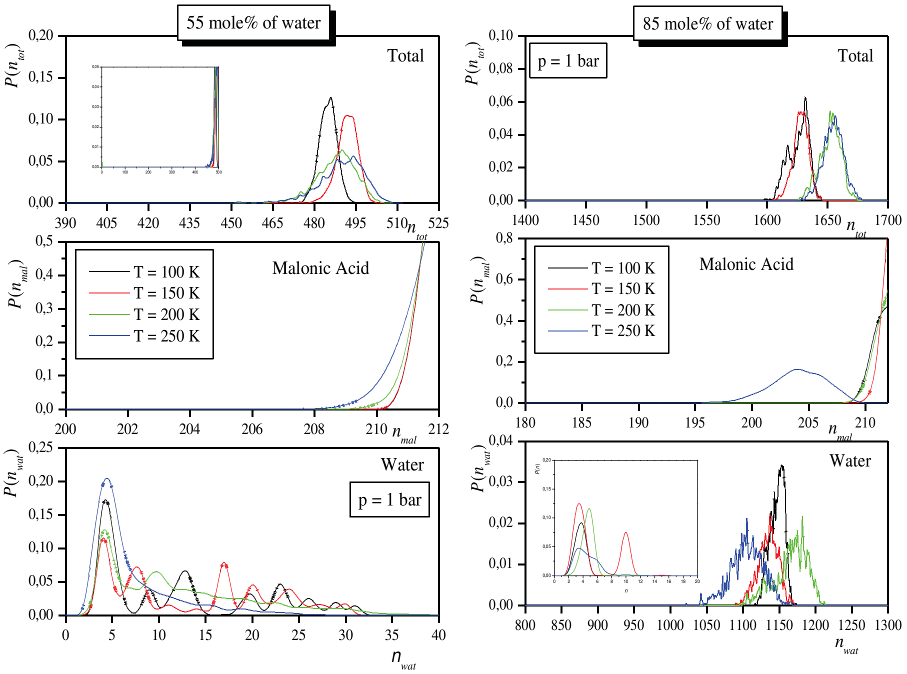

Figure 3.19. *Cluster size distributions of malonic acid water binary aerosols for 55% (a) and for 85% water content (b) at 4 different temperature values 100 (black line), 150 (red line), 200 (green line) and 250 K (blue line). Top panels show the total cluster size distributions including both malonic acid and water molecules, middle panels display the malonic acid cluster size distributions disregarding water molecules, finally water cluster size distributions can be seen on the bottom panels.*

Analyzing the size of water clusters in the binary systems may provide us with more detailed information about the structure of the adsorbed layer and may also give at least qualitative picture about the mechanism of mixing. At lower temperatures, for the lower concentration a multi peak distribution consisting of peaks of similar intensity with average abscissa values ranging between $n_{wat} = 5$ and $n_{wat} = 30$ can be observed. This finding implies that adsorption happens in a way that water clusters are trapped on the surface of the malonic acid aggregate at low temperatures. At higher temperatures the peaks characterised by larger mean abscissa values gradually disappear, and in the mixed phase water clusters containing on average three-five molecules are the predominant. Such small aggregates of water can more easily penetrate into the voids in the malonic acid aerosol. Thus the following mixing scheme can be suggested. At higher temperatures water clusters consisting originally of 20-30 molecules break up into smaller ones. At the same time more intensive thermal motion of the malonic acid molecules initiates the formation of relatively big voids and voids within the core of the aggregate, causing it to expand in diameter, allowing the small water clusters to penetrate into the core of the aggregate and fill the voids. We should note here that at the higher water concentration the tendency described above is partially washed away by the fact that water molecules in that case are present in a sufficient amount to form a percolating network. This network is originally situated around the malonic acid core at low temperature values. On the other hand, similarly to what has been observed for the lower concentration system, we can also see the appearance of quite high-intensity peaks at small aggregation number values suggesting that it is possible to imagine a mixing mechanism similar to what has been described for the low concentration case, which would be in accordance with the fact that malonic acid and total cluster size distributions behave very similarly for both examined cases. It should also be remembered that the mixing mechanism suggested simply by looking at the distribution of cluster sizes is highly speculative, and one has to investigate the energetic background to get a justification, and to form an at least semi-quantitative but still far from exact, picture of the processes underlying the occurring phase transitions.

Distributions of the average binding energy for all the possible molecule pairs for each concentration are shown in Figure 3.20. Top panels show the average binding energy distribution of

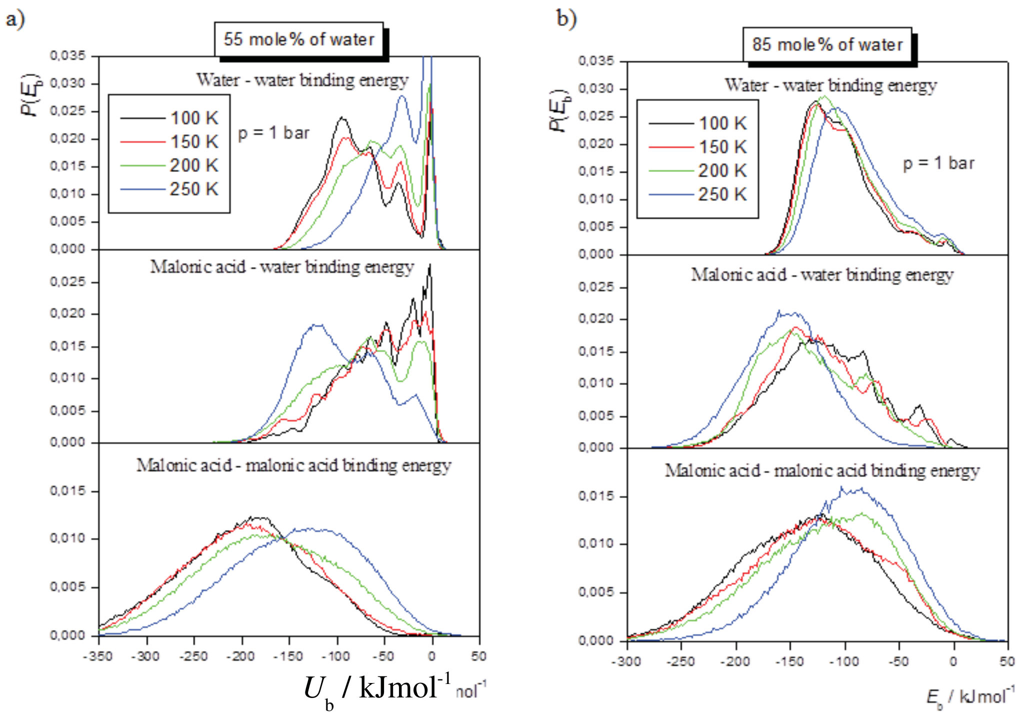

Figure 3.20. *Binding energy distributions of malonic acid water binary aerosols for 55% (a) and for 85% water content (b) at 4 different temperature values 100 (black line), 150 (red line), 200 (green line) and 250 K (blue line). Top panels show the average binding energy of one water molecule with all other waters, middle panels show the same binding energy distributions between water and malonic acid molecules, whereas bottom panels display the average binding energy distribution of one malonic acid molecule with all other molecules of the same gender.*

water molecules, the middle panels display the distribution of the mixed binding energies, whereas on the bottom panels the distribution of the average binding energy of one malonic acid molecule with all the other molecules of the same kind is seen. First of all we should note that, just like in the case of cluster size distributions, binding energies are not affected significantly by the concentration of water in the system, thus it is sufficient to analyse results obtained for one of the systems in details. Looking first at the water-water binding energy distributions, we can see four peaks at every temperature. The four peaks are situated roughly at U_b = -125, -75, -25 and 0 kJ/mol, corresponding to arrangements in which one water molecule forms 5, 3, 1 and 0 hydrogen-bonds with other waters.The peak at 0 kJ/mol comes obviously from the fact that most water molecules are too far from each other to be bonded. The relative intensity of these peaks varies greatly upon increasing the temperature. Namely lower energy peaks corresponding to the formation of a larger number of water-water hydrogen-bonds gradually loose intensity and eventually are withdrawn into a shoulder at the highest temperature. This suggests that the breakage of hydrogen-bonds formed between water molecules is a favoured process at higher temperatures. The same tendency is observed for the malonic acid-malonic acid binding energy distributions, with the exception that in this case we obtain a very broad distribution which appears to be unimodal. At low temperature the peak is found at -200 kJ/mol. It corresponds to the case when one malonic acid forms hydrogen-bonds with eight other malonic acids. With increasing the temperature this peak is shifted towards higher energy values. In the mixed phase the maximum of the distribution corresponds to -100 kJ/mol. This value suggests that in the mixed phase malonic acid molecules loose about half of their hydrogen-bonds towards other malonic acids. The loss of any kind of hydrogen-bond is an energetically unfavourable process, which is compensated by the subsequent formation of others at high temperature. This finding is evidenced by examining the temperature dependence of the malonic acid-water binding energy distributions. It is visible on the middle panel of Fig 3.20. that at low temperature mixed hydrogen-bonds, although present to some extent, are less likely to form, whereas the abscissa values of the peaks of this distribution are shifted towards more negative values at higher temperature, suggesting that the probability of the formation of mixed hydrogen-bonds is more likely at higher temperatures. This finding is in good agreement with the observed mixing at temperature values higher than 150 K.

3.6.3.5 The thermodynamic background of the phase behavior

As the phase behaviour of any system in the isothermal-isobaric ensemble is driven by the effort of the particular system to minimize the value of the characteristic thermodynamic state function, namely the Gibbs free energy, whose formula is the following:

$$G = U - TS + pV \quad , \tag{3.5}$$

where G is the Gibbs free energy of the system, U stands for the internal energy, T is the temperature, S is the entropy, while p and V stand for the pressure and volume, respectively. According to this equation, the Gibbs free energy can be minimized by maximizing the entropy and/or minimizing the volume and internal energy.

It is well known that in binary mixtures of hydrogen bonded liquids the total entropy comprises of two major terms:

$$S_{\mathrm{tot}} = S_{\mathrm{comp}} + S_{\mathrm{or}} , \tag{3.6}$$

where S_{comp} is the compositional entropy term, and S_{or} is the so-called orientational entropy.[125] The S_{comp} term is naturally maximised during the course of mixing, while the orientational entropy (S_{or}) maximized if the system is demixed, since the number of possible orientations of the intermolecular hydrogen bonds is higher in the biphasic than in the mixed system. This pattern is further elaborated if, instead of a liquid, an aerosol phase is concerned, since the entropy of such a system can also be changed by changing the size of the aerosol. Namely, the entropy of a polydisperse system consisting of smaller aggregates is suspected to be somewhat higher than that of a single particle consisting of the same number of molecules. Thus, in the case of an aerosol phase, the expression for the entropy has the form of

$$S_{\mathrm{tot}} = S_{\mathrm{comp}} + S_{\mathrm{or}} + S_{\mathrm{disp}} , \tag{3.7}$$

where S_{disp} denotes the entropy term connected to the polidispersity of the system.

From the simulations performed in this work, it is impossible to calculate the Gibbs free energy or its entropic contribution directly. However, if we check the tendency and magnitude of the change of the U+pV term, which is readily accessible from the simulation, we may have an indication of the importance of the entropic contribution as a possible driving force of the phase transitions. Namely, if the U+pV sum shows no tendentious change with pressure or temperature, and still a phase transition is observable, it can be concluded that entropy is the main driving force of the phase transition. We have thus calculated the U+pV term for all of our systems of interest.

Comparing these values it becomes obvious that pressure has practically no effect on this contribution. The increase of the temperature, on the other hand, leads to a slight (i.e., in the order of k_BT), yet visible increase of the $U+pV$ term of the Gibbs free energy for both molecules at both compositions. However, the *increase* of this term does not account for the observed phase behaviour, since phase transitions are driven by the *decrease* in the Gibbs free energy. Therefore, we can draw the conclusion that the main driving force of the observed phase transitions must be the entropic contribution. Selected values of the U and pV terms as well as their sums obtained for the oxalic acid-water model system are collected in Appendix B, Table 1.

The effect of temperature As a general pattern, we may conclude that in the low temperature range the TS term has relatively small impact on the Gibbs free energy of the aerosol particles, while the $U+pV$ term is found to be slightly lower here than at higher temperatures. However, upon increasing the temperature the Gibbs free energy can be more and more efficiently tuned by changes in the entropic contribution. These facts may account for the finding that at low temperature a single big aggregate with water clusters adsorbed on its surface represents the stable phase at both compositions for both acids. It also explains that above a certain temperature mixing occurs, even if the structure of the resulting mixed phase differs qualitatively due to the effect of composition. In a two component mixed binary system the S_{comp} term of the total entropy is necessarily higher than in a biphasic system characterized otherwise by the same set of intensive variables. On the other hand, by the formation of smaller droplets (as is seen in the case of the system of low water content for oxalic acid) the S_{disp} term can also be increased. It should be noted that the formation of a mixed liquid phase instead of the small mixed aerosols occurs in the case of higher water content or in case of larger carbon atom number, probably as a composition or chain length dependent effect which overcompensates the change in the dispersion term of the entropy. The effect of the composition and the carbon chain length on the phase behaviour of the system investigated is discussed in detail in the following sub-sections.

The effect of pressure As is seen on the phase diagrams of both compositions for both type of aerosols, the effect of pressure can be considered as being almost totally negligible. The only exception is seen in the low water content case of oxalic acid/water binary mixtures, where the mixing of the two components follows a slightly different mechanism at low than at high pressures. Namely, at low pressures the temperature induced disintegration of the big aerosol particles occurs at slightly lower temperatures, and it visibly precedes mixing of the two components.

The effect of composition The change in the composition has a marked effect on the energetic and *pV* contributions to the Gibbs free energy for both systems. As is clear from the data listed in Table 1 of Appendix B the internal energy of the systems of higher water content is considerably lower than that of the system consisting of fewer water molecules at each temperature-pressure pair. However, since the tendencies in the change of temperature and pressure are similar for both concentrations, this difference cannot account for the observed qualitatively different phase behaviour. On the other hand, oxalic acid - water binary aerosols have a specific characteristic, namely that above a certain water content they undergo a process called deliquescence, which is the uptake of water to form an outstandingly stable oxalic acid dihydrate (i.e., an aggregate consisting of one oxalic acid and two water molecules). The difference between the two systems considered here in this respect is that at the lower water concentration case one single mixed droplet built up by oxalic acid molecules hydrated by two water molecules cannot be formed with finite probability, whereas in the case of the higher water concentration the formation of such a droplet is possible. This difference may account for the fact that the temperature induced mixing occurs differently at the different compositions considered. On the other hand, for malonic acid/water systems, the effect of composition remains invisible in the phase behaviour observed in our studies, which is probably due to the overcompensating effect of one or more of the entropic terms.

The effect of the O:C ratio As it has been seen, the phase behavior of malonic acid/water mixtures differs greatly from what has been observed previously for oxalic acid/water mixtures under exactly the same conditions which, knowing that these molecules are consecutive elements of the homologous series of dicarboxylic acids, is a surprising finding. The molecules differ only in the fact that in malonic acid the two carboxylic groups are separated by a methylene group, thus this methylene group must be the reason for the differences observed in the phase behavior of the two mixtures. In the case of oxalic acid/water mixtures we have argued that the phase behavior is governed by entropic factors, since the *U-pV* term of the Gibbs free energy was found to show no tendentious change from one phase to another. The same holds for malonic acid/water mixtures. As it has been stated in the previous section about the thermodynamic background underlying the phase behaviour of binary aerosols, the entropic contribution (S_{tot}) to the Gibbs free energy can be, theoretically, expressed as the sum of three main types of contributions, S_{comp}, S_{or} and S_{disp}, where subscripts denote the total entropy, its compositional, orientational and dispersion contribution. The compositional term increases upon mixing regardless of the chemical nature of molecules constituting the binary system, thus this contribution should not be affected by the change in the carbon atom number. Dispersion always increases the entropy of any system, thus the formation of small dispersed mixed clusters in case of oxalic acid can be attributed to a favorable change in this contribution. On the other hand, in the case of malonic acid/water mixtures this term remains practically intact when crossing the phase boundary, since no dissociation of the aggregate can be observed. This results in a loss of entropy compared to the case of oxalic acid/water systems. However, the big aggregate of malonic acid is stable in both mixed and demixed phase, and its stability may be attributed to the decreased steric repulsion between the two carboxylic group, the increased flexibility of the malonic acid molecule compared to the oxalic acid, and the subsequent increase in the orientational degrees of freedom, due to the presence of the extra methylene group which separates the two carboxylic functional groups. All things considered the loss of orientational entropy due to the relative rigidness of the oxalic acid structure is compensated by increasing the dispersion term by the formation of small aggregates.

Considering the fact that a set of several small aerosol particles, due to their larger total surface area, serve probably as better nuclei for water adsorption and subsequently cloud condensation than one single big aggregate, we may conclude that our studies are in agreement with experimental results stating that aerosols characterised by a higher O:C ratio have a great potential as cloud condensation nuclei. We are aware that the detailed study of this question has to be accompanied by an intrinsic analysis of the surface of the aerosols, which, however, due to their ill-defined geometrical structure, goes beyond the scope of a PhD thesis, and is part of the plans for future studies.

3.7 Summary

The behavior of two different types of solid surfaces, namely ice and organic aerosols, both of which are highly important in environmental issues such as air pollution and climate evolution has been studied by means of Monte Carlo and molecular dynamics simulations. We have turned our attention primarily to the interaction of these surfaces with other components of the atmosphere under conditions characteristic of the troposphere.

The GCMC study of the adsorption of acetaldehyde (in agreement with experiments) on ice revealed that the adsorption of acetaldehyde on ice follows the Langmuir behavior in the entire pressure range of the existence of vapor phase acetaldehyde. Correspondingly, the adsorption layer is found to be monomolecular up to the point of condensation. Acetaldehyde molecules are attached to the ice surface by one single hydrogen bond, formed typically with the dangling H atoms of the surface water molecules. They prefer to align preferentially perpendicular to the ice surface, or they may adopt tilted alignments with a tilt angle (relative to the ice surface plane) larger than 50°. Upon saturation of the adsorption layer the range of this tilt angle gets narrower, and the preference of the acetaldehyde molecule for the perpendicular alignment becomes stronger. Further, it is found that the CH_3 group strongly prefers to point as straight away from the ice surface as possible within the constraint set by the alignment of the molecular plane. The analysis of the binding energy distribution as well as that of its ice and lateral contributions revealed that at high surface coverages lateral interactions contribute to the total binding energy comparably with the ice-adsorbate interaction. Lateral attraction originates from the dipolar interaction of the neighboring acetaldehyde molecules, the dipole vectors of which thus adopt head-to-tail or antiparallel-like relative arrangements. The heat of adsorption at infinitely low surface coverage (i.e., the binding energy of a single acetaldehyde molecule by the ice phase) turned out to be -36 ± 2 kJ/mol from the experiment, in a clear accordance with the simulation result of -34.1 kJ/mol. Considering that this value is about 20% lower than what was previously obtained for formaldehyde,[15] and also the relative abundance of acetaldehyde in the upper troposphere, the present study clearly stresses the possible atmospheric importance of the adsorption of acetaldehyde molecules on ice grains.

Molecular dynamics studies of the adsorption of oxalic acid on hexagonal ice at different temperatures at very low and at finite surface coverages, the latter being close to one monolayer of oxalic acid molecules allowed us to draw the following conclusions. Firstly, although the oxalic acid–water interaction is very strong at infinitely small coverage due to the possible formation of a large number of hydrogen bonds between the adsorbed oxalic acid and the surface water molecules, the results of the simulations at finite coverage show the predominant role played by the oxalic acid–oxalic acid lateral interactions in the adsorption/desorption process. These interactions are even stronger than the water-water and water-oxalic acid interactions, in agreement with what was inferred from the experimental results. Secondly, when increasing the temperature these strong lateral interactions favor the formation of oxalic acid aggregates at the ice surface, preventing oxalic acid desorption. Instead, the holes formed within the oxalic acid layer allows the departure of water molecules before the desorption of oxalic acid, again in accordance with experimental observations. Indeed, water molecules can escape quite easily from the ice surface through the ducts created within the adsorbed layer by the oxalic acid aggregation. This suggests that the balance between water/ice, water/VOC and VOC/VOC interactions is crucial question from the point of view atmospheric processes. MD simulations of hydroxyacetone have yielded merely qualitative results concerning the adsorption and have shown the strong need to develop a potential model to describe the interactions of this molecule with water.

Molecular dynamics studies of oxalic acid/water and malonic acid/water binary aerosols aimed at reconstructing the tropospherically relevant part of their phase diagram and at understanding the process of water nucleation induced by organic aerosols in the troposphere have allowed us to draw the following conclusions. In the case of oxalic acid, we have found that the equilibrium size of neat aggregate was rather small (consisting of about 60 molecules), and independent of the initial density of the system. For malonic acids on the other hand we found a correlation between the equilibrium cluster size and the initial density of molecules in the simulation box, namely at double density, double-sized clusters have been formed. On the other hand the equilibrium cluster size has been (at any initial density) considerably higher than in the case of oxalic acid aggregates. Analyzing the phase transitions of the binary aerosols of these two species with water has shown the following results. Water concentration has affected the phase behavior of the oxalic acid/water binary mixtures rather strongly, whereas this factor has turned out to be uninfluential in the case of malonic acid/water aerosols. Temperature seems to have been the parameter governing the phase behavior of these binary mixtures, whereas the effect of pressure has been found to be marginal in both cases, which finding suggests that the phase transitions are driven by the entropic ($T\Delta S$) term to the Gibbs free energy, and is thus in accordance with the fact that changes in the U+pV term of the Gibbs free energy would not favor the observed phase transition. The striking difference between the behavior of the two types of aggregates, consisting of otherwise rather similar molecules, as cloud condensation nuclei can be attributed also to entropic reasons. Namely, oxalic acid aggregates may increase their total entropy efficiently by forming rather small dispersed particles, which is energetically clearly unfavorable, due to the breakage of several hydrogen bonds accompanying the process, whereas the increased flexibility of malonic acid molecules facilitates the increase of entropy solely through increasing the number of possible conformations within one single aggregate. If we consider that the total surface area of several small aggregates is considerably larger than one single big particle, and that their affinity to scavenge other molecules is thus considerably higher, we may conclude that this above finding is in accordance with the experimental study stating that O:C ratio characterising the organic compound is in direct correlation with its cloud condensation potency.

Chapter 4

Fluid interfaces

4.1 General features of fluid interfaces

Liquid/liquid and liquid/gas interfaces are of paramount importance in several fields of applied chemistry, such as separation science.[126] Besides their crucial role in the field of applications, fluid interfaces have been in the foreground of fundamental research as well. Their most important and probably most peculiar characteristic is the formation of thermal capillary waves,[127] Capillary waves, in general, are defined as waves propagating at phase boundaries, whose dynamic behavior is governed by surface tension or gravity depending on the wavelength. Capillary waves are visible even macroscopically if a raindrop falls into a pond or we simply remove the cork from the washbasin and let the water flow. A capillary wave of an atomistic interface is different from macroscopic waves in the sense that the perturbation leading to its formation is more often a thermal than a mechanical fluctuation. On the atomistic scale gravity can be neglected, thus the effect of thermal motion and surface tension are responsible for the formation and propagation of microscopic capillary waves. According to the capillary wave theory, the area of the distortion of the initial intrinsic surface caused by the thermal motion is proportional to the energy of the wave and the constant of proportionality is the surface tension. The distortion of the surface by these waves plays a significant role in defining the equilibrium structure and dynamic behavior of the interface.

Liquid/gas and liquid/liquid interfaces are similar to solid interfaces in the sense that their behavior is governed, besides the above mentioned capillary waves, by the effort to reduce the interfacial excess of the Gibbs free energy. The difference between solid and fluid interfaces in that sense is that unlike solid surfaces, interfaces of two fluid phases may minimize the interfacial excess properties by minimizing their surface area, not only by means adsorption. Adsorption at fluid interfaces, though obeys similar physico-chemical rules, is a phenomenologically different process than what has been observed for solid interfaces. As it has been described in the previous chapter, adsorption at solid interfaces happens strictly when molecules of the opposite (fluid) phase get trapped by free adsorption sites of the surface increasing the number of interacting neighbors of that particular site, and thus reducing the interfacial excess Gibbs free energy of the solid surface. On the contrary to solid surfaces, the increased molecular mobility in a fluid phase allows the relatively rapid exchange of molecules between the bulk fluid phase and its surface. This may result in the enhancement of the concentration of one of the compounds of a liquid mixture at the interface, and its subsequent depletion in the bulk phase. The process of the formation of such an interfacial region enriched in one or more of the components of a mixture is called adsorption in the case of liquid interfaces. It is obvious that this kind of adsorption does not necessarily reduce interfacial excess by increasing the number of interacting neighbors of a surface molecule. The way by which the reduction of the excess free enthalpy is eventually achieved depends greatly on the structural and chemical peculiarities of the surface active species, i.e.: the one which resides preferentially at the interface.

4.1.1 Examples of surface active species

There are several compounds of different chemical nature which may act as surface active components in liquid mixtures. Take the case aqueous solutions. The spectrum of possible surface active solutes ranges from small organic molecules, through surfactants and polymers to simple and composite ions, each of them having a different mechanism and thermodynamic driving force of the adsorption, and each of them forming an adsorption layer which differs greatly in its structural and dynamic characteristics. It should be noted that surface activity of these molecules can be either positive, if their concentration is enhanced in the vicinity of the interface, or negative in which case of region of depleted concentration will be found in the interfacial region. The possibility of competitive adsorption on the other hand further elaborates the scope of properties to be investigated. In the following sections I describe some examples of surface active species and I shed light on the peculiarities of competitive adsorption in the case of polymers and surfactants.

4.1.1.1 Surfactants

The most well-known among surface active molecules are undoubtedly surfactants who are, in general, ionic or non-ionic molecules with amphifilic structure, built up in general of a hydrophilic headgroup, which may be anionic (SO_4^{2-}), cationic (-CH_2-NMe_3^+)or neutral (-C_2H_4O-oligomers), and a hydrocarbon chain of variable length, which plays the role of the hydrophobic part. In their aqueous solutions they tend to adsorb at the interface with such an orientation that minimizes the interaction of the latter with water molecules, which results in the formation of a self-organized layer of surfactants at the interface in equilibrium with molecules and micelles dissolved in the bulk phase. This phenomenon is well-known since the early years of colloid chemistry, and it has been described several times, for instance by Kunjappu et. al. in 1989,[128] at that time without seeing the system in an atomistic resolution, by *in situ* experimental investigation of the aqueous solutions of several surfactants.

The main thermodynamic driving force of surfactant adsorption at the interface of its aqueous solution lies, besides the obvious electrostatic and dispersion terms, in the occurrence of the so called hydrophobic interactions. In spite of the misleading nomenclature, hydrophobic interactions are not the interactions which appear between two hydrocarbon chains. Instead, the key process of such interactions is the formation of locally frozen water domains along the long hydrocarbon chains in their aqueous solution, which leads obviously to the loss of entropy. When these hydrocarbon chains are expelled from the aqueous phase, the „melting" of these domains and the subsequent recovery of the hydrogen-bonded network of water causes a considerable change in the Gibbs free energy of the system. Even if the thermodynamic behavior could be fully explained by looking at data about the heat of adsorption, characterizing the molecular level structure of the adsorption layer certainly necessitates a high-resolution approach. Questions like the possibility of the lateral aggregation of the surfactants at the interfaces, or the dependence of their orientation on the surface coverage as well as their lateral diffusion at the surface are readily accessible via computer simulations, and their better understanding can facilitate the development of more accurate adsorption models and may verify the concepts of existing theories, which in turn can be of use in planning industrial procedures.

4.1.1.2 Polymers

Polymers are another group of molecules among which several surface active species can be found. Some water soluble polymers, such as poly(ethylene-oxide), or poly(vinyl-pyrrolidone), have been found to decrease the surface tension of their aqueous solution significantly. Their surface activity can be attributed to a reason different from what has been described for surfactants. In studying their adsorption one has to consider the conformational changes in the macromolecule chain and its significant effect on the overall entropy of the system in order to obtain a meaningful model of the adsorbed layer. The structure of the adsorbed polymer layer, at least in the case of neutral polymers, can be in general imagined in the following way. The polymer is anchored to the surface by some of its segments, the so called train segments, whereas the rest of the monomer units arranged in loops pointing towards the bulk aqueous phase. Figure 4.1 shows a model of an adsorbed polymer molecule at the liquid/vapor interface.

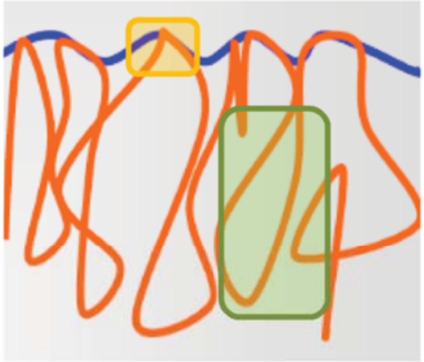

Figure 4.1. *Schematic illustration of a linear polymer adsorbed at the interface of two immiscible fluid phases. An example of train segments, anchoring the molecule to the surface is highlighted by yellow whereas one of the loops is shown with a green highlight.*

This simple model has been first described by Jenkel and Rumbach in 1951[129] on the basis of analyzing the adsorbed amount of polymers per unit area.

Upon further investigation of polymer adsorption by experiments several questions arose concerning the mechanism of the adsorption. Consequently, quantitative description of the surface layer, containing at least some segments of the adsorbed polymer, at the air/water interface has grown out to be a subject of continuous experimental and theoretical investigations. One of the most intensively used methods to study adsorption of polymers are surface tension measurements. The results of such studies have been traditionally interpreted in terms of the Gibbs equation describing the relationship between the surface excess concentration of th i^{eth} compound Γ_i and the surface tension (γ) in terms of the bulk concentration (C_i)

$$\Gamma_i = \frac{-1}{RT} \left(\frac{\partial \gamma}{\partial \ln C_i} \right)_{p,T} . \qquad (4.1)$$

However, several fundamental problems are related to this widely used practice. First of all, polymers are usually polydisperse, thus their aqueous solutions contain molecules of different chain length, and the proper use of the Gibbs equation would require the exact knowledge of the composition of the system.[130] Another important drawback is the lack of detailed knowledge about the concentration dependence of the polymer activity coefficients in the bulk phase, which is problematic in the semidilute regime, where experimental evidence shows a significant additional surface tension reduction, which implies that the activity coefficient is a complex function of the bulk concentration. [131,132,133,134,135] Even in the less complicated case of dilute polymer solutions with fairly narrow size distribution of the components, some anomalies of the adsorption behavior were reported for a variety of systems. [136,137,138]

4.1.1.3 Competitive adsorption of polymers and surfactants at liquid interfaces

In the majority of industrial applications polymers do not appear as simple aqueous solutions. Mixtures of polymers and surfactants are more common as main ingredients in the different products of the paint, pharmaceutical as well as home and personal care industry. The efficacy of such products depends strongly on the surface properties of these components. On the other hand, mixed surface layers of amphiphils and macromolecules are also important model systems of fundamental research in colloid chemistry and nanoscience. The combined practical and fundamental interest explains the motivation behind the intensive research done in the last two decades targeting such systems.[139,140,141]

The interaction between ionic surfactants and neutral, flexible polymers in the bulk phase of their solution is generally described as a cooperative process, during which micelle-like aggregates of the surfactant, wrapped around by the polymer[142,143] are formed at the critical aggregation concentration (cac).[144,145] Interestingly, this classical physical picture of the bulk interaction between neutral polymers and ionic surfactants is historically based on the interpretation of the surface tension isotherms of poly(ethylene oxides) (PEO) of different size in the presence of sodium dodecyle sulfate (SDS). In the pioneering work of Jones[142], it was assumed that the polymer adsorption is negligible, and hence the shape of the surface tension isotherms reflects solely the features of the bulk phase interactions. Namely, as the total surfactant concentration exceeds the cac, the bound amount of surfactant increases rapidly, and this is accompanied by a slow increase of the equilibrium surfactant activity, while above the critical micellar concentration (cmc) the isotherm becomes practically constant. Since the publication of this classical work a number of studies devoted to this problem have been carried out including the measurement of surface tension isotherms.[130],[146,147,148,] Rather similar surface tension isotherms were observed in a great deal of polymer/surfactant mixtures, regardless of the variety of the surface activity of the polymers involved in these studies with or without the surfactant.[134,135,149,150,151] Therefore, in order to rigorously correlate the bulk binding characteristics of the surfactant with the results of the surface tension measurements the classical assumption of the negligible extent of adsorbed polymer needs to be modified.

Several neutron reflection studies have been devoted to the investigation of the surface layer of aqueous mixtures of neutral polymers and surfactants having surface tension isotherms of the classical shape with two breakpoints, since this method combined with selective isotope substitutions is capable of determining the composition of the surface layer. In these studies, depending on the systems, either displacement (e.g., in the case of PEO/SDS and PEO/lithium dodecyle sulfate[152,153]) or enhanced adsorption of the polymer (e.g., for poly(vinyl pyrrolidine)/SDS)[132,137] was observed below the cac. It was also evidenced that in some systems there must be some adsorbed polymer even when the surfactant activity is close to the cmc. These controversial results suggest that the full understanding of the surface tension behavior of a specific polymer-surfactant system requires the simultaneous and independent investigation of the surface compositions and bulk phase interactions, which is, however, far from being a trivial task with the usual experimental techniques.

4.1.1.4 Surface activity of ions

Small molecular non-amphiphilic ions may also perform surface active behavior at the interface of their aqueous solutions, although data obtained from classical surface tension measurements suggests that the interfacial tension increases upon addition of inorganic salts to their aqueous solutions.[154,155,156,157,158] The first explanation of this phenomenon by Onsager and Samaras [159] was based on describing the ion as a simple point charge and the interface as a sharp and flat discontinuity between two continuous media of remarkably different dielectric permittivity. In the framework of this theory, the repulsion of ions from the interface is expected as a result of the force exerted on them by the image charge formed in the opposite phase.[160] This pioneering theory has been further developed by the addition of surface effects to the original model.[161,162,163,164,165,166,167,168,169] However, all the presently existing versions of the original theory predict the monotonically decreasing distribution of the ions upon approaching the interface along the surface normal axis, and eventually claim the existence of an ion free region situated right at the surface. Surface sensitive spectroscopy (SFG and SHG) measurements[170,171,172,173,174,175] disproved the general validity of the above described theory by detecting the enhancement of the ion concentration at the surface region for certain ions. These findings seemingly contradict the results of surface tension measurements, but considering the fact that these novel methods are able to detect solely the outermost surface layer of the systems while the classical surface tension measurements naturally involve the entire system, this contradiction is far from being sharp and evident. Thus an attempt to resolve these seeming contradictions could be made by such simulating the behavior of ions right at the fluid interface.

4.1.2 The dilemma of fluid interfaces – determining the intrinsic surface

The above-mentioned examples of open questions concerning fluid interfaces justify the need for the development of methods aimed at the separation of the interfacial layer and its treatment as an individual „phase", which is of crucial importance if one wants to study any of the above described phenomena. Computer simulations can be easily tuned for such tasks, as in any case they record the position of molecules, thus providing a piece of information that enables us to separate the interface from the rest of the surface, at least in theory.

In practice, one of the greatest dilemmas of scientists involved in investigating fluid interfaces is how to determine exactly the surface itself. Until very recently, the most commonly used method has been to define the interface as the region where the density of the phase changes from 90% to 10% of its bulk phase value. This approach is acceptable from the macroscopic point of view, however, with the recent rapid development of surface sensitive experimental methods and complementary computer simulation techniques, an increasing demand has been emerging for a more precise determination of the interfacial layer. Besides this, the density profile method to determine the interface is burdened by a serious systematic error of unknown magnitude which is due to the fact that thermal capillary waves, described in section 4.1, corrugate the surface on the atomistic scale. As a result of these capillary waves, the interface is molecularly rugged and the amplitude of the corrugations can be so large that some interfacial molecules may be identified as part of the bulk phase according to the above described definition. On the other hand, some molecules, which are part of the bulk phase (i. e.: are surrounded completely by molecules of the same phase) may be found in the zone where the density changes between 90% and 10% of the bulk phase value, and thus they will be regarded as interfacial.

This systematic error can be in principle corrected in atomistic simulations either by giving a functional form to the intrinsic covering surface[176,177] or by determining the full list of interfacial molecules. No matter how easy this task may seem knowing the exact spatial coordinates of every atom of a simulated system, it is in reality far from being trivial. Several methods have been described in the literature to determine the intrinsic interface between fluid phases. The first attempt to select the interfacial molecules was made by Stillinger who stated that interfacial molecules differ from bulk phase ones in the sense that they are in direct contact with a percolating volume of empty space.[178] This approach, though theoretically correct, was never routinely used due to the enormous computational demand of its algorithm. More than 20 years after Stillinger's theory had come to light, Chacón and Tarazona developed their so called Intrinsic Sampling Method which attempts at finding the covering surface that goes through at a set of pivot sites whose area is minimal. [179] They treat the surface as a smooth mathematical function, express it as the sum of its Fourier components, and minimize the normal component of its distance from the pivot sites in a conveniently chosen form to yield the real covering surface. This method determines the intrinsic surface in a self-consistent way. It had originally been developed for liquid/vapor interfaces and later extended for liquid/liquid interfaces as well. Another approach is the grid-based method of Jorge and Cordeiro,[180] who define the interface by dividing the simulation box by a fine rectangular grid whose resolution is larger than the average wavelength of the thermal capillary waves corrugating the surface parallel to the interface normal axis. In each of these grids they determine the position of the interface, and put the individual grids together to reconstruct the entire intrinsic surface. A different method was developed in our research group, which is based on probing the interface by spheres of a given radius which are moved along a set of gridlines parallel to the interface normal axis.[25] This method is described in details in section 2.7 since it has been used and further developed during my PhD studies, thus here I refrain from describing its principles. On the other hand it should be noted that a similar method was developed by Chandler and coworkers [181] for mapping the surface of proteins, that relies on moving the probe sphere along the interface. The advantage of this latter method is that it does not require the interface to be flat. Chowdhardy and Ladanyi introduced a completely different approach for identifying the interfaces.[182] Their Surface Layer Identification method is based on the idea that interfacial molecules are necessarily the closest to an opposite molecule. In practice they search over all possible pairs of the two opposing phases to find those molecules of the analyzed phase which are closest to any of the sites of the opposite phase. This method, unlike the ones described above, is seemingly free from any free tuning parameter, however it is connected to the presence of a condensed opposite phase.

The accuracy and computational cost of the above mentioned methods varies on a large scale. They have been thoroughly tested recently by Jorge[39,183] who compared their efficacy to the self-consisted method of Chacón and Tarazona. The results of these studies showed that the best compromise between computational demand and accuracy is the ITIM method which has been developed in our group. Nevertheless, the most important message of the comparative study is the necessity of using any of these methods when it comes to treating fluid interfaces.

4.2. Results concerning fluid interfaces

4.2.1 Competitive adsorption of polymers and surfactants at the free interface of water[6,7]

4.2.1.1 Introduction

This work is aimed at the investigation of the composition, the structure and the dynamics of poly(ethylene oxide) (PEO) chains adsorbed at the surface of their aqueous solutions in the absence and in the presence of an increasing amount of sodium dodecyle sulfate (SDS). The main goal of our studies have been to characterize the adsorption of the pure polymer, and to shed light on the thermodynamic reasons underlying the frequently observed competition of PEO and SDS molecules for adsorption sites at the aqueous interface, by detailed analysis of the mechanism by which the highly surface active polymer is displaced from the water surface in the presence of increasing amount of the surfactant.

PEO chains of various lengths have been simulated in a number of times in several different environments, such as the bulk phase of its aqueous solution[184,185,186,187,188] and melt,[189] inside[190] and at the surface of its crystalline phase[191] as well as at the free surface of liquid water.[192] Further, the adsorption layer of SDS[193,194,195,196] has also been simulated in a number of times both at the free water surface and at the liquid-liquid interface between water and various apolar liquids. However, in spite of the wealth of such studies, we are only aware of one single publication concerning computer simulation investigation of the mixed PEO-SDS system in the bulk phase of their aqueous solution,[197]whereas, to the best of our knowledge, the mixed adsorption layer of PEO and SDS has never been investigated yet by means of computer simulation methods.

We have investigated the state of PEO molecule adsorbed at the free water surface by means of molecular dynamics simulations. The results are interpreted in terms of the novel Identification of the Truly Interfacial Molecules (ITIM) method,[25] modified to treat the interfaces of polymer solutions. To characterize the macroscopic structure of the interface the distribution of the polymer segments along the macroscopic normal of the interface has been calculated. In order to get a deeper insight into the properties of the adsorption layer at the molecular level, structural, dynamic and energetic properties of the polymer segments have been evaluated both in the two bulk phases and at the interface. For this purpose, their partition between the bulk liquid phase, the interfacial region and the vapor phase has been determined. The conformational state of the polymer has been characterized by the chain end-to-end distance. This investigation has been completed by analyzing the mean residence time and the binding energy of the polymer segments in the above three different parts of the system. Upon finding an apparently well-functioning model for the PEO molecule, which was a task of crucial importance concerning the success of the studies, and upon checking the validity of this model through the above mentioned calculations, we have extended this study by adding an increasing amount of SDS to the system to investigate the competitive adsorption of the neutral polymer chain and ionic surfactant molecules at the free water surface. The trajectories resulting from the simulations have also been interpreted here in terms of the modified version of the ITIM method.[25]

4.2.1.2 Computational details

Molecular dynamics simulations Molecular dynamics simulations of the mixed PEO/SDS adsorption layer of seven different surface coverages of the surfactant, (Γ_{SDS} = 0, 1, 2, 3, 4, 5 and 6 μmol/m^2), at the free water surface have been performed on the canonical (N,V,T) ensemble at $T = 298$ K. The systems contained 2798 water molecules, two identical PEO chains, consisting of 50 (-CH$_2$-O-CH$_2$-) monomer units and two chain terminal -CH$_3$ groups (bearing zero charge to provide the electroneutrality of the polymer), 0, 12, 24, 36, 48, 60 and 72 DS$^-$ molecules, and the same number of Na$^+$ counterions. The X, Y and Z edges of the rectangular basic simulation box were 290.0 Å, 31.4 Å and 31.4 Å long, respectively, X being the axis perpendicular to the macroscopic plane of the interface. The simulations have been performed using the GROMACS 3.3.2. program package.[109]The equations of motion have been integrated in time steps of 1 fs. The temperature of the system was kept constant by means of the weak coupling algorithm of Berendsen et al. The bond lengths of the PEO chains and DS$^-$ ions have been kept fixed using the LINCS algorithm[112] whereas the geometry of the water molecules has been kept unchanged by means of the SETTLE method.[111]

The total energy of the systems has been calculated according to generally used protocol described in Chapter 3.3 for the simulation of oxalic acid/ice interactions. All interactions have been truncated to zero beyond the molecule (or monomer unit) based center-center cut-off distance of 9 Å. Lennard-Jones interactions have been neglected beyond this cut-off distance, whereas the long range part of the Coulomb term was accounted for by using the Particle Mesh Ewald (PME) method.[16] The intramolecular energy term included contributions from bond angle bending and torsional rotation of both the PEO chains and DS^- ions.

Water molecules have been described by the rigid, three site SPC model, [198] while the potential parameters of the Na^+ and DS^- ions have been taken from the GROMOS force field.[199,200] For the alkyl chains of the surfactant and for the PEO molecule both bond angle bending and torsional flexibility have been allowed. The torsional potential of the alkyl chains of the DS^- ions has been described by the Ryckaert-Bellemans potential function.[201] The PEO chains have been described by the potential model proposed by Shang, Wang and Larson.[197] This model is also based on the GROMOS force field, with the modifications that the $C12$ (repulsion) Lennard Jones parameter of the O atoms ($C12$ being equal to $4\varepsilon\sigma^{12}$) is scaled down by a factor of 0.55, and the Coulomb repulsion of two such oxygens in 1-4 position is scaled down by a factor of 0.65. These scaling factors were optimized to reproduce the experimental hydration enthalpy as well as the trans/gauche ratio of the PEO segments also in systems consisting SDS. The CH_3 and CH_2 groups of the PEO chains as well as of the DS^- ions were treated as united atoms. The intermolecular interaction parameters of the water, PEO and SDS molecules used in the simulations are summarized in Appendix A, Table 2, converted to the corresponding σ, ε values.

The initial coordinates of the PEO chains have been created by the following algorithm. First, ten segments have been attached to each other in a completely stretched conformation. Then the energy of this system has been minimized by the steepest descent method and have been equilibrated for 50 ps on the isothermal-isobaric (N,p,T) ensemble at $p = 1$ bar and $T = 298$ K. In the next step another chain of 10 stretched segments has been attached to the free (CH_2-) end of the equilibrated chain and the energy minimization and (N,p,T) ensemble simulation runs have been performed on the elongated chain. This process has been repeated until a pre-equilibrated chain consisting of 50 ($-CH_2-O-CH_2-$) monomer units was obtained. Then two identical pre-equilibrated chains have been placed in the vicinity of the two pre-equilibrated liquid/vapor interfaces, of an aqueous system built up by 1598 water molecules. This system has been equilibrated for 20 ns to obtain a stable adsorption layer of the polymer. The dodecyle sulfate adsorption layer has then been created separately from a layer consisting of 36 DS^- ions in an ordered arrangement. This number of the DS^- ions corresponds to the highest surface coverage considered. Lower coverages have been created by randomly removing sufficient number of DS^- ions after thorough equilibration of the original layer. Two equilibrated layers, consisting of the adequate number of DS^- ions have then been placed to the close vicinity of both surfaces of the water/PEO system, and simultaneously an equal number of Na$^+$ counterions has been inserted randomly into the bulk liquid phase to retain electroneutrality. In this way, the number of SDS molecules was always equal at the two surfaces in the basic box. These systems have been further equilibrated for 5 - 8 ns, followed by a 7 ns long production run, during which 3500 sample configurations, separated by 2 ps long trajectories each have been saved for the analyses.

ITIM analyses In this study we have used a modified version of the ITIM method[25] to identify the water molecules and PEO monomer units that are located right at the surface of the aqueous phase. It should be noted that the layer of the adsorbed DS$^-$ ions was always regarded as part of the opposite, apolar phase. Indeed in cases of low surface coverage the hydrocarbon chains of these ions indeed always penetrated to the vapor phase, whereas in cases of high surface coverages they formed an apolar layer, locally very similar to a liquid hydrocarbon phase, right beyond the aqueous surface. Thus, hereinafter we simply refer to the vapor phase of the systems consisting of various amounts of hydrocarbon chains as the apolar phase.

Slight alteration of the ITIM analysis has been necessary due to the following reason. Although the water penetration to the apolar phase has always been found to be negligible, we have observed the formation of short PEO loops in the vapor phase, even in the absence of a hydrocarbon region. The monomer units forming such loops can stop the probe sphere, and hence they can easily be misidentified as interfacial rather than apolar phase units, thus truly interfacial water molecules or PEO monomer units located beneath these apolar phase loops may be shielded from the probe sphere causing systematic error. To avoid this error and to distinguish between the PEO monomer units being in the aqueous phase, right at the interface, and in the apolar phase we have used the following procedure. First, the list of the PEO monomer units that are in the apolar phase is determined. These monomer units are identified by the lack of their close water neighbors. A water molecule is regarded as being close to a PEO monomer unit in this respect if the distance of their O atoms is smaller than 3.1 Å, i.e., the first minimum position of the corresponding radial distribution function. The PEO monomer units identified this way are considered as parts of the apolar phase and are disregarded from the analysis. After the selection of such monomer units interfacial water molecules and PEO segments are determined, i.e.: the ITIM analysis is carried out regarding only the non-apolar phase PEO segments and water molecules. Following the identification of the truly interfacial water molecules and PEO monomer units the remaining PEO segments and water molecules are regarded finally as being in the bulk liquid phase.

In the ITIM analyses a probe sphere of the radius of 2.0 Å has been used, in accordance with the simple notion that reasonable results can only be expected if the probe sphere size is comparable with the size of the atoms constituting the phase of interest. In order to obtain a sufficiently fine resolution of mapping the interface, thus we have used a set of test lines spaced equally in a 64×64 grid along the macroscopic plane of the interface. Residues have been represented by their Lennard-Jones σ parameters (When performing the ITIM analyzes the two surfaces of the aqueous phase present in the basic simulation box were treated separately, and the obtained results were averaged not only over the 3500 sample configurations per system, but also over these two surfaces per sample configuration.

4.2.1.3 Results

4.2.1.3.1 The distribution of the components along the surface normal axis

Density profiles The mass density profiles along the macroscopic interface normal axis *X* of the seven systems simulated are shown in Figure 4.2, whereas the number density profiles of the water and PEO oxygen atoms, the SDS S atoms and chain terminal CH_3 groups as well as of the Na^+ counterions are shown in Figure 4.3 as obtained in the systems containing 0, 2, 4 and 6 µmol/m^2 SDS at the surface of the aqueous phase.

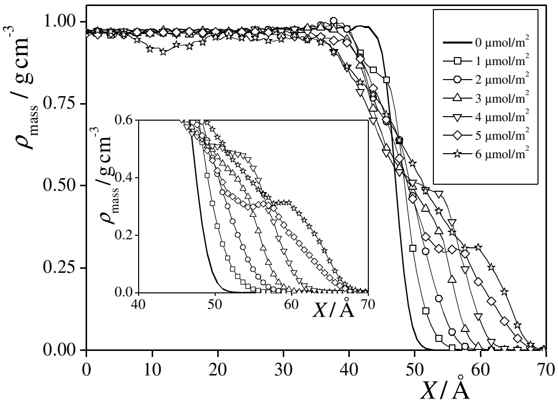

Figure 4.2 *Mass density profiles of the systems containing 0 (thick solid line), 1 (squares), 2 (circles), 3 (up triangles), 4 (down triangles), 5 (diamonds), and 6 µmol/m^2 (stars) SDS at the surface of the aqueous phase. All profiles shown are averaged over the two interfaces present in the basic simulation box. The inset shows the profiles in the interfacial region on a magnified scale.*

As is seen, the mass density profile of the SDS free system is rather similar to that of liquid water; it changes smoothly from the value characteristic of the liquid phase to zero. The 90-10% width of this profile, i.e., the distance range within which the density drops from 90% to 10% of the bulk liquid phase value is about 4.5 Å. However, upon adding SDS to the system the drop of the mass density profile at the interface becomes considerably less sharp, the region of intermediate densities between the two phases becomes much broader than in the lack of SDS. Thus, the 90-10%

width of the profiles corresponding to the systems of 1 and 2 μmol/m^2 SDS content are already 9 and 13 Å, respectively. This broadening of the intermediate density region reflects the appearance of the SDS adsorption layer, which is characterized by a lower density than the aqueous phase. Further increase of the SDS surface density leads to the development and broadening of a shoulder of the mass density profile around $X = 55$ Å (see the inset of Fig. 4.2). The first traces of this shoulder are already apparent in the profile of the 3 μmol/m^2 SDS system, whereas in the 5 and 6 μmol/m^2 SDS systems a well-developed shoulder is seen with mean density of 0.3 g/cm^3. The appearance of this shoulder reflects broadening of the adsorbed SDS layer, presumably due to changes in the orientation (i.e., from parallel to perpendicular alignment relative to the interface) of the adsorbed molecules.

More detailed information on the structure of the mixed PEO/SDS adsorption layer can be obtained from the number density profiles of the different atoms. In the lack of SDS the PEO molecule is adsorbed at the water surface by a minority, i.e., about 20% of its monomer units, whereas a large part of the polymer chain forms relatively long bulk liquid phase loops.

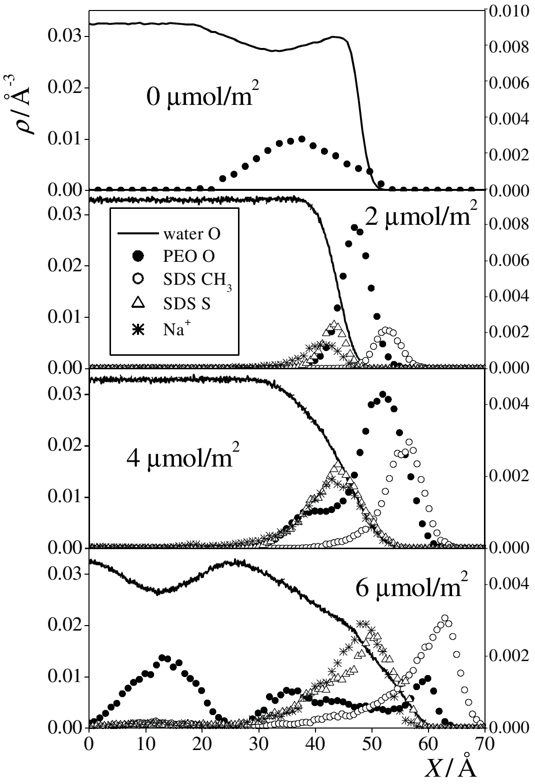

__Figure 4.3.__ Number density profiles of water O atoms (solid lines), PEO O atoms (full circles), SDS chain terminal CH_3 groups (open circles), SDS S atoms (open triangles) and Na^+ counterions (asterisks) as obtained at 0 (top panel), 2 (second panel), 4 (third panel) and 6 μmol/m^2 (bottom panel) SDS at the surface of the aqueous phase. Profiles are averaged over the two interfaces present in the basic simulation box. The scale on the left refers to the water O atom density, and that on the right to the PEO and SDS atom densities.

Correspondingly, the main PEO density peak is located beneath the interface, and only a small shoulder of this peak is exhibited in the *X* region of intermediate water densities. Fig 4.3 shows that in the presence of even a relatively small amount of SDS at the water surface the PEO molecule behaves in a completely different way. In the presence of a small amount of SDS the majority of PEO segments is located at the surface of the aqueous phase (second panel of Fig. 4.3). This finding stresses that the low affinity of the PEO monomer units to the surface in the absence of SDS molecules cannot be explained by the saturation of the water surface by the polymer segments, as in the presence of SDS molecules the overall surface coverage is naturally higher than in their absence, still a much larger number of PEO monomer units are accommodated at the surface in the presence of a few SDS molecules. Further increase of the SDS surface density, however, leads to a competition between the SDS molecules and PEO monomer units for the surface positions, as reflected in the re-appearance of a bulk phase PEO density peak (third panel of Fig. 4.3). Finally, upon saturation of the adsorption layer by SDS molecules the majority of the PEO monomer units are departed from the water surface due to this competition (bottom panel of Fig. 4.3).

Finally, it should be noted that SDS molecules practically do not enter the bulk phase of the solution, even at the highest surface concentration considered. Thus, the bulk phase concentration of SDS, calculated in the 40 Å wide slab in the middle of the liquid phase, where the concentration of both the DS^- and Na^+ ions is already constant, resulted in always below 0.006 μM, which is well below the experimental value of the critical aggregation concentration (cac), falling between 0.9 and 1.3 μM depending on the molecular weight of PEO. [202] Thus, in accordance with experimental data, [203] the complete squeezing out of PEO from the surface by SDS occurs also well below the cac in the present simulations.

Partitioning of the PEO segments among the three regions of the system Having identified the truly interfacial PEO segments allows us to calculate percentage of the segments in the three different regions of the system. The dependence of the amount of PEO monomer units adsorbed at the surface on the SDS surface density is also seen from the partitioning of the PEO monomer units between the interface and the two bulk phases. The percentages of PEO segments in the different regions of the system at the different SDS concentrations is collected in Appendix B, Table 2.

In the SDS free system 73% of the PEO monomer units are found to be in the bulk aqueous phase, and only 26% of them is located right at the interface. However, even in the presence of 1 μmol/m^2 SDS at the water surface more than 80% of the PEO monomer units are found in surface positions, and the percentage of the bulk aqueous phase monomer units drops below 15%. The increase of the SDS surface density up to 4 μmol/m^2 leads to small changes in the partitioning of the

PEO segments. A slight decrease in the percentage of interfacial monomer units due to the increasing occupation of the surface sites by SDS molecules is evidenced. However, up to 3 μmol/m^2 SDS surface density the PEO monomer units departing from the interface enter rather the apolar than the aqueous phase. Further increase of the SDS surface density leads to the occupation of the vast majority of the surface positions by adsorbed SDS molecules, whom eventually squeeze out the PEO monomer units from the surface in a step by step manner. From 5 μmol/m^2 SDS surface density the vast majority of the PEO monomer units are again located in the bulk aqueous phase.

Thermodynamic driving force of the partition In the SDS-free system, where the vast majority of the monomer units are located inside the bulk liquid phase; and only 17% of them anchor the entire polymer to the surface, the observed partitioning of the polymer segments is a result of an interplay between entropic and energetic effects. Since the monomers in the vapor phase have no close contact neighbors, and the energy of their interactions with the rest of the system is expected to be relatively small in magnitude, the presence of the vapor phase polymer loops is clearly an entropic effect. (It should be noted that, as we have already seen, the traditional model of polymer adsorption usually disregards the presence of vapor phase loops (see Fig. 4.1), and assumes that the polymer segments are partitioned solely between the bulk liquid phase and the interface. The results of this study stress that this approach might be refined in this respect.) The presence of the weakly polar (-CH_2-O-CH_2-) monomer units at the boundary between the liquid and vapor phase is energetically clearly preferable to that of the highly polar, hydrogen-bonding water molecules, which is reflected also in the fact that the surface tension of the SDS-free system has turned out to be only 51.3 mN/m, i.e., almost the third of the value of 120.3 mN/m obtained for neat SPC water. Thus, the observed small percentage of polymer segments at the interface can be attributed to entropic effects. Indeed, the presence of consecutive PEO segments at the interface seriously restricts their conformational degrees of freedom, while there is no such restriction in the bulk liquid phase. Thus, while the intermolecular energy term favors that PEO segments stay at the interface (since, due to their weaker interactions with their neighbors they lose considerably less interaction energy by being at the interface than the water molecules), the conformational entropy of the PEO chain effectively prevents more consecutive monomer units from being simultaneously at the interface. The presence of SDS at the surface modifies the interplay of the above two factors substantially. The charged headgroup of the DS^- ions as well as the Na^+ counterions can strongly interact with the charge distribution of the PEO monomer units, giving rise to the internal energy decrease accompanying the adsorption of the segments. On the other hand, the apolar hydrocarbon chains of the SDS molecules can provide an environment of high conformational degree of freedom for the PEO chains at the interface.

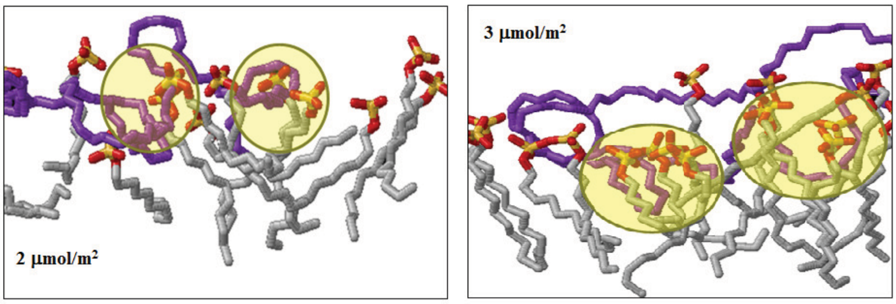

Figure 4.4. *Instantaneous equilibrium snapshots of parts of the interface of the systems containing 2 (top) and 3 μmol/m² (bottom) SDS at the surface of the aqueous phase, illustrating the formation of PEO/SDS complexes at the interface. Encircled are such apolar cushions formed by PEO/SDS surface complexes. The PEO chains and SDS O, C, and S atoms are marked by purple, red, gray, and yellow colors, respectively.*

In other words, similarly to the bulk phase solution, the neutral PEO chains and the DS^- ions can form stable polymer/surfactant complexes also at the interface, which provides an additional driving force for the adsorption of the polymer segments, and also for their increasing penetration of the to the apolar region of the SDS hydrocarbon chains. Such PEO/SDS surface complexes are illustrated in Figure 4.4, showing instantaneous equilibrium snapshots of part of the interface as taken from the simulations of the 2 and 3 μmol/m² SDS systems. The possible formation of PEO/SDS surface complexes is, however, limited to the SDS surface density range up to which the adsorbed SDS molecules leave enough unoccupied surface area for the adsorption of the PEO segments. At higher SDS surface concentrations, on the other hand, no such synergistic effect in the adsorption of the two components can be observed; instead, a real competition between the PEO monomer units and SDS molecules occurs for the available surface positions. In this competition the more surface active SDS molecules win, and the PEO segments are displaced from the surface. The obtained results also suggest that the complete departure of the entire PEO molecules from the surface occurs in a monomer unit-by-monomer unit manner, i.e., when all of its monomer units are squeezed out from the surface by the SDS molecules then the entire PEO molecule is departed from the surface. The observed dependence of the PEO adsorption on the SDS surface density is illustrated in Figure 4.5, showing instantaneous equilibrium snapshots of one of the two interfaces in the systems containing 2, 4 and 6 μmol/m² SDS at the surface.

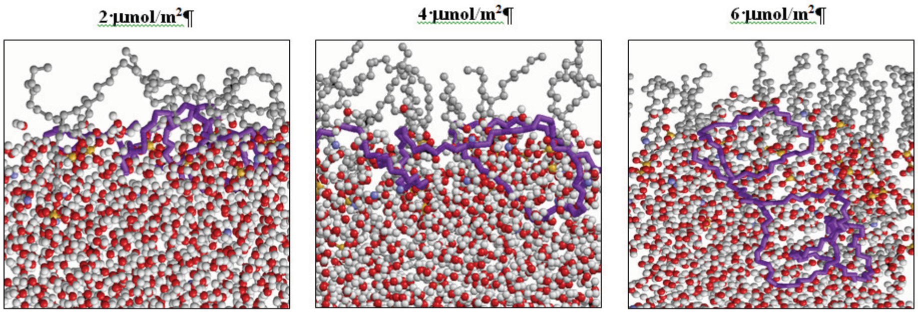

Figure 4.5. Instantaneous equilibrium snapshot of the interface of the systems containing 2 (top), 4 (middle) and 6 µmol/m² (bottom) SDS at the surface of the aqueous phase, as taken from the simulations. Colors are used in the same manner as in Fig.4.4.

4.2.1.3.2 Structural and orientational properties of the adsorbed layer

End group distances In order to characterize the overall structure of the PEO chains in the different systems we have calculated the distance of their two terminal CH_3 groups, D. The distribution of D in the different systems is shown in Figure 4.6, whereas its mean values are summarized in Appendix B Table 3. The average end-to-end distance of the PEO chains is considerably larger in the presence of SDS even at the lowest surface concentration considered than in the absence of adsorbed SDS molecules, while above this surface concentration no clear trend of $<D>$ with the SDS surface density can be observed. Further, the observed mean end group distance values are in every case considerably smaller than both the value of 35 Å predicted by the Flory theory in bulk liquid water, and the value of 33.1 Å obtained by simulating the same, 50 monomer units long PEO chain in bulk liquid water.

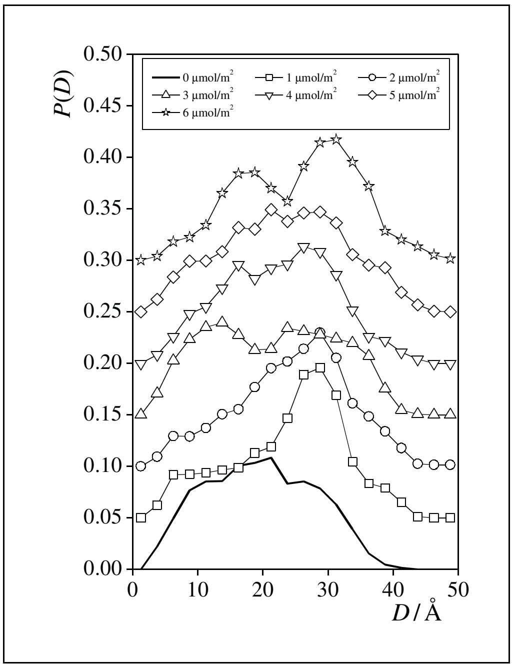

Figure 4.6. *Distribution of the distance D of the two terminal CH_3 groups of the PEO chains in the seven systems simulated. The lines and symbols corresponding to the different systems are the same as in Figure 1. The results corresponding to the systems containing 1, 2, 3, 4, 5, and 6 μmol/m^2 SDS at the surface of the aqueous phase are shifted by 0.05, 0.1, 0.15, 0.2, 0.25, and 0.3 units upwards along the vertical axis for clarity.*

These findings indicate *i*) that the interfacial binding restricts the conformational flexibility of the polymer chain; and *ii)* that the SDS molecules adsorbed at the interface provide an environment of greater conformational flexibility, and hence larger conformational entropy for the adsorbed PEO segments than the SDS free water surface. These results are in accordance with our previous observations, and confirm our conclusion that the enhanced adsorption of the PEO monomer units in the presence of SDS can largely be attributed to the larger conformational entropy of the polymer chains at the interface in the presence than in the absence of SDS molecules.

Roughness of the Aqueous Surface. The $\bar{d}(l)$ roughness curves of the seven different systems simulated are shown in Figure 4.7, whereas the ξ and a roughness parameters are summarized in Table 3 of Appendix B. As is seen, the increase of the SDS surface density clearly leads to the increasing roughness of the water surface both in terms of frequency and amplitude. This increasing corrugation of the aqueous surface can be explained by the decreasing surface tension, γ, of the system. Indeed, the surface tension values, collected also in Table 3 of Appendix B, decrease continuously with increasing SDS surface density. This finding indicates that the SDS molecules are more surface active than PEO, and explains the dominance of the former in the competition for surface positions in crowded mixed adsorption layers, which ultimately leads to the displacement of the entire PEO chains from the surface at high enough SDS surface densities. It should also be noted that the PEO molecule itself is also highly surface active, as seen from the fact that the surface tension of the SDS free system, i.e., 51.3 mN/m is already substantially lower than that of neat SPC water of 120.3 mN/m.

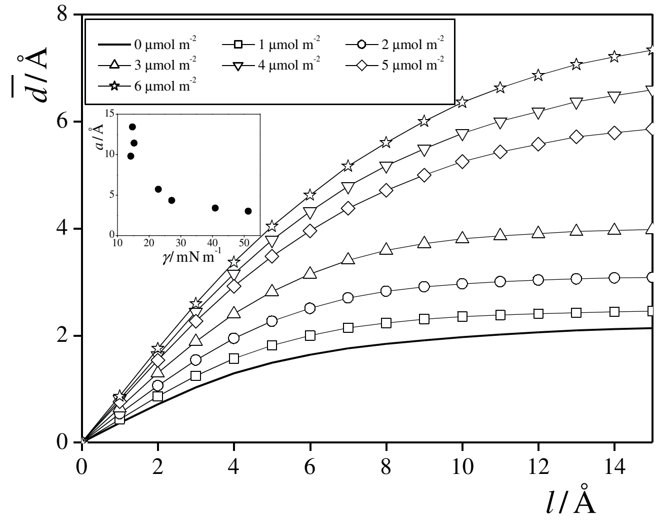

Figure 4.7. *Average normal distance of two surface points (i.e., their distance along the interface normal axis X) as a function of their lateral distance (i.e., their distance in the plane YZ of the interface) in the seven systems simulated. The inset shows the correlation between surface tension and the amplitude parameter of surface roughness.*

The decrease of the surface tension makes the free energy cost of increasing the water surface area through corrugation smaller, and thus leads to the observed increasing roughness of the water surface. The clear correlation between the surface tension of the system, γ, and the amplitude of its molecularly rough surface, a, is illustrated in the inset of Fig. 4.7. It should finally be noted that the increase of the surface roughness, i.e., the increase of the area of the intrinsic surface of the aqueous phase enables more SDS molecules and PEO monomer units to be accommodated at the surface, and hence extends the SDS surface density range in which no substantial squeezing out of the PEO monomer units from the surface occurs.

Structure of the SDS Adsorption Layer. The density distributions of the S atoms and chain terminal CH_3 groups of the DS^- ions as well as that of the Na^+ counterions along the macroscopic surface normal axis X are also included in Fig. 4.3. As is seen, in accordance with our previous observations, the DS^- ions are located almost exclusively at the water surface; no perceivable penetration of these ions into the bulk of the aqueous phase is observed even at the highest SDS surface density considered. The density peak of the CH_3 groups is located considerably, by 8 -15 Å farther from the aqueous phase than that of the S atoms, reflecting the overall outward orientation of the DS^- chains. The distance between the peak positions of these density distributions, δ_{SC} (see Table 3 of Appendix B) provides us with information about the average orientation of the DS^- ions at the surface. Thus, the continuous increase of δ_{SC} with increasing SDS surface density indicates the gradual turn of the DS^- ions from tilted to perpendicular orientation relative to the macroscopic plane of the interface. The density distributions of the Na^+ counterions follows that of the S atoms (being the centers of the negatively charged sulfate groups of the DS^- ions), although, due to the diffuse nature of the Na^+ counterion layer, it always extends noticeably deeper into the bulk aqueous phase than that of the S atoms.

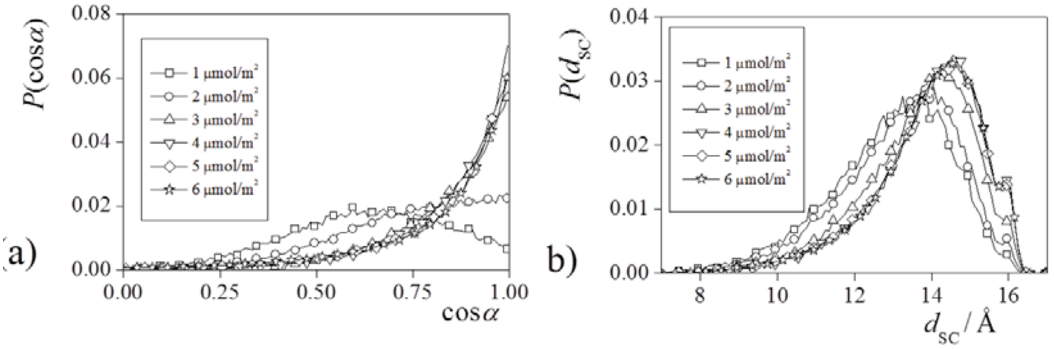

Figure 4.8. *a) Cosine distribution of the angle* α*, formed by the macroscopic interface normal vector, pointing from the aqueous to the apolar phase,* $\underline{X}$*, and the vector pointing along the* DS^- *chain from its S atom to the terminal* CH_3 *group; and b) distribution of the distance of the S atom and* CH_3 *group of the* DS^- *ions,* d_{SC}*, in the six SDS containing systems simulated.*

To investigate the structure of the adsorbed layer of the DS^- ions in more detail we have also calculated the cosine distribution of the angle α, formed by the macroscopic surface normal vector pointing from the aqueous to the apolar phase, $\underline{X}$, and the vector pointing along the DS^- chain from its S atom to the chain terminal CH_3 group. The distribution of the distance of the S atom and CH_3 group of the individual DS^- ions, d_{SC}, has also been calculated. The $P(\cos\alpha)$ and $P(d_{SC})$ distributions are shown in Figure 4.8 as obtained in the different SDS containing systems simulated. The $P(d_{SC})$ distributions obtained in the different systems are rather similar to each other, indicating that changes in the SDS surface density leave the conformation of the DS- ions practically unaffected. It is also seen that the DS^- ions prefer to adopt rather elongated conformations. Thus, the $P(d_{SC})$ distributions have their main peak around 14 Å, followed by a shoulder at about 16 Å in the systems of high SDS surface densities. This shoulder corresponds to the DS^- ions of all-*trans* conformation, whereas the main, broad peak of the $P(d_{SC})$ distributions is given by DS^- ions having one *gauche* aligned dihedral. The few DS^- ions having more than one dihedrals in *gauche* alignment contribute to the long tail of this peak at low distances.

Unlike their conformation, the orientation of the DS^- chains depends strongly on the SDS surface density. Thus, in the 1 μmol/m^2 system the $P(\cos\alpha)$ distribution is rather broad, covering almost the entire $\cos\alpha$ range from 0 to 1, and has its peak around the $\cos\alpha$ value of 0.6. In this system the orientation of the DS$^-$ ions is rather disordered, and the most probable orientation corresponds to the tilt angle of about 55° relative to the surface normal axis. The orientational order of the DS$^-$ ions is still rather weak in the 2 μmol/m^2 system, as the obtained $P(\cos\alpha)$ distribution is still quite broad, however, in this system the most probable orientation is already perpendicular to the macroscopic plane of the interface. This perpendicular orientation becomes then strongly preferred in the systems of higher SDS surface densities, which are characterized by rather strongly ordered SDS adsorption layers. Thus, in these systems about 20% and 50% of the DS$^-$ ions have a tilt angle smaller than 15° and 30°, respectively, relative to the macroscopic surface normal axis. The increasing preference of the DS$^-$ ions to adopt orientations perpendicular to the macroscopic plane of the interface with their increasing surface density had been observed previously in adsorption layer of various non-ionic surfactants, and can be explained by the decreasing surface area available for the individual molecules.

4.2.1.3.3 Adsorption dynamics

Survival probabilities In order to investigate the dynamics of the process of interfacial water molecules and PEO monomer units leaving the interface and entering one of the bulk phases we have calculated the survival probability $L(t)$ of these species at the interface. The $L(t)$ survival probabilities of the interfacial water molecules and PEO monomer units are shown in Figure 4.9 as calculated in the simulated systems. As is seen, PEO monomer units stay, in general, considerably longer at the interface than water molecules. This difference can be explained by the hindrance of mobility of the PEO monomer units due to the constraints imposed by the chemical links to their neighboring segments along the polymer chain. It is also seen that, in general, the presence of SDS at the surface slows down the dynamics of exchange of the water molecules and PEO monomer units between the interface and the bulk phases.

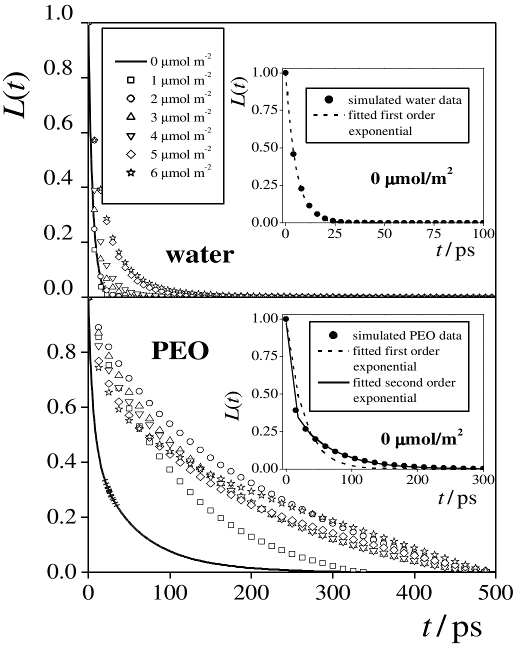

Figure 4.9. *Survival probability of the water molecules (top) and PEO monomer units (bottom) in the surface layer of the seven systems simulated. The insets illustrate, on the example of the SDS free system, that the water survival probability data (full circles, upper inset) can be fitted by a single exponential function (dashed line, upper inset), whilst the survival probability of the PEO monomer units (full circles, lower inset) cannot be fitted by such an exponential (dashed line, lower inset), only by the sum of two such exponential functions (solid line, lower inset).*

To describe this process in a more quantitative manner we have fitted the exponentially decaying function exp($-t/\tau$) to the obtained $L(t)$ data, just in order to find that while the interfacial survival probabilities of the water molecules can be well fitted by a single exponential function, the fitting of that of the PEO monomer units requires the use of the sum of at least two such exponential functions (see the insets of Fig. 4.9). This interesting feature implies that whereas a water molecule leaves the interface following first order kinetics with the mean residence time value of τ, PEO monomer units can depart from the interface in two different ways, both of described by first order kinetics, having the respective characteristic times of τ_1 and τ_2. These two ways of leaving the interface can be identified as departing towards the bulk aqueous and to the bulk apolar phase, respectively. (Since water molecules have never been found to enter the apolar phase in our simulations, they can only leave the interface in one way, towards the bulk aqueous phase, in accordance with the observed fact that the water survival probability function can always be fitted by one single exponential.)

The τ (water) as well as the τ_1 and τ_2 (PEO) residence times corresponding to these processes are summarized in Appendix B Table 3. Assuming that the dominant process of the interfacial PEO monomer units is always the departure towards the aqueous rather than to the apolar phase the τ_1 and τ_2 values are associated with these processes, respectively. The appearance of a small amount of SDS at the surface facilitates the exchange of the PEO monomer units between the interface and the apolar phase. This result supports our previous finding about the increase of the conformational entropy of the PEO chains in the presence of SDS as well as on the formation of stable interfacial polymer/surfactant complexes between the PEO chain and DS^- ions. However, with further increasing SDS surface density the apolar adsorption layer becomes increasingly crowded by the DS^- ions, which leads to a considerable slowdown of this exchange process, as penetration of the PEO monomer units into this layer becomes increasingly difficult.

It is also seen that the presence of SDS at the surface slows down the exchange processes between the interface and the bulk aqueous phase, and this effect is considerably more pronounced for the PEO monomer units than for water. The SDS induced hindrance of mobility of these polar species can, at least partly be explained by their strong electrostatic interaction with the ionic sulfate group of the DS^- ions and with the Na^+ counterions in the interfacial region. In the case of the PEO monomer units the slowdown of this exchange process is also related to their increased affinity to the interface due to the increasing conformational flexibility of the PEO chain in the presence of SDS, as discussed in detail in the previous sub-sections.

4.2.1.3.4 Energetic results

To shed light on the energetic background of the observed dependence of the adsorption of PEO at the water surface on the SDS surface density, we have calculated the distribution of the interaction energy (U_b) of the PEO monomer units located in the three different regions with the rest of the system for each simulated system. (It should be noted that, apart from the energy of the two chemical bonds linking the given monomer unit to its neighbors in the polymer chain, this interaction energy is simply the binding energy of the given monomer unit, i.e., the energy that is required to move this unit at infinite distance from the system.) In addition to the interaction energy of the given PEO monomer unit with the rest of the system we have also calculated the distribution of its contributions coming from the interactions with the water molecules, U_b^{wat}, and from that with the other solutes (i.e., other PEO segments, DS^- ions and Na^+ counterions) present in the system, U_b^{sol}. Since we are interested here in the effect of the non-bonding interactions, the contribution of the neighboring (i.e., chemically linked) PEO monomer units to U_b and U_b^{sol} are disregarded in this analysis.

The $P(U_b)$, $P(U_b^{wat})$ and $P(U_b^{sol})$ distributions of the PEO segments being in the aqueous phase, at the interface and in the apolar phase are shown in Figure 4.10 as obtained at 0, 2, 4 and 6 μmol/m^2 SDS surface densities. As is seen, in the SDS free system the solute contribution to U_b is relatively small both in the aqueous phase and at the interface. The $P(U_b^{sol})$ distribution has a peak around -10 kJ/mol in every case, whereas the $P(U_b^{wat})$ distributions exhibit their peak around -30 – -40 kJ/mol, which extends down to -50 – -60 kJ/mol in the aqueous phase and at the interface, indicating that the PEO monomer units form one or two hydrogen bonds with the neighboring water molecules in both of these regions. In the apolar phase the $P(U_b^{wat})$ distribution exhibits a sharp peak around zero, reflecting the fact that in this region the PEO monomer units do not have close water neighbors.

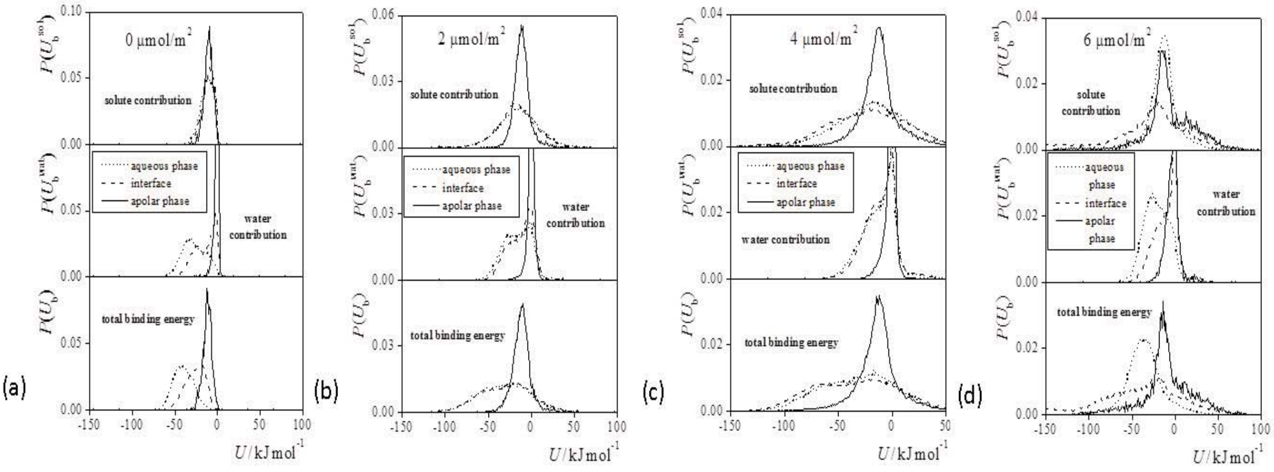

Figure 4.10. *Distribution of the total interaction energy of the PEO monomer units with the rest of the system (bottom panels) as well as of its contributions coming from the interaction with the water molecules (middle panels) and with the SDS molecules and other PEO units (top panels) in the bulk aqueous phase (dotted lines), at the interface (dashed lines) and in the apolar phase (solid lines) of the systems containing (a) 0, (b) 2, (c) 4, and (d) 6 μmol/m^2 SDS at the surface of the aqueous phase.*

The $P(U_b^{wat})$ distributions do not change considerably upon addition of SDS to the system, the only effect of the presence of SDS on these distributions is that in the case of the interfacial PEO monomer units a peak evolves around zero with increasing SDS surface density, and becomes the dominant feature of the $P(U_b^{wat})$ distribution at Γ_{SDS} = 4 μmol/m^2. The evolution of this peak reflects the fact that when the adsorption layer gets increasingly crowded with SDS molecules an increasing fraction of the interfacial PEO monomer units loses contact with the water molecules.

Contrary to $P(U_{\mathrm{b}}^{\mathrm{wat}})$, the distribution of the solute contribution $P(U_{\mathrm{b}}^{\mathrm{sol}})$ shows a marked dependence on the SDS surface density. Namely, the peak of this distributions gets visible broader upon the addition of SDS molecules, while its peak position remains practically intact, around -10 kJ/mol. This effect is particularly pronounced in the aqueous phase and at the interface, and can be explained by the strong electrostatic interaction of the polar PEO monomer units with the charged sulfate group of the DS^- ions as well as with the Na^+ counterions. Further, the mean value of the distribution corresponding to the interfacial PEO monomer units decreases only moderately with increasing SDS surface density, being -11.1, -16.8, -23.4 and -31.9 kJ/mol in the systems of 0, 2, 4 and 6 µmol/m^2 SDS surface densities, respectively. This decrease of the mean interaction energy of an interfacial PEO monomer unit with the other solute molecules has the same origin as the increase of the average interaction energy of these monomer units with water, namely that in a more crowded adsorption layer an interfacial PEO monomer unit has more Na^+ and DS^- neighbors. Further, these two effects largely compensate each other, thus the total gain of the mean interaction energy is always below 10 kJ/mol. This result clearly confirms our previous finding, already supported by structural and dynamical results that the enhanced surface affinity of the PEO monomer units in the presence of SDS at moderate surface densities can only partly be explained by the decrease of the internal energy of the system due to the strong electrostatic interaction between these polar monomer units and the charged groups of SDS, and thus the main reason of this enhanced surface affinity should be the increase of the conformational entropy of the PEO chains in the environment provided by the adsorbed layer of SDS molecules.

4.2.1.4 Summary

The atomistic scale treatment of the polymers and polymer-surfactant mixtures at the surface of their aqueous phase has allowed us to draw conclusions concerning the mechanism of adsorption and the underlying thermodynamic driving forces.

The study of the neat PEO adsorption layer at the water surface has showed that adsorption in this case is determined by two main competitive processes. The first of these processes, namely the solvation of the segments is driven by the conformational entropy change. In other words, the larger the number of hydrated monomer units is, the larger the number of the possible conformations will be. The other process is the adsorption of the surface active monomer segments at the interface, which decreases the interfacial excess energy. According to the already existing models of polymer adsorption, these two driving forces lead to the distribution of the monomer segments between the interface and the bulk liquid phase, which corresponds to an optimal combination of these two driving processes. Our simulations have shed light on the fact that such an optimal combination leads to the attachment of the polymer to the interface by very short segments, whereas the majority of monomer units is arranged in loops in the bulk phase. So far our results correspond to the classical picture, however we have also found a slight but noticeable extent of penetration of the monomer units into the vapor phase, which has never been included in any of the existing models. Obviously, this is again an energetically unfavorable situation for the individual monomer units, but it leads to an increase in the conformational entropy. Further, it has to be also mentioned that only about 1% of the monomer units are, on average, in the vapor phase, their lifetime in there is rather short (being, on average, 3.1 ps), and these vapor phase loops, being very short remain relatively close to the water surface and thus can partially maintain their interactions with water molecules.

The results obtained for the mixed adsorpion layer reveal that the squeezing out of the surface active polymer from the interface by increasing the amount of the surfactant occurs by a rather complex mechanism. Even if we could see that PEO in the absence of SDS is anchored to the surface by 20-25% of its monomer units, this behavior is by no means related to a possible saturation of the interface, as the presence of a small amount of SDS brings almost the entire PEO molecule to the surface, as in this case about 80% of the PEO monomer units are located right at the boundary of the aqueous and apolar phases. This synergistic effect of SDS on the PEO adsorption can be explained by the interplay of the electrostatic attraction between the charged groups of SDS and the charge distribution of the moderately polar PEO monomer units, and by the increasing conformational flexibility, and hence the increase of the conformational entropy of the polymer chains in the presence of SDS. From these two factors we have found the second one to be more important. This view is supported by the findings that the average end-to-end distance of the PEO chains is noticeably larger, which means it is closer to the equilibrium bulk solution phase value corresponding to the maximum conformational entropy, in the presence than in the absence of SDS. On the other hand, the mean interfacial residence time of the PEO monomer units increases much more than that of the water molecules upon adding SDS to the system; and the addition of SDS to the system leads only to a small decrease of the average interaction energy of the interfacial PEO monomer units. Further, effective attraction of the PEO chains to the surface by the SDS molecules through the increase of their conformational entropy implies the formation of similar polymer/surfactant complexes in the mixed adsorption layers of moderate SDS content than what are well known to exist in the bulk phase of their solution. However, further increase of the SDS surface density gives rise to the competition of the SDS molecules and PEO monomer units for the surface positions, and at large SDS surface densities the more surface active SDS gradually squeezes out the PEO molecules from the surface. This squeezing out occurs in a monomer unit-by-monomer unit manner, i.e., when the last monomer unit of a PEO molecule is replaced by a DS^- ion at the surface the entire PEO molecule is departed from the surface to the bulk phase of the solution.

The results of this study stress the complex nature of polymer/surfactant interactions even at the surface of their solution, and point out the important role of the interplay of energetic and entropic terms in determining the actual behavior of these important and complicated systems.

4.2.2 Calculation of the free energy profile of ions through the water/1,2-dichloroethane interface [8,9]

4.2.2.1 Introduction

The main goal of this study is to test the novel method we have proposed for calculating the free energy profile of ions with respect to the real intrinsic interface. Moreover we present the free energy profile of the transfer of the thiocyanate ion through the water/1,2-dichloroethane interface in order to shed light on the affinity of this ions to the surface, and thus to get a deeper insight to the molecular reasons underlying the surface activity of ions. The question of the co-extraction of the hydration shell and the possible orientational changes induced in the ion by the vicinity of the interface are also addressed.

The method we have proposed is to the best of our knowledge the first computationally feasible way of calculating the solvation free energy profile of a single penetrant particle across fluid interfaces with respect to the real instantaneous intrinsic interface. This new protocol, which has been described in details in Chapter 2.8.2. has been and applied for the calculation of the intrinsic solvation free energy profile of a Cl^- ion across the water/1,2-dichloroethane (DCE) liquid/liquid interface. The choice of this system has been dictated by the fact that it is a frequently studied model in the literature, similar investigations targeting the non-intrinsic free energy profile have been reported previously several times, [204,205,206] and hence the obtained intrinsic free energy profile can readily be compared to the global, non-intrinsic one.

Prior to the development of the new method the free energy profile of the penetration of the SCN^- ion has also been calculated by the classical way of reconstructing the free energy profile from constrained force simulations. The choice of thiocyanate ion was dictated by the importance of this ion is outstanding in various fields of chemistry. It plays a considerable role in essential biochemical processes, such as the biosynthesis of hypothiocyanite, the lack of which is proven to cause cystic fibrosis.[207] On the other hand, detailed studies of this ion by means of electrochemical experimental techniques (cronoamperometry as well as cyclic voltammetry) dates back to the middle of the last century.[208] Since that time this ion has attracted an ever increasing interest. Thus, the understanding of the structural and the thermodynamic changes that accompany the transfer of the SCN^- ion through a water/organic phase boundary is undoubtedly of crucial interest.

4.2.2.2 Computational details

Molecular dynamics simulations of the water/DCE liquid/liquid interfacial system containing one single thiocyanate (SCN^-) or chloride (Cl^-) ion at different positions have been performed on the canonical (N,V,T) ensemble at 298 K using the GROMACS simulation program package.[109] The lengths of the X, Y and Z edges of the rectangular basic simulation box (X being perpendicular to the macroscopic plane of the interface) have been 104, 50 and 50 Å respectively, and the system consisted of 4000 water and 1014 DCE molecules.

Water molecules have been described by the TIP4P model,[209] whereas standard OPLS potential parameters[63] have been used for the SCN^- and the Cl^- ion and for the DCE molecule[115]. The fractional charges corresponding to the DCE molecule have been taken from the work of Benjamin.[210] All bond lengths and bond angles have been kept fixed in the simulations, while torsional rotation of the DCE molecule around its C-C bond has been allowed. The CH_2 groups of the DCE molecules have been treated as united atoms. The total potential energy of the systems has been assumed to be the sum of the pair interaction energies of all molecule pairs. The interaction energy of two molecules has been calculated as the sum of the Lennard-Jones and Coulomb interactions. The Lennard-Jones distance and energy parameters (σ and ε, respectively) of the interacting atoms have been combined according to the Lorentz-Berthelot rule.[14] The Lennard-Jones parameters as well as the fractional charges, q, of the different interaction sites are collected in Appendix A, Table 2. Bond lengths and bond angles of the water molecules; and those of the DCE molecules and SCN^- ion have been kept unchanged by means of the SETTLE[111] and LINCS[112] algorithms, respectively. All interactions have been truncated to zero beyond the center-center cut-off distance of 9.0 Å. The long range part of the electrostatic interactions has been accounted for using the particle mesh Ewald (PME) method[16] with a real space cutoff of 9.0 Å, a mesh grid of 1.2 Å and a spline order of 4. Analytical tail correction has been applied. To maintain electroneutrality of the system simulated, a uniform positive charge distribution compensating the net charge of the SCN$^-$ or the Cl$^-$ ion has been added beyond the cut-off sphere of the charged particle, and its effect has also been accounted for by means of the PME method.[16] To test the appropriateness of the cut-off value of 9.0 Å used here, we have repeated six simulations with different positions of the SCN$^-$ ion, corresponding to different regions of the system, using a considerably larger interaction cut-off value, i.e., 12.0 Å, but, besides the statistical noise, no difference between the runs performed with different cut-off values has been observed.

To obtain the sample configurations on which our intrinsic and non-intrinsic analyzes were to be performed, we have used the widespread Constraint Force algorithm. Practically, we have carried out a series of molecular dynamics simulations on the canonical (N,V,T) ensemble with the ions fixed at different positions, separated from each other by 1Å along the interface normal axis X of the water/1,2-DCE system, which has been previously equilibrated without the ions. With a series of these simulations we have modeled the transfer of the ion from the bulk aqueous phase to the organic phase in quasi-equilibrium steps. The force required to keep the position of the ions unchanged with respect to the global coordinate frame defined by the basic vectors of the simulation box has been recorded in each single step of every simulation. After proper energy minimization of the starting configuration created by displacing the Cl$^-$ or the SCN$^-$ ion by 0.1 nm in the X direction from its final position in the previous run, the system has been equilibrated for 100 ps with the constraining force exerted on the ion. After equilibration, an additional 500 ps long production run has been carried out, during which the magnitude of the X component of the constraining force, $F_X(t)$, has been recorded as a function of time for every time step. Simultaneously, equilibrium sample configurations, separated by 5 ps long trajectories from each other, have been saved for the intrinsic analysis. For the non-intrinsic analysis the forces have been averaged over time and integrated to yield the potential of mean force, whereas the novel intrinsic analysis was performed as described in Chapter 2.8.2.

4.2.2.3 Results concerning the thiocyanate ion

4.2.2.3.1 Non-intrinsic free energy profile

The solvation free energy profile of the SCN$^-$ ion obtained from the simulations is shown in Figure 4.11. Error bars have been estimated by the method of block averages. For reference, the mass density profile of water and DCE are also indicated. The shape of the obtained profile indicates that the energetic changes accompanying the transfer of the SCN$^-$ ion from the aqueous to the organic phase follow a complex scheme.

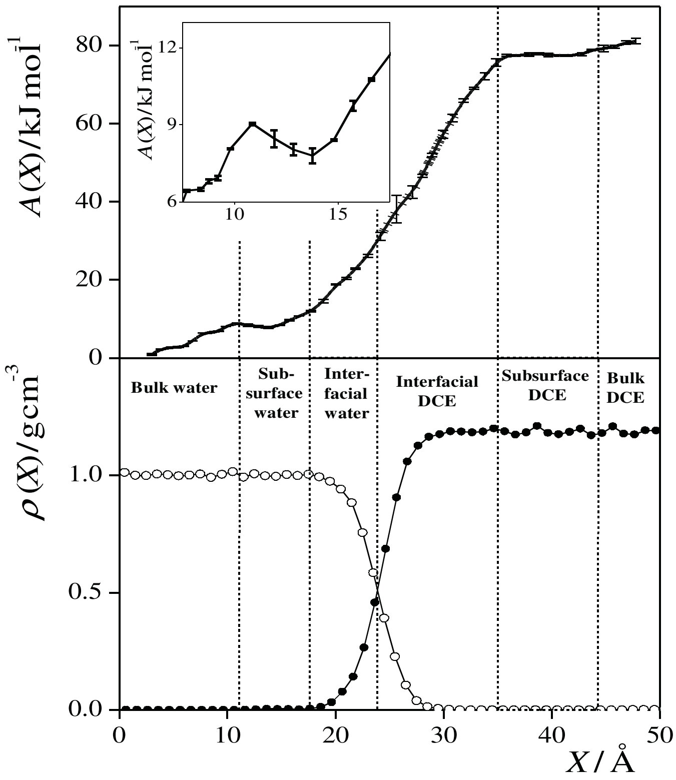

Figure 4.11. Solvation free energy profile of the SCN$^-$ ion across the water/DCE interface (top panel). Error bars estimated by the method of block averages are also shown. For reference, the mass density profiles of the water (open circles) and DCE molecules (filled circles), obtained in the ion free system[60] are also shown (bottom panel). The dashed vertical lines show the division of the system into six separate regions (see the text). The inset shows the local minimum of the free energy profile at the subsurface water region on a magnified scale

Thus, on approaching the interface from the bulk aqueous phase a slight increase of the free energy, culminating in a local maximum is seen. Since the solvation free energy of the SCN$^-$ ion inside a bulk liquid phase has to be position independent, this slight increase, typically seen in free energy profile calculations of ions, is clearly an artifact, related to the presence of two phases of markedly different dielectric constant under periodic boundary conditions. If the ion is embedded in one of the bulk phases, it experiences being in a slit of different dielectric constant than the environment behind the slit. The presence of the two dielectric boundaries results in a (non-physical) net force on the ion, which decreases upon approaching the middle of the phase, and vanishes only in the middle of the phase, i.e., at equal distance from the two boundaries. The presence of this artificial force results in the slight, albeit noticeable, non-physical decrease of the free energy profile in the bulk aqueous phase.

More importantly, the free energy profile shows a small but clear minimum in the subsurface region of water, around the *X* value of 15 Å. The ITIM analysis performed the aqueous and the DCE phase on the ion free system has revealed that this slight local minimum is located roughly at the position of the fourth molecular layer of water. Interestingly, the furthermost point to which the DCE molecules can penetrate into the aqueous phase coincides with the outer end of the region where the free energy minimum is observed. This suggests that, presumably due to the presence of the organic molecules, the region where the two phases are in direct contact with each other is a thermodynamically less favorable environment for the SCN^- ion than the subsurface water layer. The minimum in the free energy profile indicates enhanced ion concentration just beneath the interface, slightly pushed back from there to the bulk aqueous phase by the presence of the opposite phase. Similar behavior has been observed both experimentally and by computer simulations for the free surface of several ionic solutions, with the difference that in these cases the enhanced concentration region was located right at the interface.

The minimum in the subsurface water layer is followed by a strictly monotonically increasing part of the free energy profile, reflecting the fact that the SCN^- ion stays preferentially in the aqueous rather than in the organic phase. The free energy range covered by this increase (i.e., the solvation free energy difference of the SCN^- ion between the two phases) is found to be roughly 70 kJ/mol. The interfacial increase of the profile is followed by another plateau in the subsurface region of the DCE phase. According to ITIM analysis results of the ion-free system, the position of this plateau region again coincides roughly with that of the fourth molecular layer beneath the surface. Finally, the profile shows a slightly increasing part in the bulk DCE phase, the slope of this increase being noticeably smaller than that in the bulk aqueous phase, in accordance with the considerably lower polarity of DCE relative to water.

It should finally be noted that the plateau region of the profile in the subsurface DCE phase, contrary to that in water, is located clearly beyond the point up to which the molecules of the other phase can penetrate in the absence of an ion. The region of the steep free energy increase at the interface ranges beyond the point of noticeable water density further into the bulk organic phase, where finally it reaches its plateau. This behavior can be explained by the possible formation of a water finger around the SCN^- ion upon penetrating the organic phase, and by the co-extraction of at least a part of the ion's first hydration shell. This well-known phenomenon, observed also in a number of studies has, to our knowledge, scarcely been quantified by theoretical methods.

4.2.2.3.2 Properties of the SCN^- ion in different environments.

To characterize the hydration and orientation of the SCN^- ion in different environments we have divided the system into six separate regions according to the behavior of the obtained free energy profile. The division of the system into these six separate regions is shown in the bottom panel of Figure 4.11.

Hydration Properties. To investigate the hydration of the SCN^- ion we have calculated the pair correlation functions of all the three atoms constituting the ion with the water oxygen atoms in six distinguished positions representative of the six separate regions of the system. The $g(r)$ functions obtained in the two bulk and interfacial regions are shown in Figure 4.12. (The pair correlation functions obtained in the two subsurface regions did not differ considerably from those in the respective bulk regions, thus they are omitted from the figure.) As is seen, the obtained ion-water $g(r)$ functions preserve their main features observed in the bulk aqueous phase, irrespective of which region the ion is situated in. In particular, the height and position of the first peak seems to be insensitive to the region where the ion is located in every case. This finding suggests that the SCN^- ion indeed retains at least its first hydration shell upon entering to the DCE phase.

Having calculated the area under the first peak for each $g(r)$ function we can obtain a rough, semi-quantitative estimate of the hydration number of the SCN^- ion, N_{hyd}, by simply adding up the partial hydration numbers n_{hyd} of the S, the C and the N atoms, the latter simply being the coordination number of the water oxygens around the given atom up to the first minimum position of the corresponding $g(r)$ function. (We are aware of the fact that possible overlaps of the atomic hydration shells may introduce some error in this calculation, however, it seems reasonable to assume that the magnitude of this error is roughly the same in every case.) The hydration numbers calculated this way in the different regions of the system as well as the contributions of the S, C and N atoms to N_{hyd} are collected in Appendix B, Table 4. This table indicates that at the vicinity of the interface, regardless of which side of it the ion is situated, the total hydration number decreases by about 10-15% relative to the value obtained in the bulk aqueous phase, however, it gradually retains this value as the ion approaches the bulk DCE phase. Examining the atomic contributions in detail it is seen that in every region at least half of the first shell water molecules are located around the central carbon atom. Upon approaching the interfacial regions we encounter the decrease of all atomic contributions, however, some differences can be observed concerning the extent of dehydration, as seen from Table 4 of Appendix B Thus, the dehydration of the C and S atoms occurs simultaneously. After a smooth decrease, both atomic hydration numbers assume a minimal value in the interfacial region of the organic phase. The interfacial dehydration of the N atom is, however, somewhat different in the sense that, even if its hydration number is minimal in the same region, dehydration is not continuous, moreover, a maximum of it is seen right at the aqueous side of the interface. This slight rearrangement of the hydration shell at the interface suggests that the vicinity of the interface (and that of a phase of markedly different polarity) probably has an effect of enforcing a preferential orientation on the SCN$^-$ ion.

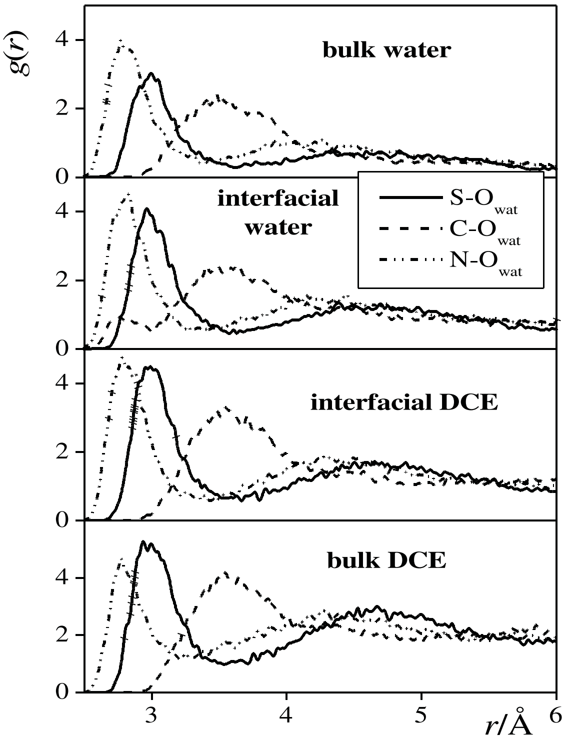

Figure 4.12. *Partial pair correlation functions of the S (solid lines), C (dashed lines) and N atom (dash-dot-dotted lines) of the SCN$^-$ ion and the water oxygens, as obtained in the bulk water (top panel), interfacial water (second panel), interfacial DCE (third panel), and bulk DCE (bottom panel) regions of the system.*

Orientation of the penetrant ion To further investigate this point we have calculated the cosine distribution of the angle γ, formed by the vector pointing along the SCN$^-$ ion from its S to N atom and the interface normal vector pointing from the organic to the aqueous phase, $\underline{X}$, in the six separate regions of the system. The obtained cosine distributions together with a chart illustrating the definition of the angle γ are shown in Figure 4.13.

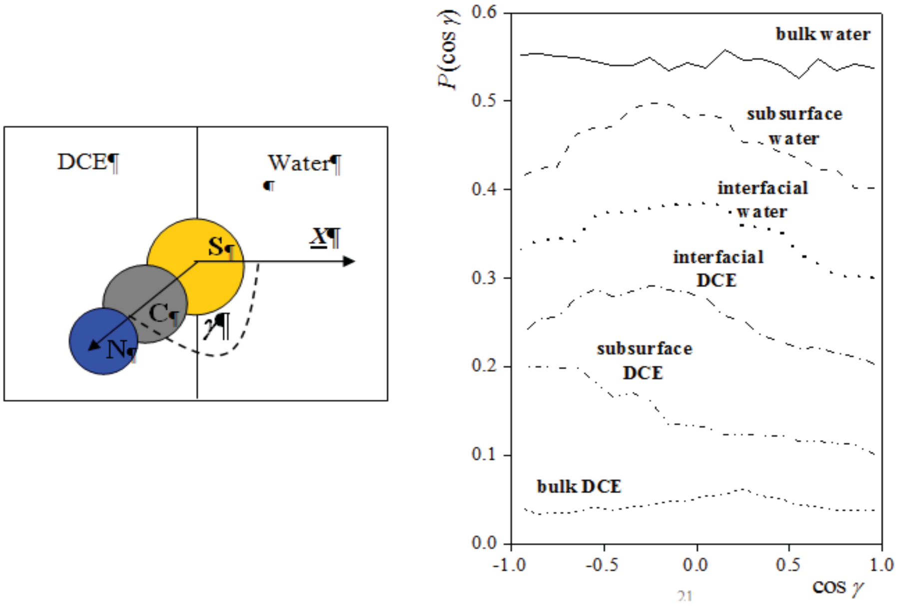

Figure 4.13. *Chart illustrating the definition of the angle γ characterizing the interfacial orientation of the SCN^- ion (left); and cosine distribution of the angle γ as obtained in the six different regions of the system (right). The results corresponding to the bulk water (solid line), subsurface water (dashed line), interfacial water (dotted line), interfacial DCE (dash-dotted line), subsurface DCE (dash-dot-dotted line), and bulk DCE (short dashed line) regions of the system are shifted by 0.5, 0.4, 0.3, 0.2, 0.1 and 0 units, respectively, for clarity.*

As is expected, no clear orientational preference of the ion is seen in any of the two bulk liquid phases. Upon approaching the DCE phase the SCN^- ion adopts a preferred alignment in which it points with the N atom to the organic and with the S atom to the aqueous phase. In the subsurface water region this preferred orientation is rather strongly tilted, it declines from the plane of the interface by only about 10°. However, as the ion gets closer to the DCE phase its preferred orientation becomes gradually less tilted, and eventually in the subsurface DCE region it becomes perpendicular to the interface, as seen from the gradual shift of the peak of the $P(\cos\gamma)$ distribution down to -1. Obviously, this orientational preference is not preserved when the ion penetrates into the bulk region of the DCE phase.

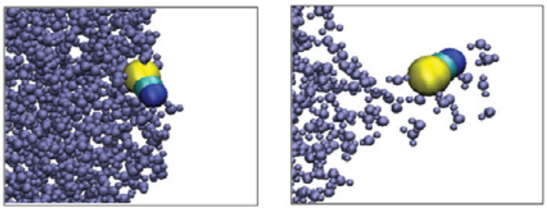

Figure 4.14 *Instantaneous snapshots illustrating the interfacial orientation of the SCN^- ion and the co-extraction of its first hydration shell upon entering to the organic phase. Water molecules are shown by grey color; the S, C and N atoms of the SCN^- ion are represented by a yellow, light blue and dark blue sphere, respectively. DCE molecules are omitted from the figure for clarity*

The observed orientational preferences are related to the considerably larger size of the S than of the N atom. Namely, when the SCN^- ion is located at the boundary of the two phases the free energy cost of bringing the first hydration shell water molecules of the small N atom to the organic side of the interface is clearly smaller than that of the large S atom. Further, the gradual decrease of the tilt angle of the preferred orientation is also related to the fact that the water molecules hydrating the large S atom remain at the aqueous side of the interface until the entire ion (together with its first hydration shell) is completely immersed in the DCE phase. The above interfacial orientational preferences of the SCN^- ion as well as the observed co-extraction of its first hydration shell are illustrated in Figure 4.14, showing two instantaneous snapshots taken out from the simulations in which the position of the SCN^- ion was fixed close to the boundary of the two phases.

4.2.2.4 Results concerning the Cl^- ion

4.2.2.4.1 Non-intrinsic free energy profiles

According to the non-intrinsic solvation free energy profile obtained from our simulations, the free energy difference between the bulk aqueous and the bulk organic phase is about 55 kJ/mol (12 kcal/mol). This value agrees sufficiently well with the results of previous computational studies. The profile corresponding to the water/DCE trajectory is shown in Fig. 4.15. together with the global mass density profiles of the aqueous and the organic phase, and those of the first three ITIM layers of both phases, as obtained for the ion-free case. The complete solvation free energy profile describing the transfer of the ion from the aqueous to the organic phase, interpreted thus in terms of the density profile of the system, provides us with more detailed information about the mechanism of the transfer. As is seen in Figure 4.15, the free energy profile of the transfer of a chloride ion from the aqueous to the organic phase can be divided into three main regions; namely, a more or less constant part in the bulk aqueous phase (region I.) a smoothly increasing part beginning in the subsurface region of the aqueous phase (region II.) which eventually turns smoothly into a plateau in the subsurface and bulk regions of the organic phase (region I). Region I., where the free energy profile takes values around zero, corresponds to the ion being dissolved in the bulk aqueous phase, where the opposite phase is far enough to have a negligible effect on the forces acting on the ion.

We should note here that, as opposed to the free energy profile obtained previously for the transfer of thiocyanate (SCN^-) ion through the same interface no significant drift of the free energy is observed in this region. The reason why in case of the chloride ion this effect is practically invisible in the non-intrinsic profile lies probably in the fact that the electric field of this nonpolarizable model of a small spherical charged particle has a spherical symmetry and obviously the ion rotates freely in its cavity, thus the effect of being situated between two different dielectric boundaries is averaged out. Region II., that is the smoothly and monotonically increasing part of the profile begins in the subsurface region of the aqueous phase, spans through the interfacial regions of both the aqueous and the organic phases and ends in the subsurface region of the organic phase. The increase in the free energy is due to the more and more repulsive forces that the ion experiences upon approaching the interface, which is related to the actual insolubility of the chloride ion in DCE. This part of the profile turns smoothly, without exhibiting any kind of extrema, into the plateau of region III, where the average free energy value of 55 kJ/mol corresponds to the free energy of solvation of the hydrated ion in 1,2-dichloroethane.

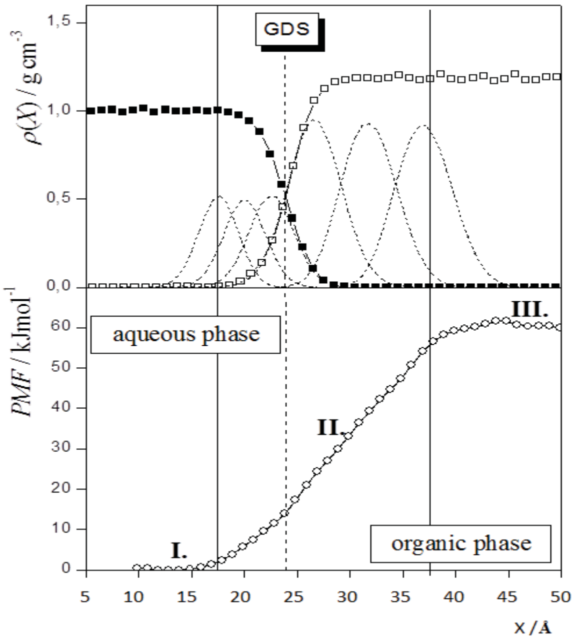

Figure 4.15 *Non-intrinsic free energy profile of the Cl- ion through the water/1,2-DCE interface (bottom panel). For reference the mass density profiles of the ion-free water and DCE molecules in the entire system and the first three-three ITIM layers are also shown (top panel)*

4.2.2.4.2 Intrinsic free energy profiles

Comparison of the intrinsic and non-intrinsic profiles We have reconstructed the intrinsic free energy profile of the chloride ion through the water/1,2-dichloroethane interface by each possible combination of the sub-procedures described in the previous section. Regardless of the applied methods, we have found significant differences in the smoothness of the intrinsic and non-intrinsic curves. As it has been discussed in the previous section, the non-intrinsic profile increases strictly monotonically in the interfacial region and reaches a plateau corresponding to the free energy of solvation in the bulk organic phase, while both of the intrinsic curves exhibit clear extrema, moreover even in the region of monotonic increase abrupt changes of the steepness occur, and a under-sampled interval is also observed. On the other hand, the intrinsic free energy profiles obtained by the Voronoi analysis and the triangular interpolation are very similar to each other, although the curve obtained by the Voronoi analysis is apparently shifted along the interface normal axis *X* by about 3 Å. This effect may result from the difference between the two methods concerning the mathematical treatment of the interface. In the sense of computational cost, as seen in Table 5 of Appendix B, the two methods have been found to be similar, i.e.: the time needed to analyze one single frame is not significantly different.

Since cluster analysis combined with triangular interpolation has been proven to be the most reliable and accurate combination among the sub-procedures tested, in this section we analyze the profile obtained as a result of the above mentioned pathway. The intrinsic free energy profiles calculated by the triangular interpolation method, using cluster analysis to eliminate the possibility of misidentifying hydration shell water molecules as parts of the interface when they form a separate droplet in the organic phase are shown in Figure 4.16 a. In Figure 4.16 b the intrinsic density profile of the ion free water/DCE interface calculated with respect to the intrinsic surface of the aqueous phase can be seen.

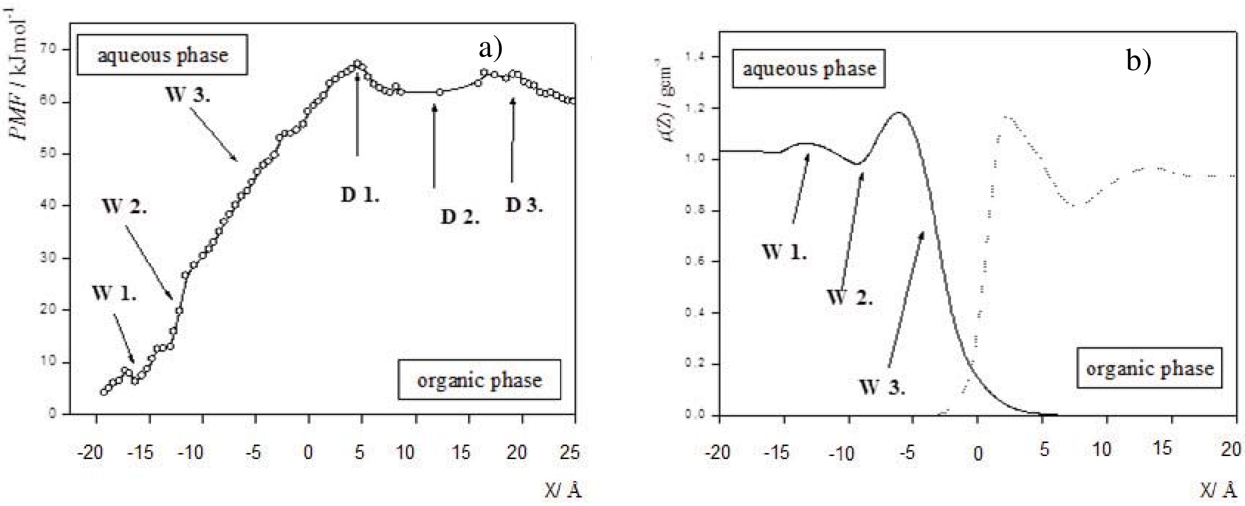

Figure 4.16 *a) Intrinsic free energy profile of the Cl^- ion through the water/DCE interface calculated by the triangular interpolation method, using the cluster analysis to differentiate cases where the hydration shell is part of the interface from those where it forms a separate cluster in the organic phase. On the X axis the intrinsic distance of the ion from the interface of the aqueous phase is shown, negative values mean that the ion is on the aqueous side of the interface whereas positive x values correspond to the ion being situated on the organic side of the interface. b) Intrinsic number density profile of the aqueous and the organic phase of the ion-free system, calculated with respect to the interface of the aqueous phase.*

Direct matching of the points on the free energy curve to those on the density profile is in theory impossible as the presence of the chloride ion alters the structure of the interface relative to which the density profile has been calculated. However, interpreting the free energy curve in terms of the density profile of the system is a natural way of understanding the energetic background of the transfer process and is, with some constraints, possible in the framework of this study. Comparison can be made if the ion is positioned such that the interface of the ion free system is similar to that obtained in the presence of the ion. ITIM analysis of the interface of the aqueous phase at several different, randomly chosen ion positions have been performed. The roughness of the intrinsic interface has been analyzed as seen in Chapter 2.7.2.1. Namely, the amplitude and the frequency-like parameters which can describe the surface roughness accurately if examined together have been investigated to justify the validity interval for such a comparison. Our analyzes have shown that the comparison of the density profile with the intrinsic free energy profile is feasible, that is the interface of the aqueous phase in the presence of the ion is similar to that of the ion free system, until the formation of a water finger brought about by the ion crossing the interface, which manifests as a sharp increase in the amplitude of the surface roughness, begins.

It should also be noted here that the zero abscissa value of the intrinsic free energy profile does not coincide with that of the non-intrinsic one. In the non-intrinsic case we have used the center of mass of the aqueous phase as the origin, whereas for interpreting the intrinsic profile this choice would have been physically meaningless. In the intrinsic case the zero abscissa value corresponds to an arrangement in which the distance of the ion from the real, fluctuating interface, more precisely the closest point of the interface, is exactly zero. Negative X values mean that the ion is at the aqueous side of the interface whereas positive values of the abscissa correspond to the ion being situated on the organic side. The free energy difference between the two bulk phases calculated from the intrinsic profile has turned out to be 55 kJ/mol (12 kcal/mol), which is in sufficiently good agreement with that obtained in the non-intrinsic case. This observation shows that the bulk phase interactions are not affected significantly by the instantaneous fluctuations of the interface brought about by the capillary wave effect.

However, upon approaching the interfacial region the effect of the above mentioned fluctuations becomes clearly visible in the intrinsic profile. Differences between the intrinsic and the non-intrinsic profiles are seen already at relatively large intrinsic distances. The first observable feature on the intrinsic free energy profile is the slight but clear minimum seen at X=-15 Å. This region (W1) on the curve may correspond to the maximum on the intrinsic density profile of the aqueous phase which is also marked as W1 in Figure 4.16 b for the sake of clarity. Similarly to what has been observed in the case of the SCN^- ion, the minimum in the free energy profile and the subsequent enhancement of the ion's concentration below the interface is due to the presence of an opposite phase. As the enhancement of the concentration of certain ions directly at the interface has been observed experimentally at the free water surface, we may conclude that finding a similar free energy minimum (and an enhanced concentration region) below the interface can be attributed to the fact that the organic molecules can, to a certain extent, penetrate into the aqueous phase and push the enhancement zone back towards the bulk organic phase by developing energetically less favorable interactions with the ion. Thus the minimum on the free energy profile will appear in a region where DCE molecules cannot enter. According to the density profiles of the aqueous and the DCE phase the innermost point where DCE molecules are still present in the aqueous phase coincides roughly with a local minimum of the density of water molecules. However, the local decrease in water density means energetically less favorable circumstances for the ion, thus the free energy minimum appears slightly below this point, where a local maximum is seen in the density profile.

At somewhat smaller intrinsic distance values we encounter a steeply increasing region (W2) in the free energy profile. The width of this steeply increasing part is roughly 1.4 Å which is equal to the width of the region in the intrinsic density profile also labeled W2, where the profile descends from the local maximum to a local minimum. This region is characterized by a slight decrease in the hydration number of the Cl^- ion compared to the value obtained in the bulk aqueous phase, as indicated in Fig. 4.16. At even smaller intrinsic distances (region W3), the interplay between the increasing water density and the increasing number of DCE molecules in the aqueous phase results in conditions that induce the monotonic increase in the free energy of the ion as it approaches the interface.

Unlike the non-intrinsic profile, the intrinsic one exhibits a clear maximum of 67 kJ/mol at an intrinsic distance value of 4.5 Å (point D1.), that is, very close to the interface but already on the organic side. The appearance of this maximum can be attributed to the fact described in several studies that as the ion crosses the interface it pulls out a water finger with itself being situated on the top of it. This kind of arrangement maximizes the number of dichloroethane molecules which are in direct contact with the Cl^- ion and, in turn, it creates an energetically unfavorable environment. In other words, the shading effect of the hydration shell water molecules surrounding the ion is reduced in such cases. Our assumption about the physical significance of the appearance of the above-mentioned maximum is well supported by the fact that the hydration number of the Cl^- ion at positions corresponding to intrinsic distances in this region has turned out to be considerably (by 15%) smaller than that observed in any of the bulk phases. The ratio of hydration numbers calculated as the area under the first peak of the corresponding radial distribution functions of the ion and the oxygen atom of the water molecules at different ion positions are shown in Figure 4.17. evidencing our finding. It follows from the origin of the global maximum in the intrinsic free energy profile, that in this region direct matching with the intrinsic density curve is already meaningless, since the presence of the ion disturbs the interface to such an extent by forming this water finger that meaningful comparison would require recalculation the intrinsic density profile curve for both water and DCE "on the fly" for each analyzed frame, which is however computationally quite costly and at the same time unnecessary, as this part of the profile can be interpreted independently from the density of the system.

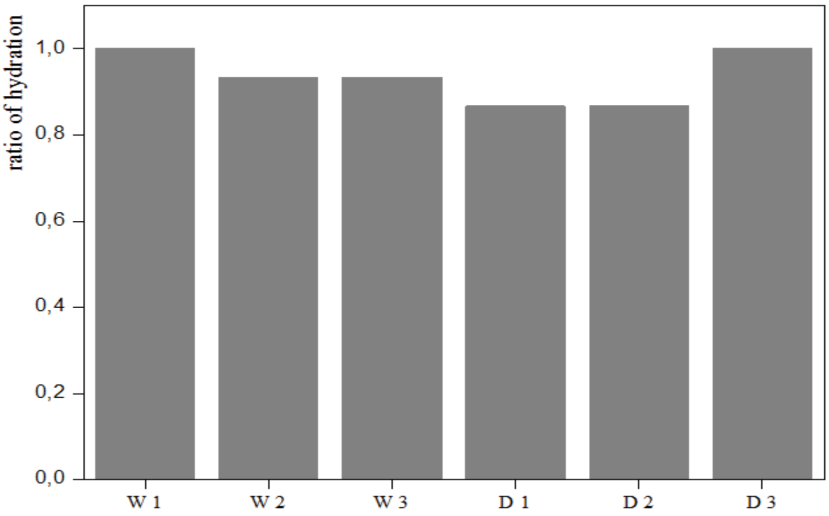

Figure 4.17 *Ratio of Hydration Numbers in the 6 different regions obtained from the Ow-Cl radial distribution functions at different positions of the ion relative to the interface.*

This maximum is followed by a roughly 7 Å wide under-sampled region on the profile, ranging from 9 to 16 Å (D2.) Under-sampling in the framework of our intrinsic approach suggests that no configuration characterized by such intrinsic distance values between the ion and the interface occurs during the course of the simulation. Knowing that the coordinates of the ion are fixed in the simulations, and are translated by 0.1 nm between two consecutive constraint force runs, the presence of the under-sampled region can be attributed to a sudden movement or relaxation of the interface after the release of the ion and its hydration shell. In other words, the lack of points in this region suggests that the relaxation of the interface is not a smooth continuous process. More precisely, as the slab width used during the reconstruction of the intrinsic free energy profile is chosen to be equal to the magnitude the displacement between two consecutive runs, a smooth gradual relaxation of the interface would prevent the formation of empty slabs. Thus, the interface is suspected to retreat rapidly to its original position, on the time scale of the step between two analyzed frames that is of 5 ps, to its original position. The driving force of this process may be the considerable energy gain connected to the recovery of the total two dimensional percolating network of the interface after the breakage of the ion's hydration shell. This dynamic property cannot be anticipated from the non-intrinsic profile, calculated from the time average of the forces acting on the ion, in which this region seems to be continuous. However, considering that the breakage of the hydration shell happens in a way that right after the final detachment the hydrated ion will be situated quite far away from the interface, physically meaningful sampling of the above mentioned region should be actually impossible. Thus the continuity in this region of the free energy profile might be considered as an artifact due to the time averaging used in the non-intrinsic analysis.

Finally, the curve exhibits a steeply decreasing part which follows the above mentioned under-sampled region, after which the free energy reaches a plateau (D3) which corresponds to the similar average value of the free energy of solvation of a chloride ion in 1,2-dichloroethane to what has been seen in the non-intrinsic profile. This latter finding supports the idea that the intrinsic treatment of the interface does not have a significant effect on the average value of the calculated free energy of solvation.

4.2.2.5 Summary and evaluation of the new intrinsic method

In this work we have presented detailed calculations for determining the solvation free energy profile of a SCN^- and a Cl^- ion across the water/DCE liquid/liquid interface. Our results concerning the SCN^- ion have shown that the free energy cost of transferring the ion from the bulk aqueous to the bulk DCE phase is about 70 kJ/mol. A local free energy minimum has been observed in the subsurface water region, just beyond the point up to which DCE can penetrate into the aqueous phase along the molecularly rugged interface. The presence of this free energy well indicates the ability of the SCN^- ion for being adsorbed at the close vicinity of the interface. It has also been seen that the SCN^- ion enters into the organic phase along with the water molecules constituting its first hydration shell. This fact also leads to the preference of such orientations at the interface in which the bulky S atom remains at the aqueous side of the interface, whilst the smaller N atom, together with its smaller first hydration shell penetrates to DCE.

The findings listed above emphasize that the shape of the free energy profile of ions through fluid interfaces is strongly dictated by the nature, more precisely the molecular level structure of the interface. We have thus developed a new method based on the ITIM analysis of the interface to reconstruct the free energy profile of small molecular penetrants across fluid interfaces. During the course of method development we have faced three major difficulties, (*i*) the computational cost of the ITIM analysis had to be reduced considerably to make it applicable for a large number of calculations, as our method relies inherently on knowing the list of interfacial molecules in every sample configuration. (*ii*) Existing methods to calculate the intrinsic distance between a surface and a point, namely the Voronoi method and the triangular interpolation, had to be tested in terms of computational cost. (*iii*) Finally, the most severe difficulty we had to face was to develop a correct treatment of the water molecules constituting the first hydration shell of the ion that are known to be coextracted to aqueous phase.

The cost of the ITIM analysis could eventually be successfully reduced by, instead of mapping the entire interface, choosing small set of test lines which lie laterally close to the ion, and thus only mapping a small portion of the surface. Nevertheless we should note here that the cost of the ITIM analysis, even after speeding up the algorithm is comparable to that of the time demand of the simulation. Thus here further development should be effectuated. Among two basic methods to determine the distance between a point and the portion of the intrinsic interface no substantial differences have been found it terms of efficacy and computational cost, thus it has been agreed, that triangular interpolation, whose accuracy has been proven to be higher should be used in the analysis. The question of the hydration shell could be most successfully addressed by performing cluster analysis on the set of water molecules which form the hydration shell, for each configuration, prior to the ITIM analysis, in the computationally most effective way possible. More precisely, this analysis by simply checking the size of the smallest cluster these water molecules belong to and decide if for any of them it exceeds a multiple of the average hydration number, as it is a clear indication of the hydration shell being part of the interface. In this case thus the hydration shell water molecules are included in the surface analysis, otherwise they are disregarded. We are aware of the fact that computational cost of the intrinsic treatment of the surface in such questions is high, however the information obtainable from an intrinsic free energy profile is definitely much more detailed than what could be yielded by the traditional non-intrinsic treatment.

The features of the intrinsic free energy profile as obtained from constrained force simulations has turned out to be significantly more detailed than the corresponding non-intrinsic one. The two most important differences between the intrinsic and non intrinsic free energy profiles, i.e.: the presence of a pronounced maximum and the appearance of an under-sampled region right beyond the maximum, can be attributed partly to the fact that the presence of the ion in the close proximity of the interface further enhances its corrugations due to the change of electrostatic interactions, partly to that the ion, naturally tries to minimize its interactions with the repulsive environment of the organic phase by co-extracting its hydration shell. Indeed, with the intrinsic treatment of the free energy profile we have been able prove in statistically relevant way the fact that, as it has been seen a number of times from the analysis of snapshots of constrained force simulations, when the ion pulls its hydration shell out of the aqueous phase towards the boundary of the two phases, it is situated in the tip of the water finger. This characteristic can be assigned to the appearance of a pronounced maximum in the profile. More clearly this maximum is exhibited due to the fact that in the above mentioned arrangement the ion experiences a maximal repulsive force since its direct contact with DCE molecules is maximized by such a structure. Note that in any other region along the reaction coordinate, even in the organic phase, the ion's repulsive interactions are shielded by the presence of at least the water molecules constituting the first hydration shell. On the other hand, the observed under-sampled region following the maximum, another feature which is averaged out by the non-intrinsic treatment, could be attributed to the fact that after the final breakaway of the ion from the aqueous phase, it is repelled from the interface thus leaving a number of points along the intrinsic reaction coordinate (the intrinsic distance from the interface) unvisited.

All things considered, the above-mentioned features, which are in turn all washed away by the use of the Gibbs dividing surface as a reference for interpreting the free energy profile obtained from constrained force simulations, are indeed important in understanding the detailed mechanism of ion transfer along various interfaces. Thus, the use of the intrinsic treatment of the interface, even at the expense of the increase in computational effort, is highly important.

Chapter 5

Conclusions and perspectives

In this dissertation I have presented my work aimed mainly at the demonstration of the ability of classical atomistic computer simulations (namely Monte Carlo and molecular dynamics methods) to model various non-trivial processes and phenomena related to both solid and liquid interfaces, such as adsorption and competitive adsorption.

Classical computer simulations are nowadays commonly used and easily available techniques to investigate several physico-chemical phenomena. One of the main advantages connected to the use of computer simulations is that, besides the possibility to reconstruct mean macroscopic values of thermodynamic quantities by either ensemble or time averaging over the trajectories obtained during the simulation, they can directly provide a picture of our system of interest in an atomistic resolution without the necessity of using an expensive experimental setup even under conditions which are experimentally not trivial to achieve. On the other hand, molecular dynamics in particular, can also yield dynamic information by the analysis of the trajectories saved during the course of the simulations. Thus we can conclude that computer simulation tools may be used as instantaneous imaging techniques (analogous to highly developed microscopy techniques such as STM or AFM), as methods to obtain thermodynamic quantities and finally for analyzing dynamic properties. Nevertheless, it should be always kept in mind, that since the application of classical computer simulations inherently requires the use of a simplified model of the real system of interest, the obtained data can only be meaningfully interpreted within the framework of the validity of the model. The validity of the model, on the other hand, can be conveniently justified by comparison of the data obtained from the simulation for the model system with experimental data obtained for the corresponding real system. Thus to be able to meaningfully interpret the results of my simulations I have attempted to compare the data obtained from each of my studies with existing experimental findings whenever it was possible.

My work on solid interfaces is comprised of three main topics, each related to environmentally important phenomena connected to questions of air pollution and climate evolution occurring in the troposphere, that is the region of the atmosphere following the lowermost boundary layer. The first among these studies is the grand canonical Monte Carlo simulation of the adsorption of acetaldehyde on the surface of ice under tropospheric conditions (i.e.: at 200 K). The grand canonical Monte Carlo technique made it possible to reconstruct the adsorption isotherm by directly monitoring the number of inserted acetaldehyde molecules in the simulation box as a function of the chemical potential of the system. The obtained isotherms could be well fitted with the Langmuir model of adsorption, suggesting that the adsorbed layer is monomolecular and lateral interactions between acetaldehyde molecules adsorbed at the ice surface were negligibly small. The analysis of the molecular level structure of the adsorbed layer has shown that acetaldehyde molecules are most commonly connected to the surface by one single hydrogen-bond formed between their carbonyl group and a dangling H of the ice surface, thus turning their C=O group towards the surface, and pointing outwards with the methyl group, this outward orientation can be parallel to the interface (in the extreme case of very high surface coverage) but can also turn in a direction which is slightly tilted with respect to the interface normal axis, in order to maximize dipole-dipole attraction between the molecules of the adsorbed layer. Our findings have agreed sufficiently well with those of FTIR studies.

The second topic connected to solid surfaces has been the molecular dynamics study of the adsorption bifunctional organic compounds (which are important factors in the chemistry of the troposphere) on ice under the conditions relevant in the troposphere. The main importance of this work lies in the fact that, to the best of our knowledge, this study was the first to investigate the applicability of MD simulations for describing the energetics and dynamics of interactions between ice surfaces and bifunctional molecules. As model compounds we have chosen two molecules which are present in relatively high amounts in the upper region of the troposphere, namely oxalic acid and hydroxyacetone. The results obtained for oxalic acid have shown that, *i*) this molecule is adsorbed readily on the surface of ice by the formation of a number of hydrogen bonds, even at the expense of loosing its outstandingly stable gas phase structure; *ii*) the molecules in the adsorption layer are not evenly distributed and upon increasing the temperature, the stable adsorption layer is characterized by an increasing extent of lateral aggregation of the oxalic acid molecules, and the subsequent formation of uncovered patches on the ice surface; *iii*) due to the formation of these uncovered patches, which can eventually serve as ducts for water molecules to leave the surface, the increase of the temperature causes the departure of water molecules from the ice phase rather than that of oxalic acid molecules from the stable adsorbed layer. The results of our simulations have been found to be in agreement with, and could qualitatively explain the experimental adsorption and thermally induced desorption studies of the oxalic acid/ice system evidencing that the desorption of water molecules takes place at lower temperature than that of oxalic acids even if the upper layer is built up of the latter species. Results obtained for the hydroxyacetone/ice system, on the other hand, were burdened by severe weaknesses of the, to the best of our knowledge, single existing model of the molecule.

The third question of large atmospheric interest that I have addressed is the computational modeling of the phase behavior of binary water/organic aerosols known as cloud condensation nuclei. Here we have proposed a simulation protocol, based on the molecular dynamics method, to reconstruct the phase diagram of binary aerosols on ice. The model compounds used in this work were oxalic acid/water and malonic acid/water systems, the latter added to shed light on the effect of the carbon chain length on the aerosol's efficacy as a cloud condensation nucleus. The question of the effect of humidity has been also addressed by performing the simulations at two different water contents, corresponding to cases when *i*) the stable hydrate formation is hindered by the low water concentration and when *ii*) the amount of water exceeds the concentration needed for the formation of a dihydrate in the case of oxalic and a hexahydrate in the case of malonic acid. The results of this study have revealed the fact that the average size of the pure organic aerosol particle depends strongly on the molecular size. Namely the larger the molecule the bigger the average aggregation number. Secondly, the phase behavior of the corresponding binary aerosols has been found to be markedly different for the two organic compounds. The details of phase diagram of the oxalic acid/water systems have been found to depend strongly on the concentration. Nevertheless, at each composition the stable phase at low temperatures has been represented by one big organic aggregate with the water molecules adsorbed on its surface whose disintegration could be observed at the highest examined temperatures to form small oligomeric droplets. In the case of malonic acid, on the other hand, the phase behavior has been found to be independent of the water concentration in the examined range and, more importantly, no disintegration of the original large aggregate could be observed. Thermodynamic analysis of the results suggests that the phase diagram is governed largely by entropic factors. The comparison of our findings with recent experiments about the relation between the O:C ratio and the cloud condensation potency of the aerosol implies that the disintegration of the particles into small droplets can be connected to the increased efficacy of oxalic acid/water binary aerosols as cloud condensation nuclei.

My work on liquid interfaces can be divided into two main topics. The first among them is the investigation of the competitive adsorption of poly(ethylene-oxide) and sodium dodecyle sulfate at the free interface of water, whereas the second is the study of the transfer of ions through liquid/liquid interfaces by means of the potential of mean force method. The latter one includes the development of a new, intrinsic surface analysis based method to reconstruct the free energy profile from constrained simulations.

The study of the competitive adsorption of PEO and SDS at the water surface can be, besides its significance in fundamental science, important for industrial applications, since the complexes of these two molecules are present in several products of chemical industry. We have performed molecular dynamics simulations and ITIM analyses of the free interface of the water/PEO system at different SDS concentrations to reveal the details and the thermodynamic background of the mechanism by which the PEO segments are eventually displaced by the DS^- ions at the surface. Here we have found that the mechanism of competition is indeed complex, and the displacement happens in a segment by segment manner. In the absence of SDS the PEO molecules have been found to be anchored to the surface only by a few segments, whereas the rest of segments are arranged in long loops towards the bulk liquid phase and short but perceivable loops towards the vapor phase. At small SDS surface concentrations almost the entire PEO molecule has been found at the interface, and only a considerably high amount of SDS has led to its departure. Another important finding of this study has been the fact that PEO segments can form loops towards the apolar phase (vapor or in the presence of a SDS a hydrocarbon region) as well as towards the bulk aqueous phase, which had never been included so far in any of the models of polymer adsorption. Finally the possibility of the formation of polymer-surfactant complexes which are well-known structures of the aqueous phase has also been observed at the interface in our simulations.

The other main topic of my studies concerning fluid interfaces has been the reconstruction of the free energy profile of different ions (thiocyanate and chloride) across the liquid/liquid interface of water and 1,2-dichloroethane from constrained force simulations. This work included the development of a method to calculate the free energy profile with respect to the real intrinsic interface. The results of the intrinsic analysis of our test system (water/DCE/Cl^-) has revealed that the intrinsic free energy profile provides a considerably more detailed view on the mechanism of transfer than the corresponding non-intrinsic one. Indeed, the fact that in the non intrinsic treatment the profile is usually anchored to the Gibbs-dividing surface instead of the instantaneous intrinsic interface, has been found to wash away features of the profile which correspond to such important details of the mechanism of transfer as the structure of the water finger pulled by the ion when crossing the interface or the manner by which the first hydration shell coextracted with the ion finally breaks away from the bulk aqueous phase. Information about these can be obtained only by the intrinsic approach. Thus, even if the computational cost of such analysis if somewhat higher than that of the non-intrinsic one, our results suggest that it is recommended adopt the intrinsic treatment in order to obtain a more detailed picture of the mechanism of transfer.

My work has shed light on the wide range of applicability of computer simulations in the field of modeling interfacial processes. Obviously there are several unexplored areas which are currently subject of investigations in our group. Concerning solid surfaces, the development has taken a direction to model the competitive incorporation of small molecules such as CO or noble gases into clathrate hydrates which, are of great interest for the community of astrophysicists. We have started recently to adapt grand canonical Monte Carlo simulations, used so far for modeling the competitive adsorption of small molecules on zeolites, to be able to perform that kind the above-mentioned analysis.

In the field of fluid interfaces the two main directions of development are the following. First of all investigations of the structure and dynamics of the adsorption layer of several ionic and non-ionic surfactants is going on currently. The main target of this work is to investigate the lateral diffusion of surfactants at the interface. On the other hand, we have also started recently to characterize the depth to which a surfactants can penetrate into the subsurface layers by means of a modification of the ITIM analysis. Both of these studies are aimed at developing the currently existing theoretical models of surfactant adsorption at fluid interfaces. Secondly our new method to reconstruct free energy profile with respect to the intrinsic interface is also going on. Currently we are testing the ability of our method to describe the transfer of complex ions (SCN^-) and of neutral molecules such as methane and other small organic compounds.

Bibliography

Publications serving as a basis of this thesis:

[1] *Adsorption of Acetaldehyde on Ice* M. Darvas,S. Picaud,P. Jedlovszky, J. Lasne,C. Laffon and P. Parent *Langmuir* **28**, 4198, (2012).

[2] *Molecular Dynamics Simulation of the Adsorption of Oxalic Acid on Ice Surface* M. Darvas, S. Picaud, and P. Jedlovszky *ChemPhysChem.* **11**, 3971 (2010).

[3] *Adsorption of Hydroxyacetone on Pure Ice Surfaces* M. Petitjean, M. Darvas, S. Le Calvé, P. Jedlovszky, and S. Picaud *ChemPhysChem.* **11**, 3921 (2010).

[4] *Oxalic Acid Aerosols as Cloud Condensation Nuclei. A Computer Simulation Study* M. Darvas, S. Picaud and P. Jedlovszky *Phys. Chem. Chem. Phys.* **13**, 19830, (2011).

[5] *Molecular dynamics simulations of the water adsorption around malonic acid aerosol models* M. Darvas, S. Picaud, P. Jedlovszky (submitted for publication *(J.Chem.Phys.)*)

[6] *Adsorption of Poly(Ethylene-Oxide) at the Free Water Surface. A Computer Simulation Study* M. Darvas, T. Gilányi, and P. Jedlovszky *J. Phys. Chem. B* **114**, 10995 (2010).

[7] *Competitive Adsorption of Surfactants and Polymers at the Free Water Surface. A Computer Simulation Study of the Sodium Dodecyle Sulfate* - Poly(ethylene oxide) System M. Darvas, T. Gilányi, and P. Jedlovszky *J. Phys. Chem. B* **115**, 933 (2011).

[8] *Solvation Free Energy Profile of the SCN- Ion Across the Water - 1,2-Dichloroethane Liquid/Liquid Interface. A Computer Simulation Study* M. Darvas, M. Jorge, M. N. D. S. Cordeiro, and P. Jedlovszky *J. Phys. Chem. C* **115** 11140 (2011).

[9] *Calculations of the Intrinsic Free Energy Profile of a Penentrant Ion across the Liquid/Liquid Interface in Computer Simulation*s M. Darvas, M. Jorge, M. N. D. S. Cordeiro, M. Sega, S. Kantorovich, and P. Jedlovszky (submitted for publication (*Phys. Rev. Lett.)*)

1) Gibbs, J.W. Transactions of the Connecticut Academy of Art and Science, **111**, (1874-78).

2) Rüdenberg, R. *Naturwissen Schaften*, **20**, (1916), 522.

3) Max, K. *Zeitschrift für Technische Physik*, **16**, (1935), 467.

4) von Ardenne, M. *Zeitschrift für Physik*, **109**, (), 553.

5) Binning, G.; Gerber, G.; Quate, C.F. *Phys. Rev. Lett.*, **56**, (1986), 930.

6) Bloembergen, N.; Schawlow, A. L.;Siegbahn, K.M. *Nobel Prize Lecture in Physics*, (1981).

7) Shen, Y.R. *Natute*, **337**, (1989), 519.

8) B.C. Smith, Fundamentals of Fourier Transform Infrared Spectroscopy, CRC Press, Boca Raton, FL, 1996.

9) Duncan J. Shaw: Introduction to Colloid and Surface Chemistry Third Edition, London-Boston, Butterworth & Co Ltd. 1980.

10) Varga, I.; Keszthelyi,T.; Mészáros, R.; Hakkel, O.;Gilányi, T. *J. Phys. Chem. B.* **109**, (2005), 872.

11) Meriona, T.S.; Marmurb, A.; Saguya, I.S. *J. Coll. Int Sci.*, **274**, (2004), 637.

12) Allen, M. P.; Tieldsley, D. J. Computer Simulation of Liquids, Oxford, Oxford University Press, 1987.

13) Doran, M. B.; Zucker, I. J. *J. Phys* **C4**, (1971), 307.

14) (a) Lorentz, H.A. *Ann. Phys.*; **12**, (1881), 127.

(b) Berthelot, D. *Comtes rendus hebdominaires des séances de L'Académie des Sciences*, **126**, (1898),1703.

15) Ewald, P. *Ann. Phys.*, **64**, (1921), 253.

16) Essman, U.; Perera, L.; Berkowitz, M. L.; Darden, T.; Lee, H.; Pedersen, L. G. *J. Chem. Phys.* **103**, (1995), 857.

17) Barker, J.A.; Watts,R.O. *Mol. Phys.* **26**, (1973), 789.

18) Metropolis, N.; Rosenbluth, A. W.; Rosenbluth, M. N.; Teller, A. H.; Teller, E. *J. Chem. Phys*, **21**, (1953), 1087.

19) Norman, G. E.; Filinov, V. S. *High. Temp. USSR*, **7** (1969), 216.

20) Adams, D. J. *Mol. Phys*. **28**, (1974), 1241.

21) Adams, D. J. *Mol. Phys*. **29**, (1975), 307.

22) Mezey, M.. *Mol. Phys*. **40**, (1980), 901.

23) Mezey, M.. *Mol. Phys*. **61**, (1987), 565. (Erratum: *Mol. Phys*. **67**, (1989), 1207.

24) Verlet, L. *Phys. Rev.*, **159** (1967), 98.

25) Pártay, L. B.; Hantal, G.; Jedlovszky, P.; Vincze, Á.; Horvai, G. *J. Comput. Chem.,* **29**, (2008), 945.

26) Idrissi, A. ; Damay, P. ; Yukichi, K. ; Jedlovszky, P. *J. Chem. Phys.* **2008,** *129*, 164512.

27) Voronoi,G.F. *J. Reine Angew. Math.* **1908,** *134*, 198

28) Zaninetti, L. *Phys. Lett. A* **1992,** *165*, 14

29) Ruocco, G.; Sampoli, M.; Vallauri, R. *J. Chem. Phys.* **1992,** *96*, 6167.]

30) Kollman, P. *Chem. Rev.* **93**, (1993), 2395.

31) Kirkwood, J. G. Collected Works: Theory of Liquid, Gordon&Breach, New York (1968).

32) Zwanzig, R. J. Chem. Phys. 22 (1954), 1420.

33) Kästner J. Umbrella Sampling Wiley Interdisciplinary Reviews:Computational Molecular Science, **1**, (2011), 931.

34) Berendsen, H. J. C.; Postma, J. P. M.; DiNola, A.; Haak J. R. *J. Chem. Phys*., **81**, (1984), 3684.

35) Izrailev, S.; Stepaniants, S.; Isralewitz, B.; Kosztin, D.; Lu, H.; Molnar, F.; Wriggers, W.; Schulten, K. in Deuflhard, P.; Hermans, J.; Leimkuhler, B.; Mark, A.; R. Skeel, R.; Reich S.: Computational Molecular Dynamics: Challenges, Methods, Ideas, Springer-Verlag, (1999).

36) Laio, A.; Parrinello, M. *Proc.. Natl. Acad. Sci.USA,* **99**, (2002), 12562.

37) Sugita, Y.; Okamoto, Y.; *Chemical Physics Letters* **314**: (1999) 141.

38) Earl, D. J.; Deem, M. W. *Phys. Chem. Chem. Phys.*, **7**, (2005) 3910.

39) Jorge, M.; Hantal, G.; Jedlovszky, P.; Cordeiro, M.N.D.S. *J. Phys. Chem. C* **114**, (2010), 18656.

40) Kirkwood J G *J. Chem. Phys*., **3**, (1935), 300.

41) Pártay, L.B.;Hantal, Gy.; Jedlovszky, P.; Vincze, A.; Horvai; G. *J. Phys. Condens. Matter.* **29** (2008) 945.

42) de Dios Lopez-Gonzalez, J. ; Carpenter, F.G.; Deitz, V.R. *J.Phys.Chem.* , **65**, (1961) 1112.

43) Hellemans, R.; van Itterbeek, A.; van Dael, W. *Physica*, **34**, (1967), 429.

44) Kulprathipanja, S. Zeolites in Industrial Separation and Catalysis, Wiley (2010). an refernces therein

45) Langmuir *Principles of Adsorption and Reaction on Solid Surfaces*. Wiley Interscience. 1996. 240 .

46) Brunauer, S.; Emmett, P. H.; Teller, E. *J. Am. Chem. Soc.*, **60**, (1938), 309.

47) Freundlich, H. *Kapillarchemie*, Academishe Bibliotek, Leipzig (1909).

48) Temkin, M.I., and V. Pyzhev, *Acta Physiochim. URSS* **12**, (1940), 217.

49) Kuo-Nan, L. *Monthly Weather Review* **114** (1986), 1167.

50) Pöschl, U., *Angew. Chem. Int. Ed.* **2005**, *44*, 7520-7540.

51) Finlayson-Pitts, B.J. *Phys. Chem. Chem. Phys.* **2009**, *11*, 7760-7779.

52) Goldstein, A.H. and Galbally, I.E. *Environ. Sci. Technol.* **2007**, *41*, 1514-1521.

53) Henderson, J. R.; van Swol, F. *Mol. Phys*. **51**, (1984), 991.

54) Henderson, J. R.; van Swol, F. *Mol. Phys*. **56**, (1985), 1313.

55) Sikkenk, J. H.; Indekeu, J. O.; van Leuwen, J. M. J. *Phys. Rev. Lett* **59**, (1987), 98.

56)Heinzinger, K.; Spohr, E. *J. Chem. Phys*. **84**, (1986), 2304.

57) Foster, K.; Raghavan, K.; Berkowitz, M. *Chem. Phys. Lett.* **162**, (1989), 32.

58) Perram, J. W.; White, L. R., *Faraday Discuss. Chem. Soc.,* **59**, (1975), 29.

59) Evans, R.; Tarazona, P.; Marini Bettolo Marconi, U. *Mol. Phys*, **50**, (1983), 993.

60) Ohnesorge, R.; Löwen, H.; Wagner, H. *Phys. Rev. E.,* **50**, (1994), 4801.

61) Raghavan, K.; Foster, K.; Berkowitz, M. *Chem. Phys. Lett*., **177**, (1991),426.

62) Lyem, S. Y.; Chan, K. Y. *Surf. Sci.* **328**, (1995), 119.

63) Pohl, P. I. *Mol. Phys.,* **89**, (1996), 1725

64) Wang Q.; Johnson, J. K.; *J. Phys. Chem. B*, **103**, (1999), 277.

65) Yoshioka, T.; Tsuru, T.; Asaeda, M.; *Sep. Purif. Technol.,* **25**, (2001), 441.

66) Yang, Q.; Zhong, C. *J. Phys.Chem B* **109** (2005), 11862.

67) Krishna, R.; van Baten, J.M. Micropor. Mesopor. Mater. **109,** (2008), 91.

68)Garberoglio, G. *Langmuir*, **23,** (2007), 12154.

69)Battisti, A.; Taioli, S.; Garberoglio, G. Micropor. Mesopor. Mater. **143**, (2011), 46.

70) Winkler, A.K.; Holmes, N. S.; Crowley, J.N. *Phys. Chem. Chem. Phys.***2002**, *4*, 5270.

71) Giddings, C. J. Sokolov, O. and Abbatt, J.P.D., *J. Phys. Chem. A*, **106** (2002) 775.

72) Domine, F.; Rey-Hanot, L. *Geophys. Res. Lett.*, **29**, (2002) 1873.

73) Hudson, P. K.; Zondlo, M. A.; Tolbert, M. A. *J. Phys. Chem. A* **106**, (2022) 2882.

74) Abbatt, J. P. D. *Chem. Rev.* 1**03**, (2003) 4783.

75)Bartels-Rausch, T.;Guimbaud, C.; Gäggeler, H. W.; Ammann, M. *Geophys. Res. Lett.* **31**, (2004) L16110.

76) Peybernès, N.; Marchand, C.; Le Calvé, S.; Mirabel, P. *Phys. Chem.Chem. Phys.* **6** (2004) 1277.

77) Picaud, S.; Hoang, P. N. M.; Peybernès, N.; Le Calvé, S.; Mirabel, P. *J. Chem. Phys.* **122,** (2005) 194707.

78) Behr, P.; Terziyski, A.; Zellner, R. *J. Phys. Chem. A* **110**, (2006), 8098.

79) von Hessberg, P.; Pouvesle, N.; Winkler, A: K.; Schuster, G.; Crowley, J. N. *Phys. Chem. Chem. Phys.* **10,** (2008) 2345.

80) Picaud, S.; Hoang, P. N. M. *J. Chem. Phys.* **112,** (2000)**,** 9898.

81) Marinelli, F.; Allouche, A. *Chem. Phys.* **272,** (2001),137.

82) Colligno, B.; Picaud, S. *Chem. Phys. Lett.* **393,** (2004), 457.

83) Peybernès, N.; Le Calvé, S.; Mirabel, P.; Picaud, S.; Hoang, P. N. M. *J. Phys. Chem. B* **108**, (2004), 17425.

84) Allouche, A. *J. Chem. Phys.* **122,** (2005), 234703.

85) Ballenegger, V.; Picaud, S.; Toubin, C. *Chem. Phys. Lett.* **432,**(2006), *432*, 78.

86) Jedlovszky, P.; Pártay, L B; Hoang, P. N: M.; Picaud, S.; von Hessberg, P.; Crowley, J. N. *J. Am. Chem. Soc.* **128,** (2006),15300.

87) Thierfelder, C.; Schmidt, W. G. *Phys. Rev. B* **76**,(2007),195426.

88) Pártay, L. B.; Jedlovszky, P.; Hoang, P. N. M.; Picaud, S.; Mezei, M. *J.Phys. Chem. C* **111**, (2007), 9407.

89) Hantal, G., Jedlovszky, P.; Hoang, P. N. M.; Picaud, S. *J. Phys. Chem. C* **111,** (2007), 14170.

90) Jedlovszky, P.; Hantal, G.; Neurohr, K.; Picaud, S.; Hoang, P. N. M.; von Hessberg, P.; Crowley, J. N. *J. Phys. Chem. C* **112,** (2008), 8976.

91) Hantal, G.; Jedlovszky, P.; Hoang, P. N. M; Picaud, S. *Phys. Chem. Chem. Phys.* **10** (2008), 6369.

92) Hammer, S. M.; Panisch, R.; Kobus, M.; Glinnemann, J.; Schmidt, M. U. *Cryst. Eng. Comm.* **11,** (2009)**,**1291.

93) Petitjean, M.; Hantal, G.; Chauvin, C.; Mirabel, P.; Le Calvé, S.; Hoang, P. N. M.; Picaud, S.; Jedlovszky, P. *Langmuir* **26** , (2010), 9596.

94) Domine, F.; Cincinelli, A.; Bonnaud, E.; Martellini, T.; Picaud, S. *Environ. Sci. Technol.* **41** (2007), 6033.

95) Carter,W.P.L, *Atmos. Environ.* **24A** (1990), 481.

96) Zhou, X. ; Huang, G. ; K. Civerolo, K.. ;Schwab J. *Environ. Sci. Technol.* **43***,* (2009), 2753.

97) Satsumabayashi, H. ; Kurita, H. ;Yokouchi, Y. ; Ueda ; H. *Atmos. Environ.* **24,** (1990)**,**1443.

98) Kawamura, K. ;Ikushlma, K. *Environ. Sci. Technol.* **27** (1993), 2227.

99) Zhou, Y. ; Hoigné,J. *Environ. Sci. Technol.* **26**, (1992), 1014.

100) Yan, H.; Chu, L.T. *Langmuir* **24** (2008), 9410.

101) Karl,T.; Guenther, A.; Turnipseed, A; Tyndall, G.; Artaxo, P.; Martin, S. *Atmos. Chem. Phys.* **9,** (2009), 7753-7767.

102) Carter, W.P.L; Atkinson, R. *Int. J. Chem. Kinet.* **28,** (1996), 497.

103) von Kuhlmann, R.; Lawrence, M.G.; Pöschl,U.; Crutzen, P.J. *Atmos. Chem. Phys.* **4** (2004), 1.

104) Petitjean, M.; Mirabel, P.; Le Calvé, S. *J. Phys. Chem. A* **113,** (2009), 5091.

105) Vega, C.; Sanz, E.; Abascal, J. L. F. *J. Chem. Phys.* **122** (2005)**,** 114507.

106) Stubbs, J. M.; Potoff, J. J.; Siepmann, J. I. *J. Phys. Chem. B* **108** (2004)**,** 17596.

107) Mezei, M. *MMC: Monte Carlo program for simulation of molecular assemblies.* URL: http://inka.mssm.edu/~mezei/mmc.

108) Daub, C. D.; Patey G. N.; Jack, D. B.; Sallabi A. K. *J. Chem. Phys.* **124** (2006) 114706.

109) Lindahl, E.; Hess, B.;van der Spoel, D. *J. Mol. Mod.,* **7** (2001), 306

110) Berendsen, H.J.C.; Postma, J.P.M.; DiNola, A.; Haak,J.R. *J. Chem. Phys.* **81** (1984)**,** 3684.

111) Miyamoto, S.; Kollman, P.A. *J. Comp. Chem.* **13,** (1992), 952.

112) Hess, B.; Bekker, H.; Berendsen, H.J.C. ;Fraaije, J.G.E.M. *J. Comp. Chem.* **18** (1997), 1463.

113) Abascal, J.L.F.;Vega, C. *J. Chem. Phys.* **123** (2005), 23450.

114) A. Mohajeri, A.; Shakerin, N. *J. Mol. Struct. (Theochem)* **711,** (2004), 167.

115) Jorgensen, W.L.; Rivas, J.T. *J. Am. Chem. Soc.* **110,** (1988), 1657.

116) Van Alsenoy, C.; Klinowski, V.T.; Schafer, L. *J. Mol. Struct. (Theochem)* **109,** (1984), 321.
117) Krijn, M.P.C.M.; Feil, D. *J. Chem. Phys* **89,** (1988), 4199.

118) Chen, C.; Shyu S.F. *Int. J. Quantum. Chem* **76,** (2000), 541.

119) Sharma, A.; Reva, I.; Fausto, R. *J. Phys. Chem. A*, **112** (2008), 5935.

120) Schill, G.P. ;Tolbert, M.A. *J. Phys. Chem. A* **116** (2012), 6817.

121) Nosé, S. *Mol. Phys.* **52,** (1984), 255.

122) Hoover, W. G. *Phys. Rev. A* **31** (1985), 1695.

123) Parinello, M.; Rahman, A. *J. Appl. Phys.* **52**, (1981), 7182.

124) Braban, C.F.; Carroll, M.F.; Styler, S.A.; Abbatt, J.P.D *J. Phys. Chem. A*, **107** (2003), 6594.

125) Jackson, G. *Mol. Phys.*, **72**, (1991), 1365.

126) Giddings, C. J. Unified Separation Science, New York, Wiley (1991)

127) Rowlinson, J. S.; Widom, B. Molecular theory of capillarity Clarendon, Oxford, (1982).

128) Kunjappu JT, Somasundaran P. *Colloids Surf, A* **37**, (1989), 245.

129) E. Jenkel and R. Rumbach, *Z. Elektrochem.*, **55**, (1951), 612.

130) Fleer, G. J.; Cohen Stuart, M. A.; Scheutjens, J. M. H. M.; Cosgrove, T.; Vincent, B. *Polymers at Interfaces*, Chapter 5,London, Chapman & Hall, 1993.

131) Kim, M. W. *Colloids Surf. A* **128**, (1997) 145.

132) Cao, B. H.; Kim, M. W. *Europhys. Lett.* **29,** (1995), 555.

133) Huang, Q. R.; Wang, C. H. *J. Chem. Phys.* **105,** (1996), 6546.
134) Alexandridis, P. *Curr. Opin. Coll. Interface Sci.* **1**, (1996), 490.
135) Chu, B.; Zhou, Z. *Surf. Sci. Ser.* **60**, (1996), 31.
136) An, S. W.; Thomas, R. K.; Forder, C.; Billingham, N. C.; Armes, S. P.; Penfold, J. *Langmuir* **18** (2002), 5064.

137) Goddard, E. D. In *Interactions of Surfactants with Polymers and Proteins*; Goddard, E. D.; Ananthapadmanabhan, K. P.; Eds.; CRC Press: Boca Raton, 1993, Chapter 4.

138) Hansson, P.; Lindman, B. *Curr. Opin. Colloid Interface Sci.* **1** (1996), 604.

139) Holmberg, K.; Jönsson, B.; Kronberg, B.; Lindman, B. *Surfactants and Polymers in Aqueous Solution*, Wiley: New York, 2002.

140) Shirahama, K.; Tsuji, T.; Takagi, *J. Biochem. (Tokyo)* **75** (1974), 309.

141) Nagarajan, R.; Kalpakci, K. *Polym. Prepr. Am. Chem. Soc. Div. Polym. Chem.***23** (1982), 41.

142) Jones, M. N. *J. Coll. Int. Sci.* **23** (1967), 36.

143) Gilányi, T.; Wolfram, E. *Colloids Surf.* **3, (1981),** 181.

144) Cabane, B. *J. Phys. Chem.* **81** (1977)**,** 1639.

145) Goddard, E. D. *Colloids Surf.* **19** (1986)**,** 255, and references therein.

146) Dal Bo, A.; Schweitzer, B.; Felippe, A. C.; Zanette, D.; Lindman, B. *Colloids Surf. A* **256** (2005), 171.

147) Purcell, I. P.; Thomas, R. K.; Penfold, J.; Howe, A. M. *Colloids Surf. A* **94** (1995), 125.

148) Purcell, I. P.; Lu, J. R.; Thomas, R. K.; Howe, A. M.; Penfold, J. *Langmuir* **14** (1998)*,* 1637.

149) Tadros, T. F. *J. Colloid Interface Sci.* **46** (1974)**,** 528.

150) Penfold, J.; Tucker, I.; Thomas, R. K.; Zhang, J. *Langmuir* **21** (2005), *21,* 10061.

151) Penfold, J.; Tucker, I.; Thomas, R. K.; Taylor, D. J. F.; Zhang, J.; Bell, C. *Langmuir* **22** (2006)**,** 8840.

152) Cooke, D. J.; Blondel, J. A. K.; Lu, J. R.; Thomas, R. K.; Wang, Y.; Han, B.; Yan, H.; Penfold, J. *Langmuir* **14** (1998)**,** 1990.

153) Cooke, D. J.; Dong, C. C.; Lu, J. R.; Thomas, R. K.; Simister, E. A.; Penfold, J. *J. Phys. Chem. B* **102** (1998), 4912.

154) Jarvis, N. L.; Sheiman M. A. *J. Phys. Chem.* **72,** (1968), 74.

155) Randles, J. E. B. *Phys. Chem. Liq.* **7,** (1977), 107.

156) Conway, B. E. *Adv. Coll. Int. Sci.* **8,** (1977), 91.

157) Hey, M. J.; Shield, D. W.; Speight, J. M.; Will, M. C. *J. Chem. Soc. Faraday Trans.* **1**, (1981), 123.

158) Weissenborn, P. K.; Pugh, R. J. *Langmuir* **11**, (1995), 1422.

159) Onsager L., Samaras, N. N. T. *J. Chem. Phys.* **2,** (1934), 528.

160) Wagner, C. *Phys. Z.* **25,** (1924), 474.

161) Bhuiyan, L. B.; Bratko, D.; Outhwaite, C. W. *J. Phys. Chem.* **95**, (1991), 336.

162) Stairs, R. A. *Canad. J. Chem.* **73**, (1995), 781.

163) Karraker, K. A.; Radke C. J. *Adv. Coll. Int. Sci.* **96**, (2002), 231.

164) Markin, V. S.; Volkov. A. G. *J. Phys. Chem. B.* **106**, (2002), 11810.

165) Maheshwari, R.; Sreeram, K. J.; Dhathathreyan A. *Chem. Phys. Lett.* **375**, (2003), 157.

166) Manciu, M.; Ruckenstein, E. *Adv. Coll. Int. Sci.* **105**, (2003), 63.

167) Oshima, H.; Matsubara, H. *Colloid. Polym. Sci.* **282**, (2004), 1044.

168) Woelki, S.; Kohler, H. H. *Chem. Phys*. 306, (2004), 209.

169) Petersen, P. B.; Johnson, J. C.; Knutsen K. P.; Saykally, R. J. *Chem. Phys. Lett.* **397**, (2004), 46.

170) Viswanath, P.; Motschmann, H. *J. Phys. Chem. C* **112**, (2008), 2099.

171) Raymond, E. A.; Richmond, G. L. *J. Phys. Chem. B.* **112**, (2008), 5051.

172) Uchida T.; Yamaguchi, A.; Tomoni, I.; Teramae, N. *J. Phys. Chem. B* **104**, (2000)*,* 12091.

173) Barker, A. L.; Unwin, P. R. *J. Phys. Chem. B* **105**, (2001), 12019.

174) Schröder, U.; Wadhawan, J.; Evans, R. G.; Compton, R. G.; Wood, B.; Walton, D. J.; France, R. R.; Marken, F.; Bulman Page P. C.; Hayman, C. M. *J. Phys. Chem. B* **106**, (2002), 8697.

175) Fujiwara, K.; Wada, S.; Monjushira, H.; Watani, H. *Langmuir* **22**, (2006), 2452.

176) Iwahashi, T.; Miyamae, K.; Kanai, K., Seki, K. D.; Ouchi, Y. *Ionic Liquids: From Knowledge to Application,* ACS Sympsoium Series: Washington DC**,** (2010).

177) Buff, F.; Lovett, R.; Stillinger, F. H. *Phys. Rev. Lett.,* **15**, (1965), 621.

178) Stillinger, F. H. *J. Chem. Phys*., **76**, (1982), 1087.

179)Chacón, E.; Tarazona, P. *Phys. Rev. Lett.,* **91**, (2003), 166103.

180) Jorge, M.; Cordeiro, M. N. D. S. *J. Phys. Chem. C,* **111** (2007) 17612

181) Willard, A. P.; Chandler, D. *J. Phys. Chem. B*, **114**, (2010), 1954.

182) Chowdhardy, J.; Ladanyi, B. M. *J. Phys. Chem. B*, **110**, (2006), 15442.

183) Jorge, M.; Jedlovszky, P.; Cordeiro, M. N. D. S. *J. Phys. Chem. C*, **114**, (2010), 11169.

184) Smith, G. D.; Jaffe, R. L.; Yoon, D. Y. *J. Phys. Chem.* **97** (1993)**,**12752.

185) Smith, G. D.; Yoon, D. Y.; Jaffe, R. L. *Macromolecules* **26** (1993)**,** 5213.

186) Tasaki, K. *J. Am. Chem. Soc.* **118** (1996), 8459.

187) Bedrov, D.; Pekny, M.; Smith, G. D. *J. Phys. Chem. B* **102** (1998)**,**, 996.

188) Smith, G. D.; Bedrov, D.; Borodin, O. *J. Am. Chem. Soc.* **122** (2000), 9548.

189) Neyertz, S.; Brown, D. *J. Chem. Phys.* **102** (1995)**,** 9725.

190) Neyertz, S.; Brown, D.; Thomas, J. O. *J. Chem. Phys.* **101** (1994)**,** 10064.

191) Aabloo, A.; Thomas, J. *Comp. Theor. Polym. Sci.* **7** (1997)**,** 47.

192) Darvas, M.; Gilányi, T.; Jedlovszky, P. *J. Phys. Chem. B* **114** (2010), 10995.

193) Miller, A. F.; Wilson, M. R.; Cook, M. J.; Richards, R. W. *Mol. Phys.* **101** (2003)**,** 1131.

194) Schweighofer, K. J.; Essmann, U.; Berkowitz, M. L. *J. Phys. Chem. B* **101** (1997)**,** 3793.

195) Schweighofer, K. J.; Essmann, U.; Berkowitz, M. L. *J. Phys. Chem. B* **101** (1997)**,** 10775.

196) Domínguez, H.; Berkowitz, M. L. *J. Phys. Chem. B* **104** (2000**),** 5302.

197) Shang, B. Z.; Wang, Z.; Larson, R. G. *J. Phys. Chem. B* **112** (2008)**,** 2888.

198) Berendsen, H. J. C.; Postma, J. P. M.; van Gunsteren, W. F.; Hermans, J. In *Intermolecular Forces*; Pullman, B.; Ed; Reidel: Dordrecht, 1981, p. 331.

199) Hermans, J.; Berendsen, H. J. C.; van Guntseren, W. F.; Postma, J. P. M. *Biopolymers* **23** (1984)**,**1513.

200) van Guntseren, W. F; Berendsen, H. J. C. *Groningen Molecular Simulation (GROMOS) Library Manual*; Biomos: Groningen,1987.

201) Ryckaert, J. P.; Bellemans, A. *Faraday Discuss. Chem. Soc.* **66** (1978)**,** 95.

202) Mészáros, R.; Varga, I.; Gilányi, T. *J. Phys. Chem. B* **109** (2005)**,** 13538.

203) Peron, N.; Mészáros, R.; Varga, I.; Gilányi, T. *J. Colloid Interface Sci.* **313** (2007), 389.

204) Alper, H. E.; Bassolino-Klimas, D.; Stouch, T. R. *J. Chem. Phys.* **99** (1993) 5547.

205) Benjamin, I. *Science* **261** (1993), 1558.

206) Benjamin, I. *Acc. Chem. Res.* **28** (1995), 233.

207) Pedemonte, N.; Caci, E.; Sondo, E.; Caputo, A.; Rhoden, K.; Pfeffer, U.; Di Candia, M.; Bandettini, R.; Ravazzolo, R.; Zegarra-Moran, O.; Galietta, L. J. *J. Immunol.* **178** (2007), 5144.

208) Panzer, R.E.; Schaer M. G. *J. Electrochem. Soc.* **112** (1965)**,** 1136, and references therein.

209)Jorgensen, W. L.; Chandrasekhar, J.; Madura, J. D.; Impey, R. W.; Klein, M. L. *J. Chem. Phys* **79** (1983),926.

210) Benjamin, I. *J. Chem. Phys.* **97** (1992), 1432.

211) URL.: http://www.kowoma.de/en/gps/additional/atmosphere.htm

212) Lasne J.,; Laffon C.,; Parent P., *Phys. Chem. Chem. Phys.* **14**, (2012), 697.

APPENDIX A.

TABLE 1: Interaction Parameters of the Models Used in Chapter 3.

Molecule	Interaction site	σ / Å	ε / kJmol^{-1}	q/e
TIP5P water	O	3.120	0.669	0.000
	H	0.000	0.000	0.241
	L^a	0.000	0.000	–0.241
TIP4P/2005 water	O	3.158	0.775	0.000
	H	0.000	0.000	0.5564
	L	0.000	0.000	-1.11280
Acetaldehyde	CH_3	3.75	0.813	-0.043
	CH	3.72	0.448	0.525
	O	3.05	0.656	-0.482
Oxalic acid	C	3.75	0.439	0.700
	O(C=O)	2.96	0.879	-0.450
	O(OH)	3.07	0.711	-0.685
	H	0.000	0.000	0.435
Hydroxyacetone	CH_3	3.75	0.866	0.000
	CH_2	3.91	0.494	0.265
	H_{OH}	0.00	0.000	0.435
	C	3.71	0.439	0.470
	O_{OH}	2.96	0.711	-0.700
	$O_{C=O}$	3.15	0.787	-0.470
	CH_3	3.75	0.866	0.000
Malonic acid	C	3.75	0.439	0.557
	$O_{C=O}$	2.96	0.878	-0.450
	O_{OH}	3.070	0.711	-0.685
	H_{OH}	0.000	0.000	0.435
	CH_2	3.80	0.494	0.285

TABLE 2: Interaction Parameters of the Models Used in Chapter 4

Molecule	Interaction site	σ / Å	ε/kJmol^{-1}	q/e
SPC water	Ow	3.166	0.649	-0.820
	H	0.000	0.000	0.410
PEO	CH_3	3.74	0.866	0.000
	CH_2	4.07	0.410	0.250
	O	2.97	0.815	-0.500
SDS	CH_3	3.90	0.732	0.000
	CH_2	3.90	0.495	0.000
	-O-	3.00	0.716	-0.459
	=O	3.17	0.784	-0.654
	S	2.42	1.043	1.284
	Na^+	2.58	0.743	-1.000
TIP4P water	O_w	3.166	0.649	0.000
	H_w	0.000	0.000	0.520
	L^a	0.000	0.000	-1.040
SCN^-	S	3.550	1.046	-0.750
	C	3.750	0.439	0.490
	N	3.250	0.711	-0.740
Cl^-	Cl^-			
DCE	CH_2	3.800	0.494	0.227
	Cl	3.400	1.255	-0.227

APPENDIX B

TABLE 1. The enthalpic contribution to the Gibbs free energy of the oxalic acid/water binary aerosol system at selected p,T pairs, at 65 water % mole concentrations

	0.1 bar			0.5 bar			1.0 bar		
65 mol%	**U/ kJ/mol**	**pV/ kJ/mol**	**U+pV**	**U/ kJ/mol**	**pV/ kJ/mol**	**U+pV**	**U/ kJ/mol**	**pV/ kJ/mol**	**U+pV**
100 K	-6.130	-0.247	-5.883	-6.087	-0.249	-5.838	-6.026	-0.262	-5.764
175 K	-5.623	-0.159	-5.464	-5.647	-0.148	-5.499	-5.684	-0.118	-5.566
200 K	-5.689	-0.089	-5.600	-5.602	-0.095	-5.507	-5.616	-0.093	-5.523
250 K	-4.827	-0.016	-0.811	-4.723	-0.024	-0.699	-4.687	-0.041	-4.646

TABLE 2: Partition of the PEO monomer units between the three different regions of the systems simulated

	Percentage of the PEO monomer units		
SDS surface density	aqueous phase	interface	apolar phase
0 μmol/m^2	73	26	1
1 μmol/m^2	14	83	3
2 μmol/m^2	13	82	5
3 μmol/m^2	12	77	11
4 μmol/m^2	18	70	12
5 μmol/m^2	77	20	3
6 μmol/m^2	81	18	1

TABLE 3: Properties of the seven systems simulated

				surface roughness parameters			residence times (ps)		
Γ_{SDS} (μmol/m^2)	N_{SDS}	δ_{SC} (Å)	γ(mN/m)	a (Å)	ξ	<D> (Å)	τ water	τ_1 PEO	τ_2 PEO
0	0	-	51.3	3.01	0.56	19.5	5.31	56.9	6.12
1	12	7.5	40.9	3.39	0.72	23.9	4.09	98.6	0.89
2	24	9.1	27.2	4.31	0.89	24.5	5.23	171.1	2.94
3	36	11.7	23.0	5.72	1.05	21.4	6.79	145.2	5.08
4	48	12.3	15.3	11.4	1.12	23.5	8.87	152.1	4.97
5	60	13.3	14.3	9.79	1.07	23.6	17.08	167.9	8.31
6	72	14.1	14.8	13.6	1.15	25.5	17.87	205.3	8.08

TABLE 3: Partial First Shell Hydration Numbers Corresponding to the Different Atoms of the SCN$^-$ Ion, n_{hyd}, and Molecular Hydration Numbers, N_{hyd}, Obtained as the Sum of the Contributions of the S and N Atoms

Ion Position	Atom pairs	n_{hyd}	N_{hyd}
Bulk water	O_w - S	2.3	3.9
	O_w - C	4.3	
	O_w - N	1.6	
Subsurface water	O_w - S	2.3	4.3
	O_w - C	3.9	
	O_w - N	2.0	
Interface water	O_w - S	1.9	3.8
	O_w - C	3.3	
	O_w - N	1.9	
Interface DCE	O_w - S	1.8	3.5
	O_w - C	3.0	
	O_w - N	1.7	
Subsurface DCE	O_w - S	2.0	3.8
	O_w - C	3.1	
	O_w - N	1.8	
Bulk DCE	O_w - S	2.2	4.2
	O_w - C	4.0	
	O_w - N	2.0	

TABLE 5. The computational cost of the sub-procedures of the calculation of the intrinsic free energy expressed as a percentage of the total time demand of the analysis of 1 configuration

Step	Approximate Time demand/ %total time /conf
Simulation	28
Cluster analysis	26
ITIM analysis	42
Triangular interpolation	1
Voronoi method	1
Force -position pairing	1
Reslabbing and integration	1

RESUME

Ce travail a pour objectif de montrer la capacité des simulations numériques à modéliser les phénomènes aux interfaces solides et liquides. Dans le travail sur les interfaces solides, la méthode GCMC a été utilisée pour simuler l'isotherme d'adsorption de l'acétaldéhyde sur la glace dans les conditions de la haute troposphère, puis l'adsorption de composés organiques bi-fonctionnalisés sur la glace a été caractérisée par dynamique moléculaire avec pour objectif d'interpréter des résultats expérimentaux de la littérature. Une partie de ce travail a été consacrée à la simulation du diagramme de phase (p,T) d'aérosols organiques (acide oxalique et malonique) dans les conditions troposphériques afin d'étudier la capacité de ces aérosols à jouer le rôle de noyaux de condensation pour les particules de glace. Le travail sur les interfaces liquides a concerné tout d'abord l'adsorption compétitive de polymères et de surfactants à la surface de l'eau. Il s'appuie sur une description très précise, par simulation, de la structure et de la dynamique de la surface des systèmes considérés. La deuxième partie des travaux sur les interfaces liquides s'est intéressée à la caractérisation du transfert d'ions à travers une interface liquide/liquide par le biais du calcul des variations de l'énergie libre du système au cours du transfert. Afin d'obtenir une description très rigoureuse des détails des processus mis en jeu, une méthode spécifique a été développée dans cette thèse pour calculer le profil d'énergie libre en tenant compte directement du caractère très dynamique de l'interface.

SUMMARY

This work aims to demonstrate the ability of numerical simulations to model solid and liquid interfaces. In the work on the solid interfaces, the GCMC method was used to simulate the adsorption isotherm of acetaldehyde on ice under the conditions of the upper troposphere and the molecular dynamics method was used to characterize the adsorption of difunctionalized organic compounds on ice, aiming at interpreting experimental results. Part of this work was devoted to the simulation of the phase diagram (p, T) of organic aerosols (oxalic acid and malonic) in tropospheric conditions to study the ability of aerosols to act as condensation nuclei for ice particles. The work on liquid interfaces concerned firstly the competitive adsorption of polymers and surfactants at the water surface. It is based on a very precise description, by numerical simulation, of the structure and dynamics of the surface of the considered systems. The second part of the work on liquid interfaces has focused on the characterization of ion transfer across a liquid/liquid interface through the calculations of the free energy variations of the system during the transfer. To obtain a rigorous description of the details of the corresponding processes, a specific method was developed in this thesis to calculate the free energy profile while taking into account the dynamics of the interface.